

Development of Improved Entrance Pressure Drop Technique for Extensional Viscosity Determination

Bc. Jan Musil

Master Thesis
2008



Tomas Bata University in Zlín
Faculty of Technology

Univerzita Tomáše Bati ve Zlíně

Fakulta technologická

Ústav výrobního inženýrství

akademický rok: 2007/2008

ZADÁNÍ DIPLOMOVÉ PRÁCE

(PROJEKTU, UMĚLECKÉHO DÍLA, UMĚLECKÉHO VÝKONU)

Jméno a příjmení: **Bc. Jan MUSIL**

Studijní program: **N 3909 Procesní inženýrství**

Studijní obor: **Konstrukce technologických zařízení**

Téma práce: **Vývoj nového postupu pro stanovení tahové viskozity na základě kapilární reometrie**

Zásady pro vypracování:

1. Vypracujte literární studii na dané téma.
2. Teoreticky a experimentálně ohodnoťte vliv designu kapiláry a způsobu kalibrace tlakových čidel na stanovení tahové viskozity pomocí výtlačného reometru pro různé typy lineárních a rozvětvených polymerů.
3. Navrhněte metodiku pro přesnější způsob stanovení tahové viskozity na základě kapilární reometrie a úspěšnost navrženého postupu ověřte pomocí nezávislého měření na Sentmanatově elongačním reometru.

Rozsah práce:

Rozsah příloh:

Forma zpracování diplomové práce: **tištěná/elektronická**

Seznam odborné literatury:

- ZATLOUKAL, M., VLCEK, J., TZOGANAKIS, C., SAHA, P. Improvement in techniques for the determination of extensional rheological data from entrance flows: computational and experimental analysis *Journal of Non-Newtonian Fluid Mechanics*. 2002, no. 107, p. 13.
- BARNES, H. A., HUTTON, J. F., WALTERS, K. *An Introduction to Rheology*. New York : Elsevier, 1989.
- COGSWELL, F. N. *Polymer Melt – A Guide for Industrial Practice*. Cambridge : Woodhead, 1994.
- COLLYER, A. A., CLEGG, D. W. *Rheological Measurement*. London : Elsevier, 1998.
- LARSON, R. G. *Constitutive Equations for Polymer Melts and Solutions*. Boston : Butterworths, 1988.
- MACOSCO, CH. W. *Rheology–Principles, Measurements and Applications*. New York : VCH, 1994.
- MORRISON, F. A. *Understanding Rheology*. New York : Oxford University Press, 2001.
- AGASSANT, J.F., AVENAS, P., SERGENT, J. PH, CARREAU, P. J. *Polymer Processing–Principles and Modeling*. Munich : Hanser, 1991.
- BIRD, R. B., ARMSTRONG, R. C., HASSAGER, O. *Dynamics of Polymeric Liquids, Volume 1 – Fluid Mechanics*. New York : Wiley, 1987.

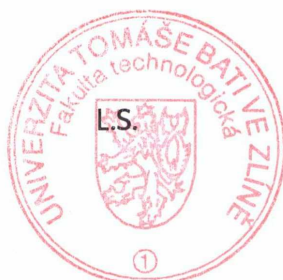
Vedoucí diplomové práce: **prof. Ing. Martin Zatloukal, Ph.D.**
Centrum polymerních materiálů

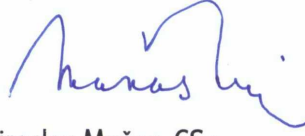
Datum zadání diplomové práce: **19. února 2008**

Termín odevzdání diplomové práce: **23. května 2008**

Ve Zlíně dne 29. ledna 2008


doc. Ing. Petr Hlaváček, CSc.
děkan




doc. Ing. Miroslav Maňas, CSc.
ředitel ústavu

ABSTRAKT

Při zpracování polymerů jsou tyto materiály často vystaveny velmi intenzivnímu elongačnímu toku, což může při dosažení kritických podmínek vyvolat nejrůznější typy tokových nestabilit, jež následně destabilizují celý zpracovatelský proces. Přesné stanovení elongační viskozity polymerů je pak naprosto nezbytné pro navržení optimálního designu zpracovatelských zařízení jako např. vytlačovací hlavy, vyfukovací hlavy, vstřikovací formy atd. Experimentální stanovení této velmi důležité reologické veličiny je však velmi obtížné a nepřesné, zvláště pak v oblasti vysokých deformačních rychlostí a teplot. Prakticky jedinou experimentální metodou pro stanovení elongační viskozity za těchto podmínek je měření vstupní tlakové ztráty při toku tavenin z širokého válce do úzké kapiláry s následnou aplikací metody dle Bindinga, Cogswella nebo Gibsona. Vzhledem k tomu, že design použité kapiláry, způsob kalibrace tlakových čidel a volba příslušné metodiky má zásadní význam na stanovení elongační viskozity, bylo cílem této práce porozumět těmto vlivům a následně navrhnout a ověřit vylepšený způsob stanovení této veličiny. Mezi nejdůležitější přínosy této práce patří navržení a experimentální ověření nového designu kapiláry s nulovou délkou (jež prokazatelně umožňuje přesnější stanovení vstupní tlakové ztráty ve srovnání s běžně používanými kapilárami) a závěr, že nejvhodnější metodikou pro stanovení elongační viskozity u rozvětvených polymerů je Cogswellův model, zatímco pro lineární polymery je to model Bindingův a Gibsonův.

Klíčová slova: Kapilární reometr; Kalibrace tlakových čidel; Kapilára s nulovou délkou; Vstupní viskozita; Bindingův model; Cogswellův model; Gibsonův model; Elongační viskozita; modifikovaný White-Metznerův model; Numerické modelování.

ABSTRACT

In this work, novel orifice die design and pressure transducer down resolution limit calibration procedure to determine precise extensional viscosity data from entrance pressure drop measurements has been developed and tested both, theoretically (through Finite Element Analysis) and experimentally. It has been clearly demonstrated that the proposed improvements leads to much more precise extensional viscosity measurements for polymer melts in comparison with conventional procedures based on the entrance pressure drop measurements. Moreover, it has been found that for extensional strain hardening and extensional strain thinning polymer melts, the corrected Cogswell model and Binding/Gibson model should only be preferred, respectively. Otherwise, the extensional viscosity determination can be rather erroneous.

Keywords: Capillary rheometer; Pressure transducer calibration; Orifice capillary die; Entrance viscosity; Binding model; Cogswell model; Gibson model; Elongational viscosity; modified White-Metzner model; Numerical simulation.

DEDICATION

The first words in my Master Thesis belong to my parents. Via this work, I would like to say: “*Thank you.*”

(Má první slova v mé diplomové práci patří mým rodičům. Prostřednictvím této práce bych Vám rád řekl své: „*Děkuji Vám.*“)

The special dedication is to Professor Martin Zatloukal because he allowed me to look into the mysteries of the beautiful science of rheology.

(Speciální věnování patří profesoru Martinu Zatloukalovi za to, že mi umožnil nahlédnout do tajů krásné vědy reologie.)

ACKNOWLEDGEMENTS

I would like to express my sincere gratitude to all people who supported me during the work on the thesis.

I am especially grateful to my supervisor, Prof. Martin Zatloukal for his patience, guidance and support throughout the process of measuring and analysing data and writing the thesis. It is very difficult to express him the acknowledgement for everything what he did for me during the work on this thesis. Mere “*thank you*” does not seem not be enough...

Many thanks go to Dr. Anežka Lengálová for the time she devoted to proofreading my Master Thesis.

I send my heartfelt gratitude to my uncle, Ing. Jaroslav Císař, who helped me with DSC analysis and IR spectrum of the tested materials.

I am also indebted to CompuPlast® International, Inc. company which has provide finite element based Virtual Extrusion Laboratory™ program for theoretical analysis used in this work.

I should like to acknowledge Steve Bladen and Dipl.-Phys. Torsten Remmler from Malvern company for their fruitful consultations in the field of pressure transducer calibration and temperature sensor principles.

Further, for the aid with creation of software algorithm my thanks fly to Roman Kolařík, my best friend and I would like to extend my gratitude to my family and all friends for their support.

The support of the project by the Czech Grant Agency (Grant no. 103/06/1033) is gratefully acknowledged too.

Finally, I would like to express my thanks to all nonliving things which are helped me to successful creation of this thesis.

Even the small Muse deserves my thanks.

I agree that the results of my Master Thesis can be used by my supervisor's decision. I will be mentioned as a co-author in the case of any publication.

I declare I worked on this Master Thesis by myself, I created all figures and I have mentioned all the used literature.

Zlín, May 20, 2008

Jan Musil

“FELIX QUI POTUIT RERUM COGNOSCERE CAUSAS.”

(Happy is he who has been able to learn the causes of things.)

Publius Virgilius Maro (70 – 19 B.C.),

GEORGICA (*Georgics*).

TABLE OF CONTENTS

INTRODUCTION	12
I THEORETICAL BACKGROUND	14
1 SHEAR AND EXTENSIONAL FLOWS IN POLYMER PROCESSING	15
1.1 BASIC FLOW TYPES	15
1.1.1 Shear flow	17
1.1.1.1 Drag flow	19
1.1.1.2 Pressure driven flow	21
1.1.2 Elongational flow	22
1.1.2.1 Uniaxial elongational flow.....	25
1.1.2.2 Planar elongational flow	26
1.1.2.3 Biaxial elongational flow	27
1.2 REVIEW OF POLYMER PROCESSING TECHNOLOGIES AND THEIR INSTABILITIES.....	28
1.2.1 Melt fracture in extrusion.....	28
1.2.2 Instabilities in film casting process	29
1.2.3 Fibre spinning instabilities	30
1.2.4 Film blowing instabilities.....	31
1.2.5 Coextrusion and interfacial instabilities.....	32
1.2.6 Injection moulding instability	33
2 CAPILLARY RHEOMETRY.....	35
2.1 PRESSURE DROP COMPONENTS	38
2.2 EXTENSIONAL VISCOSITY	39
2.2.1 Entrance viscosity.....	40
2.2.2 Cogswell's analysis	41
2.2.3 Binding's analysis	43
2.2.4 Gibson's analysis.....	45
2.2.5 Haul-off Rheotens	47
2.3 SHEAR VISCOSITY	50
2.3.1 Shear stress.....	50
2.3.2 Shear rate.....	51
2.4 FIRST AND SECOND NORMAL STRESS DIFFERENCES	52
2.5 WALL SLIP.....	57
2.6 CORRECTIONS USED IN CAPILLARY RHEOMETRY.....	59
2.6.1 Bagley correction.....	59
2.6.2 Weissenberg - Rabinowitsch correction.....	61
2.6.3 Effective entry length correction	62
2.6.4 Mooney correction for slip near the wall	63
2.6.5 Hagenbach (kinetic) correction	63
2.6.6 Temperature correction	64
2.6.7 Pressure correction	65
2.6.8 Pressure losses in the rheometer reservoir	66
2.6.9 Adsorption in the channel surface	66

2.7	LIMITATIONS OF CAPILLARY RHEOMETRY	67
2.7.1	Shear stress	67
2.7.2	Shear rate.....	67
3	POLYMER MELT FLOW MODELLING	69
3.1	CONSERVATION EQUATIONS	69
3.1.1	Continuity equation	69
3.1.2	Momentum equation	70
3.1.3	Energy equation.....	72
3.2	CONSTITUTIVE EQUATIONS FOR POLYMER MELTS	72
3.2.1	Modified White-Metzner model	73
3.3	COMPUTER AIDED ANALYSIS AND DESIGN	76
3.3.1	Flow Analysis Network (FAN)	77
3.3.2	Finite Difference Method (FDM).....	78
3.3.3	Finite Element Method (FEM).....	79
4	AIMS OF THE WORK	81
II	EXPERIMENTAL	82
5	MATERIALS.....	83
6	EQUIPMENT AND METHODS	84
6.1	CAPILLARY RHEOMETER ROSAND RH7-2.....	84
6.2	PRESSURE TRANSDUCER CALIBRATION.....	87
6.2.1	Single - point calibration.....	87
6.2.2	Multi - point calibration	88
6.2.3	Pressure calibration device.....	88
6.3	SER-HV-A01 UNIVERSAL TESTING PLATFORM.....	89
6.4	COMPUPLAST® VIRTUAL EXTRUSION LABORATORY™ (VEL)	91
	RESULTS AND DISCUSSION	92
	<i>FEM analysis of Binding, Cogswell and Gibson models</i>	<i>92</i>
	<i>Theoretical effect of die design on the measured extensional rheology.....</i>	<i>96</i>
	<i>Novel orifice die design</i>	<i>98</i>
	<i>Experimental evaluation of the novel orifice die design</i>	<i>98</i>
	<i>Experimental analysis of Binding, Cogswell and Gibson models.....</i>	<i>100</i>
	CONCLUSION	135
	REFERENCES.....	136
	LIST OF SYMBOLS	142
	LIST OF FIGURES	150
	LIST OF TABLES	155
	APPENDICES	156

INTRODUCTION

“INITIA IN POTESTATE NOSTRA SUNT, DE EVENTU FORTUNA IUDICAT.”

(The beginning of the work is in our power, the result is in the hands of fate.)

Lucius Annaeus Seneca the Younger (4 B.C. – A.D. 65),

EPISTULAE MORALES AD LUCILIUM (*Moral Letters to Lucilius*).

Rheology, as a study of the deformation and flow of matter [1], plays an important role not only in polymer processing but also in all other production processes where materials flow (e.g. food processing [2], coating [3], printing [4] etc.). In the case of polymer processing it is possible to answer a lot of questions with knowledge of rheology of the processed polymeric materials. It is well known that rheological properties of polymers are used for example in simulation of processes [5], predicting processing instabilities [6], or distinguishing of various material grades [7].

Flow of polymer melts can be divided into two basic groups: shear and elongational flows. The rheological properties which express the resistance of the material to both types of flow are shear and extensional viscosities, respectively. Ordinarily, during polymer processing, the melts flow into complex flow domains (e.g. flow through converging channels in extrusion/coextrusion dies or injection moulding). For this reason the occurrence of only one flow type is rare and both flows are usually mixed. In order to simplify the flow description of a process, the elongation flow component is usually neglected. Nevertheless, elongation flow causes a lot of instabilities which limit the production rate.

In order to measure extensional viscosity and subsequently to describe elongational flow mathematically, a number of devices [8], [9], [10] and constitution equations [11], [12], [13] were developed. The majority of the extensional viscosity measurement devices are able to determine the extensional viscosity only in low deformation rates. However, in polymer processing the deformation rates can be multiple higher than in laboratory devices.

In the measurement of extensional viscosity at high deformation rates and high temperatures only capillary rheometer can be used. Nonetheless, in these measurements shear and elongational flows are mixed. Furthermore, the influence of orifice capillary die design on the obtained data has not been investigated enough [14]. Thus, elongational

viscosity determination is very complicated and usually not sufficiently precise. Therefore, the main aim of this work is to theoretically as well as experimentally evaluate the effect of orifice capillary die design and pressure transducer calibration process on the extensional viscosity determination from entrance pressure drop for different types of linear and branched polymer melts. Second, a more accurate entrance pressure drop technique for extensional viscosity determination will be proposed. Third, the merits of the novel methodology will be verified through independent extensional viscosity measurements on the Sentmanat extensional rheometer (SER) [10], [15].

I. THEORETICAL BACKGROUND

1 SHEAR AND EXTENSIONAL FLOWS IN POLYMER PROCESSING

“RESISTENTIAM QUÆ ORITUR EX DEFECTU LUBRICITATIS PARTIUM FLUIDI, CÆTERIS PARIBUS, PROPORTIONALEM ESSE VELOCITATI, QUÆ PARTES FLUIDI SEPARATUR AB INVICEM.”

(The resistance arising from the lack of lubricity in the parts of a fluid, is, all other things being equal, proportional to the velocity with which the parts of the fluid are separated from each other.)

Sir Isaac Newton (1643 – 1727),

PHILOSOPHIÆ NATURALIS PRINCIPIA MATHEMATICA (*The Mathematical Principles of Natural Philosophy*).

In this section, the basic types of flow in polymer processing will be provided and a review of flow domains in the process including possible flow instabilities will be presented.

1.1 Basic flow types

The two basic types of flow most often used to characterize polymeric liquids are the shear and elongational flow. In each of them, the material particles have very different relative motion and thus the material responses are quite different.

In order to enable mathematical modelling, the type and intensity of each flow as well as stress response of the investigated material must be known. The former is mathematically defined as a deformation rate tensor whereas the latter is expressed by a stress tensor.

Fig. 1 shows a differential material element that generally moves in Cartesian coordinates with velocities v_x , v_y and v_z in three directions (x , y , z).

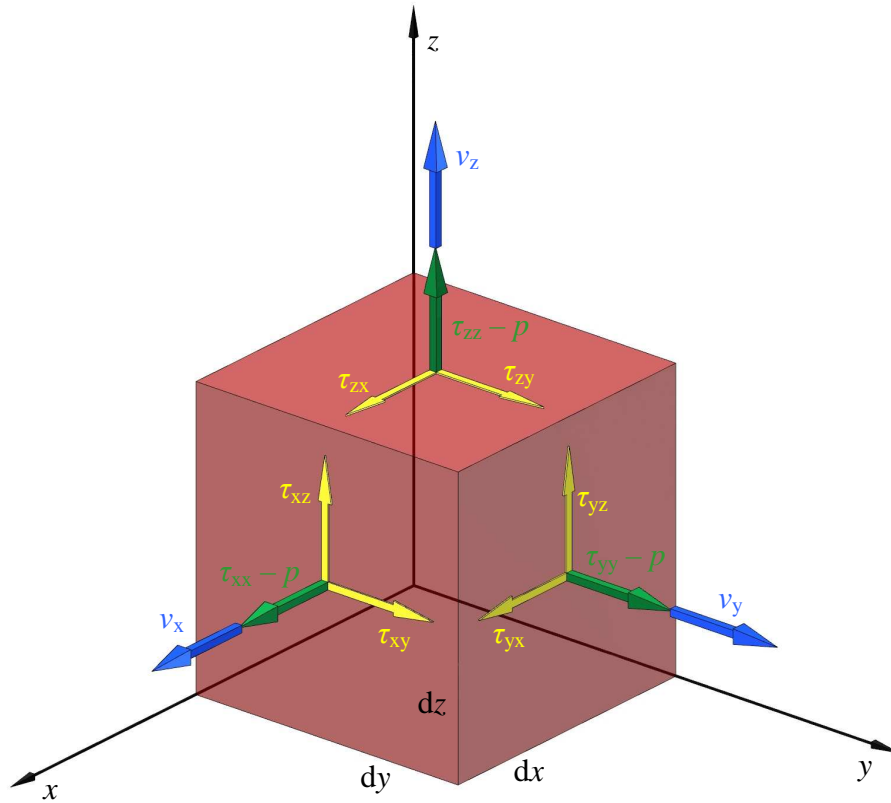


Fig. 1: Movement of a differential material element

With the aid of Fig. 1 the deformation rate tensor can be defined in the following general form (in Cartesian coordinates):

$$\underline{\underline{D}}_{ij} = \begin{pmatrix} 2 \frac{\partial v_x}{\partial x} & \frac{\partial v_y}{\partial x} + \frac{\partial v_x}{\partial y} & \frac{\partial v_z}{\partial x} + \frac{\partial v_x}{\partial z} \\ \frac{\partial v_x}{\partial y} + \frac{\partial v_y}{\partial x} & 2 \frac{\partial v_y}{\partial y} & \frac{\partial v_z}{\partial y} + \frac{\partial v_y}{\partial z} \\ \frac{\partial v_x}{\partial z} + \frac{\partial v_z}{\partial x} & \frac{\partial v_y}{\partial z} + \frac{\partial v_z}{\partial y} & 2 \frac{\partial v_z}{\partial z} \end{pmatrix} \quad (1)$$

where v_x , v_y and v_z are material element velocities in directions x , y , and z . The components in the diagonal of deformation rate tensor represent tensile (elongational) rates, whereas the other components are shear rates.

In shear flow as well as in elongational flow, the deformation rate can be dependent or independent of time. In the case of steady flows the deformation rate is independent of time because the deformation rate has been constant for such a long time that all stresses in the fluid are time-independent. On the contrary, in the transient flows the deformation rate is dependent on time.

The stress tensor is specified in this form (in Cartesian coordinates):

$$\underline{\underline{\tau}}_{ij} = \begin{pmatrix} \tau_{xx} - p & \tau_{xy} & \tau_{xz} \\ \tau_{yx} & \tau_{yy} - p & \tau_{yz} \\ \tau_{zx} & \tau_{zy} & \tau_{zz} - p \end{pmatrix} \quad (2)$$

where p is pressure. In tensor mathematics, ordinarily, the first index specifies the axis of the coordinate system which cuts through the plane in which the stress is acting, and the second index indicates the direction of the stress. The stress tensor components identification is similar as in the previous tensor. The main diagonal components express normal stresses and the others stand for shear stresses. The fluid mechanics of polymer melts is deeply analysed in open literature [16], [17].

In the following sections, the form of both tensors will be shown for shear and elongational flows. Furthermore, incompressibility and isotropy assumptions of polymeric material will be taken into account.

1.1.1 Shear flow

Shear flow is the first basic flow type which occurs in polymer processing. The principle can be understood from *Fig. 2* (the deformation starts at time t_1 and finished at time t_2). Purely shear flow arises when the material element on streamline has a constant rate and it changes the rate only in cross section direction (perpendicular to flow). Mathematically, in steady shear flows, the distance l between two neighbouring fluid particles, which are initially on the y – axis and separated by a distance l_0 , is expressed as [16]:

$$l = l_0 \sqrt{1 + (\dot{\gamma} \Delta t)^2} \approx l_0 \dot{\gamma} \Delta t \quad (3)$$

where $\dot{\gamma}$ is a shear rate and Δt is a time interval in which the deformation is observed. The relative shear deformation (usually called *shear strain*) of the material element (γ) in the time range t_1 to t_2 ($t_2 > t_1$) is expressed by the following equation:

$$\gamma = \dot{\gamma}(t_2 - t_1) \quad (4)$$

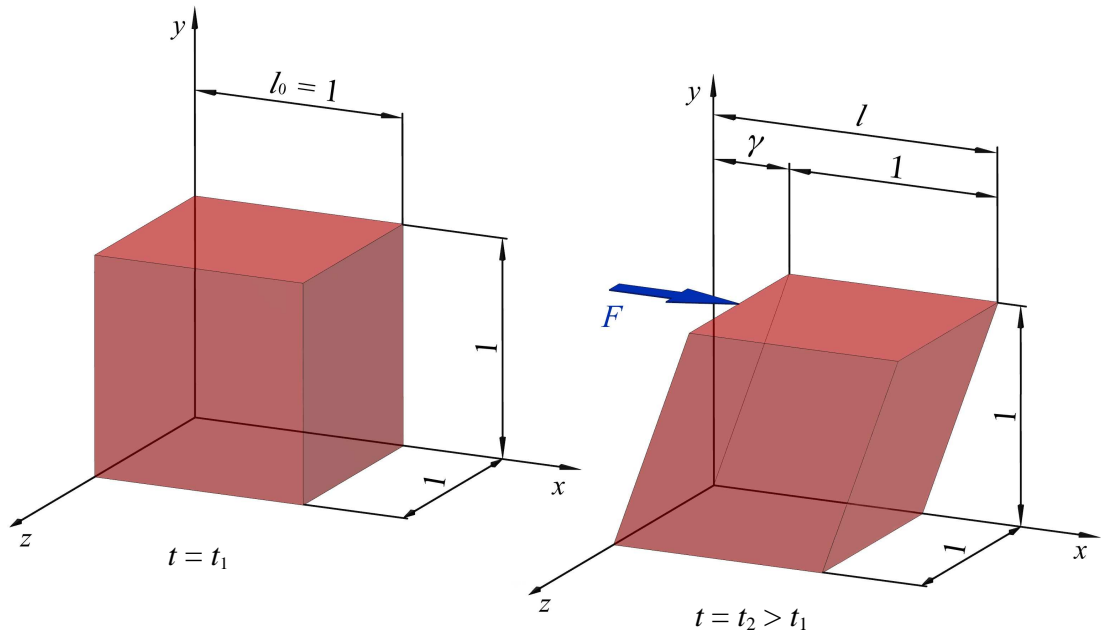


Fig. 2: Shear flow definition sketch

The velocity field in simple shear flow is given as:

$$v_x = \dot{\gamma}y; \quad v_y = 0; \quad v_z = 0 \quad (5)$$

In the case of shear flow, the deformation rate tensor is significantly simplified:

$$\underline{\underline{D}}_{ij} = \begin{pmatrix} 0 & \dot{\gamma} & 0 \\ \dot{\gamma} & 0 & 0 \\ 0 & 0 & 0 \end{pmatrix} \quad (6)$$

and the stress tensor has following form:

$$\underline{\underline{\tau}}_{ij} = \begin{pmatrix} \tau_{xx} - p & \tau_{xy} & 0 \\ \tau_{yx} & \tau_{yy} - p & 0 \\ 0 & 0 & \tau_{zz} - p \end{pmatrix} \quad (7)$$

However, for incompressible fluids we cannot separate the pressure and normal stress contributions in normal force measurements. Therefore, the only experimental quantities of interest are the shear stress and two normal stress differences. It is evident that in the shear flow, commonly used stresses are:

- *Shear stress:* τ_{xy}
- *First normal stress difference (N_1):* $\tau_{xx} - \tau_{yy}$
- *Second normal stress difference (N_2):* $\tau_{yy} - \tau_{zz}$

Furthermore, the material functions (usually called *viscosimetric functions*) are shear viscosity (dependent on shear rate):

$$\eta(\dot{\gamma}) = \frac{\tau_{xy}}{\dot{\gamma}} \quad (8)$$

and normal stress coefficients (dependent on shear rate) which are defined as:

$$\tau_{xx} - \tau_{yy} = \psi_1(\dot{\gamma})\dot{\gamma}^2 \quad (9)$$

$$\tau_{yy} - \tau_{zz} = \psi_2(\dot{\gamma})\dot{\gamma}^2 \quad (10)$$

In addition, for deep understanding of shear flow creation, the drag shear flow and pressure driven flow will be described in more detail. In polymer processing both types exist namely either independently or in combination. For example, the function of screw extruder is based on the combination of drag flow and pressure driven flow [18].

1.1.1.1 Drag flow

In order to explain the drag shear flow principle, two infinitely wide (W) parallel plates (stationary and moving), separated by a gap (H) will be considered (thus, shear flow is only in one direction). As can be seen in *Fig. 3*, the fluid is between the bottom (stationary) and top (moving) plates and to cause flow, the top plate must move (velocity v_M). From the above it is evident that the motion in this flow is not based on the pressure gradient.

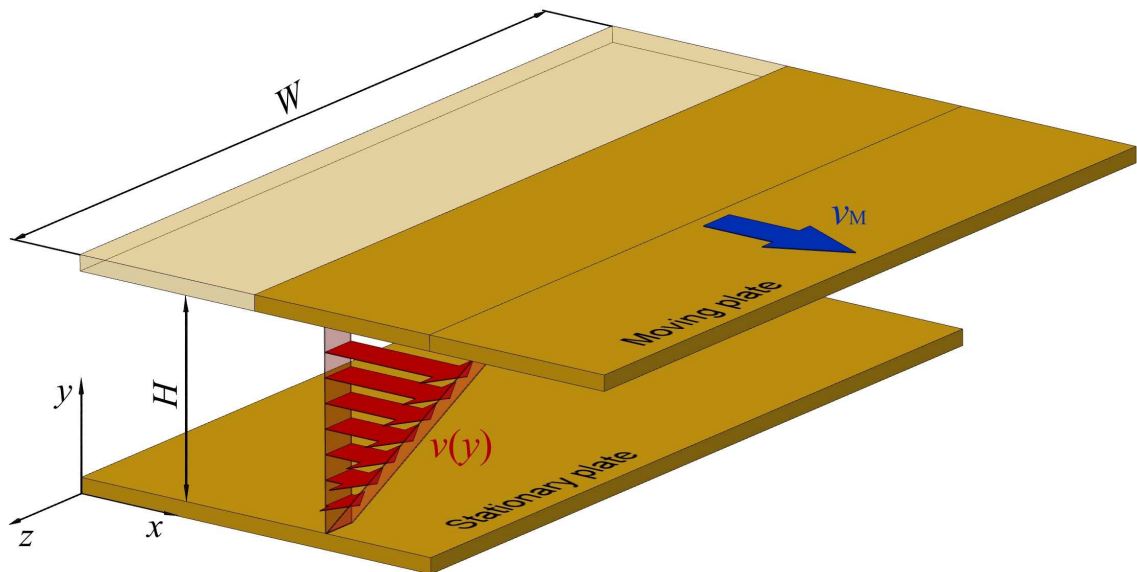


Fig. 3: Principle of drag shear flow and its velocity profile

Fig. 4 shows the detail of several abutting material layers deformation (before and after deformation). It is clear that the layers are deformed according to the velocity profile and no layer is stretched.

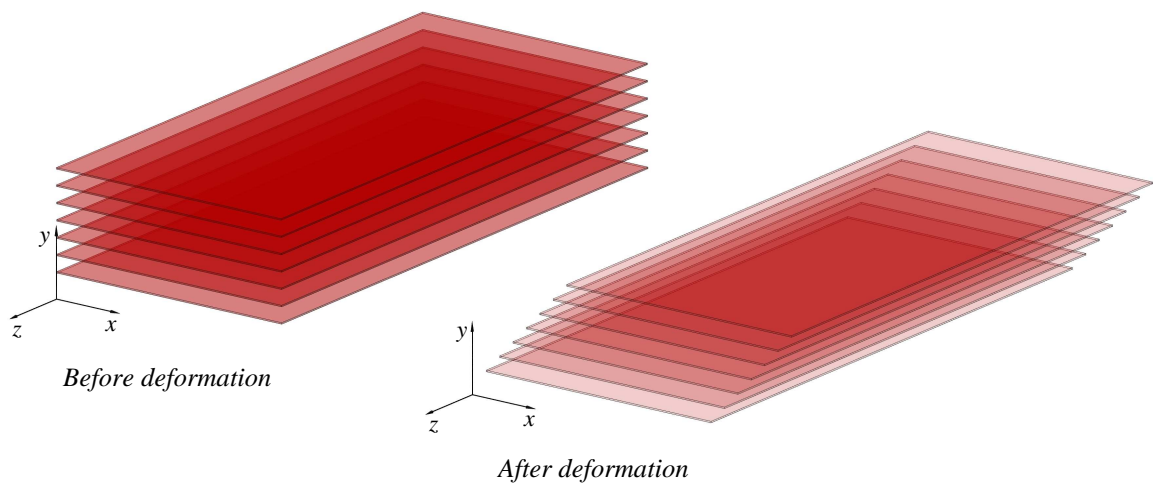


Fig. 4: Deformation of abutting material layers in drag shear flow

1.1.1.2 Pressure driven flow

The principle of pressure driven flow (frequently called *Poiseuille flow*) is based on pressure differences of flow domain sections in the flow direction. Fluid always runs from the high-pressure section to the lower-pressure section. The *Poiseuille flow* of fluid occurs in a thin slit [19] as well as in circular tube [20].

For deeper clarification, as indicated in *Fig. 5*, two infinitely wide (W) stationary parallel plates, separated by a gap (H), will be considered. The pressure difference between the entrance and exit sections is Δp , and is caused by the flow of the fluid. From the figure it is also evident that the velocity profile in *Poiseuille flow*, $v(y)$, is significantly different from the velocity profile in drag flow. The velocity has parabolic profile (in the case of Newtonian fluids), in which the zero velocity is on the wall and the velocity maximum is in the middle of geometry. Therefore, at the walls the shear rate is maximal and in the middle of domain the shear rate is minimal.

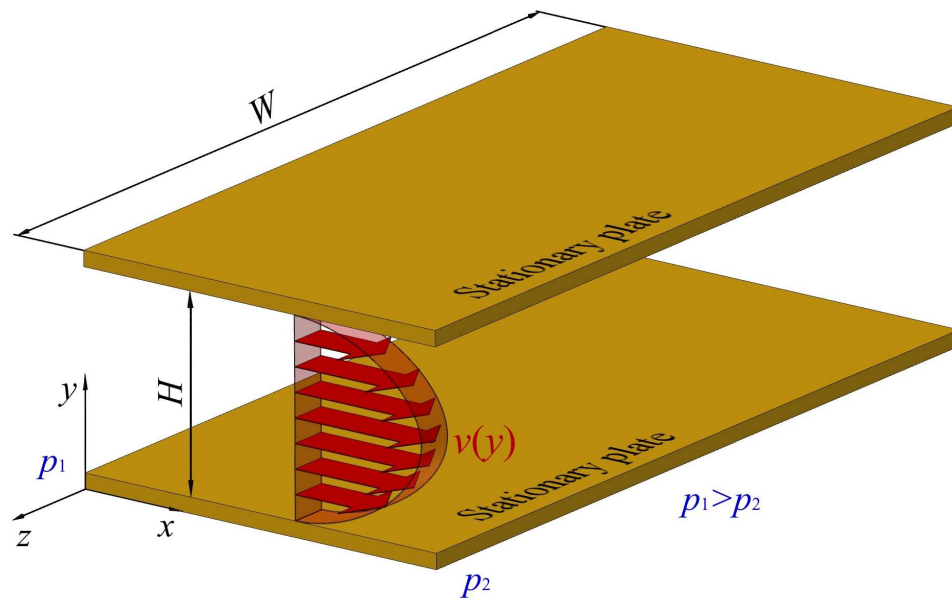


Fig. 5: Poiseuille flow into a thin slit and its velocity profile

For further illustration the neighbouring material layers deformation is shown in *Fig. 6*. In the same way as in the previous flow, the layers deformation follows the velocity profile and no layer is stretched.

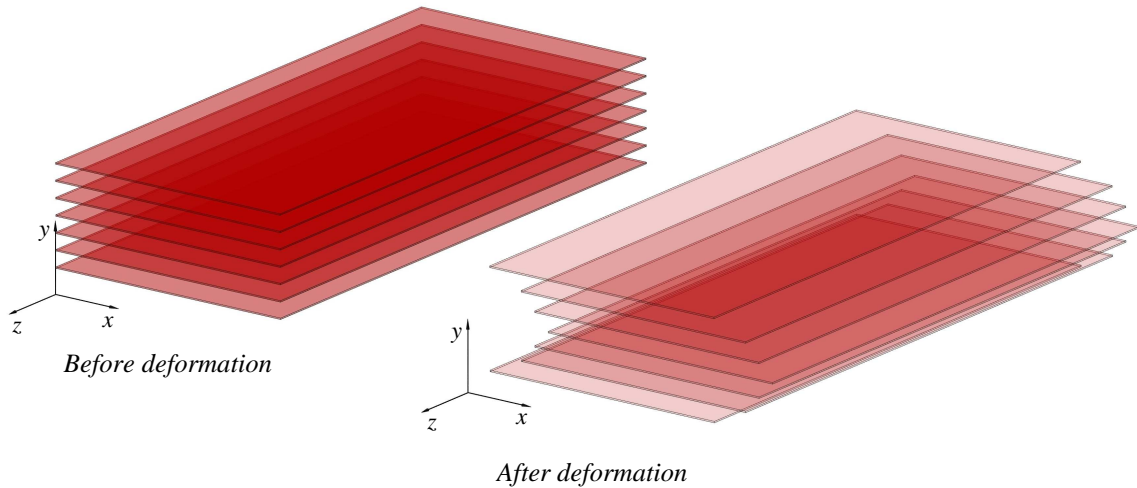


Fig. 6: Deformation of neighbouring material layers in Poiseuille flow

1.1.2 Elongational flow

At elongational flow (also called *shearfree flow*) the material element is stretched in one or two directions. Purely elongational flow arises when a material element changes the rate on streamline and at the same time the elements on all neighbouring streamlines have an identical rate (see Figs. 7, 8, 9). In these figures, start of deformation (dark solid) is in time t_1 , and the deformation finishes (transparent solid) at time t_2 .

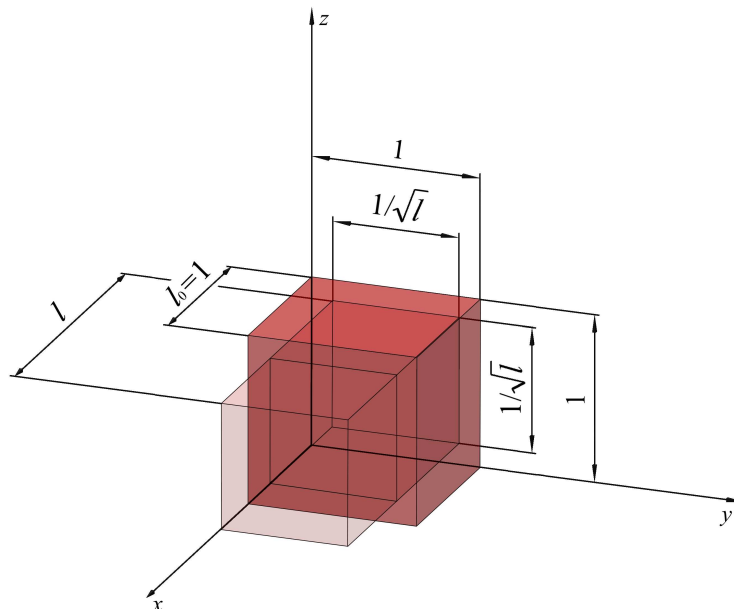


Fig. 7: Definition sketch of uniaxial elongational flow

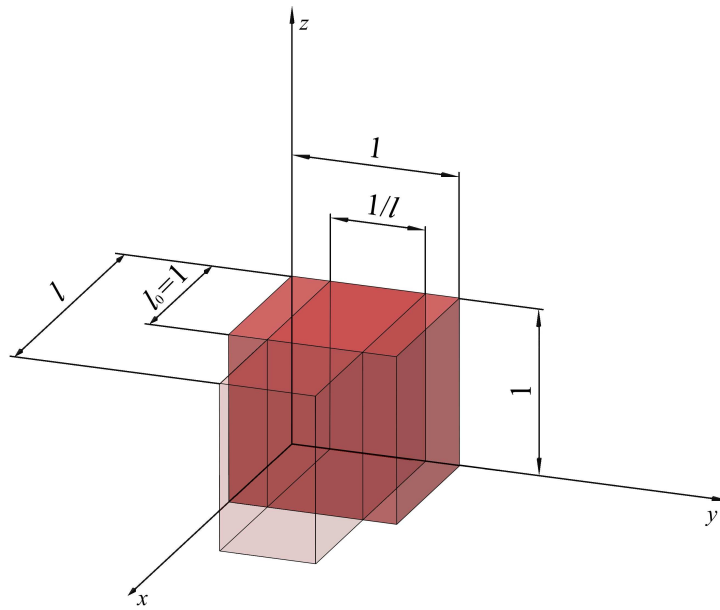


Fig. 8: Definition sketch of planar elongational flow

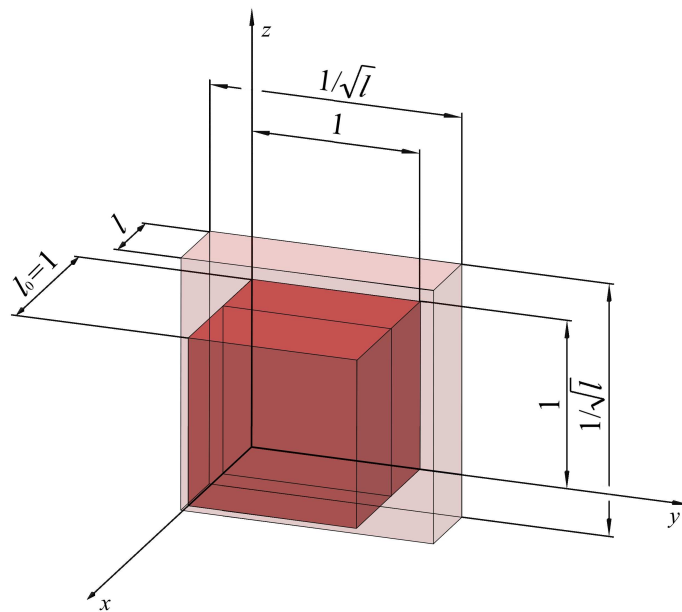


Fig. 9: Definition sketch of biaxial elongational flow

A characteristic attribute of steady elongational flows is expressed by an exponential rate of relative motion of a fluid element to a neighbouring one. This is also shown in *Figs. 7, 8, 9*, when two neighbouring fluid particles are separated by an initial distance l_0 . After time Δt the distance l_0 changes into l according to relation [16]:

$$l = l_0 e^{\dot{\epsilon} \Delta t} \quad (11)$$

In the same way as for shear flow, the relative elongational deformation (frequently called *elongational strain*) of a material element (ε) between times t_1 and t_2 (when $t_2 > t_1$) can be determined as:

$$\varepsilon = \dot{\varepsilon}(t_2 - t_1) \quad (12)$$

The velocity field in simple elongational flows is defined for each direction as:

$$v_x = \frac{1}{2}\dot{\varepsilon}(1+b)x; \quad v_y = \frac{1}{2}\dot{\varepsilon}(1-b)y; \quad v_z = -\dot{\varepsilon}z \quad (13)$$

where $0 \leq b \leq 1$ and $\dot{\varepsilon}$ represents elongational rate. Several special elongational flows can be observed for particular choices of parameter b :

- Uniaxial elongational flow: $b = 0, \dot{\varepsilon} > 0$
- Planar elongational flow: $b = 1$
- Biaxial elongational flow: $b = 0, \dot{\varepsilon} < 0$

In the case of incompressible fluids, only two normal stress differences are of experimental interest:

- *First normal stress difference* (N_1): $\tau_{xx} - \tau_{yy}$
- *Second normal stress difference* (N_2): $\tau_{yy} - \tau_{zz}$

Nevertheless, in uniaxial and biaxial elongational flows, for which parameter b is equal 0 in Eq. (13), the x and y directions are indistinguishable, so $\tau_{yy} - \tau_{zz} = 0$ and there is only one normal stress difference to be determined for these flows.

The material functions in steady simple elongational flows are two viscosity functions (dependent on elongational rates) which describe two normal stress differences:

$$\tau_{zz} - \tau_{yy} = \eta_{E1}(\dot{\varepsilon}, b)\dot{\varepsilon} \quad (14)$$

$$\tau_{yy} - \tau_{zz} = \eta_{E2}(\dot{\varepsilon}, b)\dot{\varepsilon} \quad (15)$$

In the special steady state elongational flow where parameter b is equal 0, $\eta_{E2} = 0$ and η_{E1} is equal to the elongational viscosity (sometimes called the *extensional viscosity*) η_E :

$$\eta_E(\dot{\varepsilon}, 0) = \frac{\tau_{xx} - \tau_{yy}}{\dot{\varepsilon}} \quad (16)$$

For $\dot{\epsilon} > 0$, η describes uniaxial elongational flow and for $\dot{\epsilon} < 0$ it describes biaxial elongational flow.

The following part is devoted to description of three basic types of elongational flow. As will be discussed in *Chapter 1.2*, the elongational flow in polymer processing often accompanies shear flow and causes a number of flow instabilities.

1.1.2.1 Uniaxial elongational flow

A schematic view of uniaxial elongational flow is presented in *Fig. 10*. As can be seen, a material element is stretched in one direction (x) and in other directions (y, z) it is compressed (in the case of isotropic material). In the figure blue colour represents the action and green colour expresses the material response.

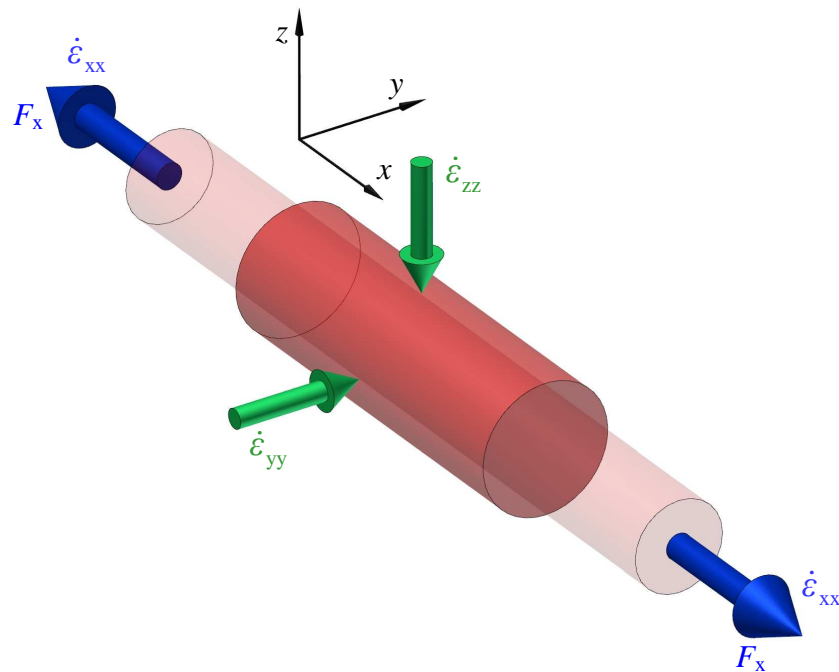


Fig. 10: Uniaxial elongational flow

In order to describe uniaxial elongational flow mathematically, the deformation rate tensor is established as:

$$\underline{\underline{D}}_{ij} = \begin{pmatrix} \dot{\epsilon} & 0 & 0 \\ 0 & -0.5\dot{\epsilon} & 0 \\ 0 & 0 & -0.5\dot{\epsilon} \end{pmatrix} \quad (17)$$

The tensor represents the nature of the process, thus the plus sign (i.e. no sign) before $\dot{\epsilon}$ component means the given action and the minus sign before $0.5 \dot{\epsilon}$ represents the material reaction.

The stress tensor then has following form:

$$\underline{\underline{\tau}}_{ij} = \begin{pmatrix} \tau_{xx} - p & 0 & 0 \\ 0 & \tau_{yy} - p & 0 \\ 0 & 0 & \tau_{zz} - p \end{pmatrix} \quad (18)$$

1.1.2.2 Planar elongational flow

As shown in *Fig. 11*, the material element in planar elongational flow is stretched in one direction (x), in the second direction (y) it is clamped and in the third direction (z) it is compressed.

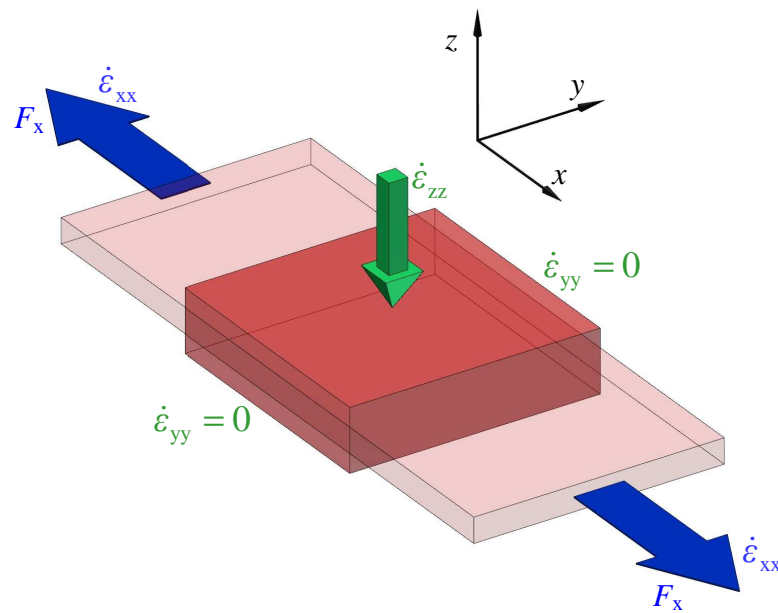


Fig. 11: Planar elongational flow

The deformation tensor in this case is written in the following form:

$$\underline{\underline{D}}_{ij} = \begin{pmatrix} \dot{\epsilon} & 0 & 0 \\ 0 & 0 & 0 \\ 0 & 0 & -\dot{\epsilon} \end{pmatrix} \quad (19)$$

In the tensor it is clearly seen that the rate of stretching in x and y directions is equal and the zeros in diagonal express clamping of material. The stress tensor in planar flow is in the same form as in the uniaxial elongational flow, Eq. (18).

1.1.2.3 Biaxial elongational flow

Fig. 12 shows biaxial elongational flow in which the material element is stretched in two directions (x, y), and in third direction (z) it is compressed. The elongational rates in directions x and y can be equal (this is the unique case when we can determine the elongational viscosity) or different (it is not possible to determine the one elongational viscosity but two of them are needed for particular directions).

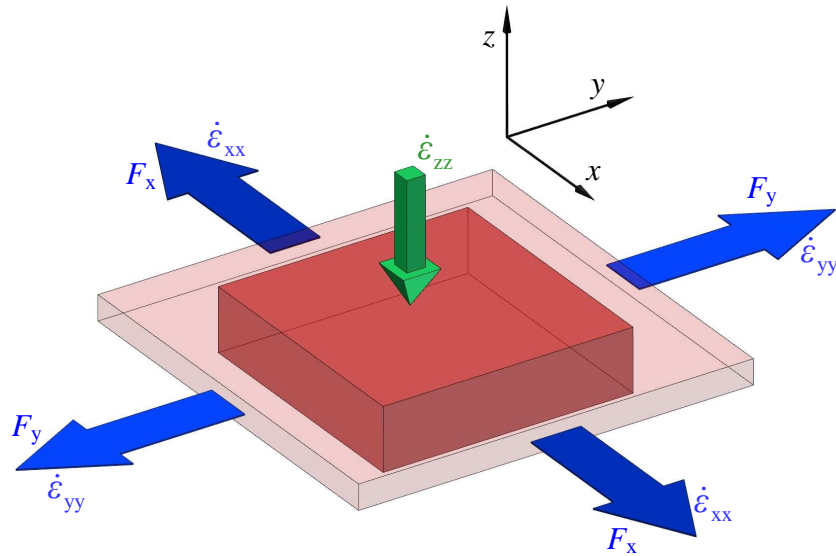


Fig. 12: Biaxial elongational flow

The deformation rate tensor in biaxial elongational flow with the same elongational rates in both directions is given by:

$$\underline{\underline{D}}_{ij} = \begin{pmatrix} \dot{\epsilon} & 0 & 0 \\ 0 & \dot{\epsilon} & 0 \\ 0 & 0 & -2\dot{\epsilon} \end{pmatrix} \quad (20)$$

The same elongational rates are in the two positions in the main diagonal ($\dot{\epsilon}$) and the third position ($-2\dot{\epsilon}$) represents twice the speed of material compression. The stress tensor has the same form as in the uniaxial elongational flow, Eq. (18).

It should be kept in mind that in preponderance of polymer processes shear and elongational flow components are mixed, which causes many processing problems (for example instabilities, which are described below). Nevertheless, the complex industrial flows are often simplified in such a way that the minor flow component is neglected and the flow situation is viewed as simple shear flow or simple elongational flow. Due to the simplifications, the flow description is not exact and theoretical predictions are imprecise. It should be also noted that in many cases the reasons of these simplifications are connected with the extensional viscosity measurement difficulties.

1.2 Review of polymer processing technologies and their instabilities

Flow instabilities are fundamental problems of fluid dynamics. The focus of hydrodynamical stability is in the transition from laminar to turbulent flow. The flow of polymer fluids is significantly different from the low-viscosity counterparts, therefore the base of flow instabilities for both is completely distinct. In the case of low-viscosity fluids the turbulent flow is caused by inertial forces (usually expressed as the *Reynolds number*). On the other hand, disturbances in laminar flow of high-viscosity polymers are produced as a consequence of fluid elasticity (usually expressed as the *Weissenberg number*).

In the case of polymer processing, the origin of instabilities is caused by many effects, where the most significant is the extensional viscosity (extensional flow). With the aim to see where flow instabilities play an important role in polymer processing, a short overview in this sense is provided bellow.

1.2.1 Melt fracture in extrusion

A typical extrusion line is depicted in *Appendix A I*. Polymeric material is fed to the hopper of the extruder, and transported and simultaneously melted. Subsequently it is formed in the extrusion die to required shape, and the further final product is calibrated, cooled, drawn-off, cut and placed on a palette (pipes and profiles) or cooled, cut and wound on a reel (films). This technology is typical of pipes, profiles and films production.

Polymer extrusion is one of the simplest polymer processing operations, but as a consequence of shear and extensional flows existence in extrusion dies, it exhibit a full range of flow instabilities. The most common problems in polymer extrusion consist in

melt fracture, *wall slip* and *polymer elasticity*. As a result of these phenomena, the production rate of extrusion line must not exceed a certain limit.

The typical development of melt fracture instability is shown in *Fig. 13*. As can be seen, the first extrudate (*a*) has a *smooth surface* because the shear rate was small. In case (*b*), the shear rate was higher and *surface melt fracture* (also called *sharkskin*) arose. At the highest values of the output rate, *gross melt fracture* occurs (*c*) – the extrudate is distorted.

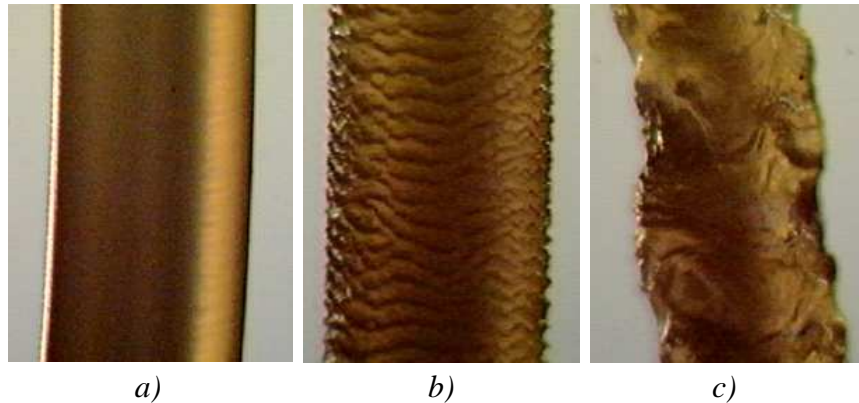


Fig. 13: Development of melt fracture instability with increasing shear rate: (a) smooth surface, (b) sharkskin, (c) gross melt fracture (taken from [21])

1.2.2 Instabilities in film casting process

The extrusion product line for film casting is shown in *Appendix A II*. The polymer melt is transported from the extruder to the film (slit) die, where polymer melt is conveyed to thin film. The film is cooled on dual chilled rolls, then the thickness is measured, edges are cut and the final film is wound up.

The main aim of this process is the increase of production speed and reduction of film thickness. On the contrary, problems as *edge neck-in*, *bead formation* and some other *instabilities* create troubles in the die exit region as indicated in *Fig. 14* (adapted from [6]). As a result of high melt viscosity, the downstream pulling is usually used. However, this configuration causes *neck-in* at edges which leads to creation of non-uniform gauge profile. Furthermore, instabilities accompanied with film casting process of polymers cause spontaneous thickness and width oscillations. Next, the *draw resonance* arises when the wound up rate is too high. In addition, the properties of final film is non-uniform due to the non-uniform elongation of each particle of material which is caused by various speed of

each one. Finally, problems with adjustment of die lip thickness can also caused the non-uniform thickness of final film product.

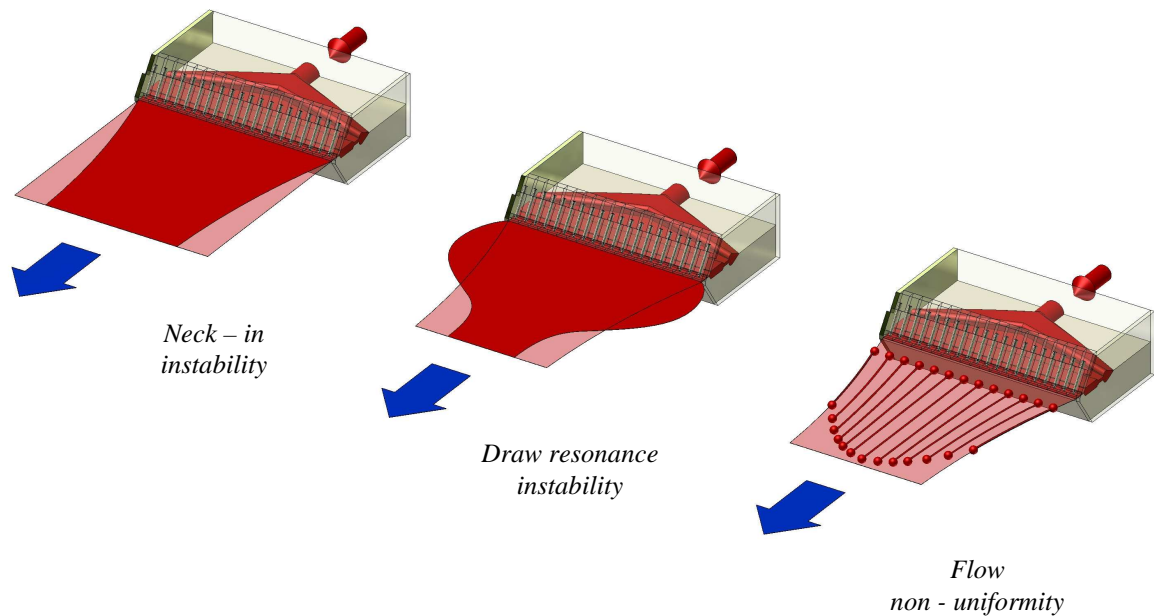


Fig. 14: Instabilities in film casting process

1.2.3 Fibre spinning instabilities

Another polymer process where instabilities play an important role is fibre spinning. The process is depicted in *Appendix A III*. Polymer melt is prepared in the extruder and then it is pumped through a plate with many small holes – *spinneret*. The melt is cooled in water bath, slowly pulled by rolls, and warmed to orientation temperature in tempering bath. The following process is drawing of fibres, then the fibres are cooled in stabilization bath, pulled by fast rolls and finally they are wound up to coils.

Fig. 15 shows one hole of *spinneret* with flow of the material. With the aid of ambient air the extruded filaments are cooled, and subsequently they are stretched by a rotating wind-up roll, which is placed before the solidification line.

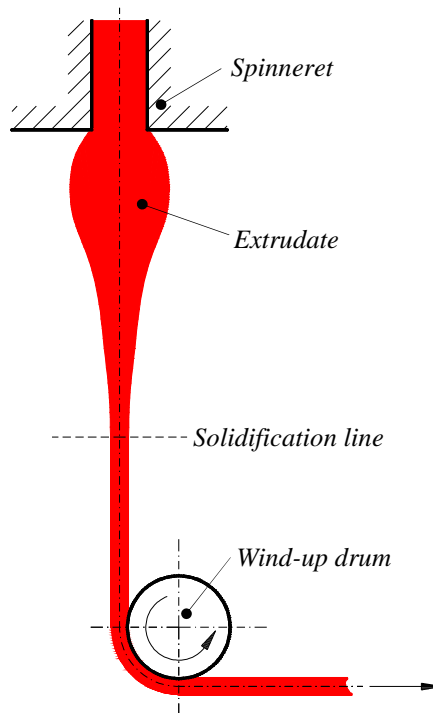


Fig. 15: One spun fibre

In this polymer process, as well as in all other processes in this section, high production speed requirements are limited by the onset of instabilities. In fibre spinning, three basic types of instability can arise and they are connected with *spinneret*. First, instability called *drawability*, which is a capability of polymer melts to stretch without breaking. Second, instability called *draw resonance*, which is defined as a periodic fluctuation of the cross-sectional area of wound-up fibres. Third, instability well known as *melt fracture*, which is described in *Chapter 1.2.1*.

1.2.4 Film blowing instabilities

Film blowing process is used for production of carrier bags, polymer films or sacks. A simple film blowing production line is shown in *Appendix A IV*. The polymer melt flows from the extruder to an annular blowing die, which distributes the melt from a circular channel (end of extruder) to annular area. Therefore, the melt is extruded in the tube form (at the freeze line the melt undergoes transition from liquid to solid state), subsequently it is cooled by a cooling ring, enfolded by two table flats and stretched by nip roles. After it, the film is measured, guided to a storage device by guide rolls, its edges are cut and the film is pulled by wind up device (in the case of single film as a product) or only pulled by wind up device (in the case of twin film as a product).

Fig. 16 (adapted from [22]) shows several types of instabilities in film blowing process which can be observed. These instabilities have a negative influence on mechanical and optical properties of the final product. At *draw resonance* the film tube periodical changes diameter and this common start-up problem occurs when molten film stretches so quickly that it gets stiff. In the case of *freeze line instability* the freeze line height periodical oscillation and it is caused by surging, drafts, or relatively slow shifts in ambient temperature. *Bubble sag instability* means that the bubble sack touches the cooling ring and this instability is observed when the wind-up speed is small. *Bubble tear* is appeared when the stress in blown polymeric material reaches the rupture stress (the wind-up speed is too high). At *bubble flutter* the surface of bubble between die exit and freeze line flutter quivers and the reason of it is in the high speed of cooled air.

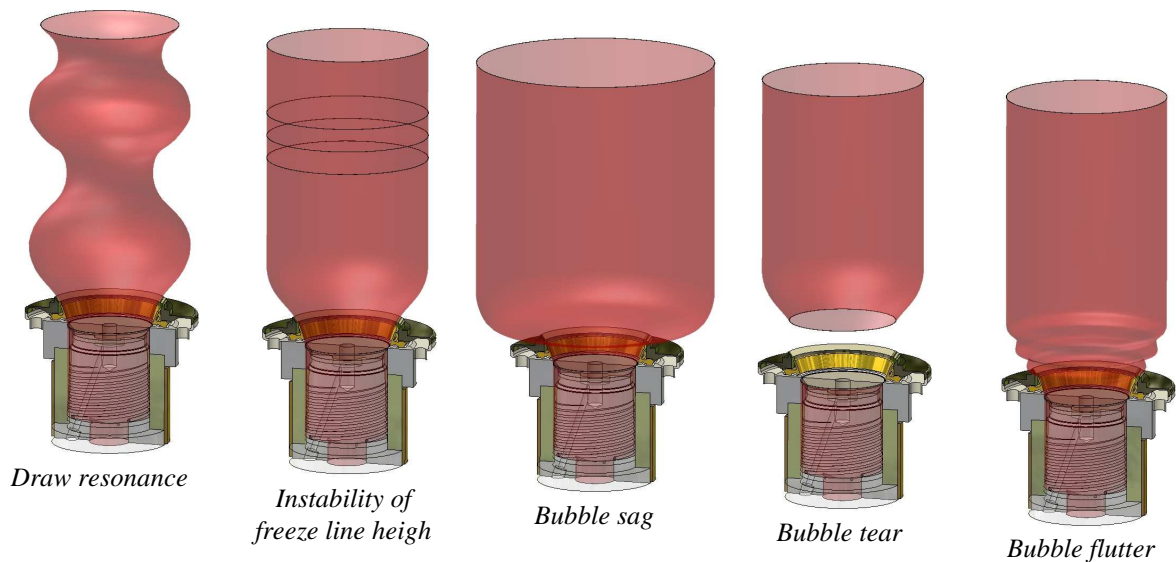


Fig. 16: Film blowing instabilities

1.2.5 Coextrusion and interfacial instabilities

Coextrusion is a technology in which two or more polymer melts are simultaneously extruded. Each of the polymer melts is prepared in one extruder (the number of extruders is the same as the number of layers) and in the feedblock (in the case of extrusion), or in the film blowing die (in the case of film blowing) the polymer melts create required coextrusion structure. The coextrusion of polymer melts is applied in barrier films, cables, fibres, pipes, profiles and in many more.

Three basic types of instabilities which can arise in coextrusion are depicted in *Fig. 17* (adapted from [6]). The non-uniformity of layers (*encapsulation*) and interfacial instabilities (*zig-zag* and *wave*) are caused by differences in viscous and elastic properties of the components as well as by the geometry of the coextrusion die. Low adhesion between coextrusion materials causes another instability – *material incompatibility*. Another instability which is connected with extrusion as well as coextrusion is *melt fracture*, as already discussed.

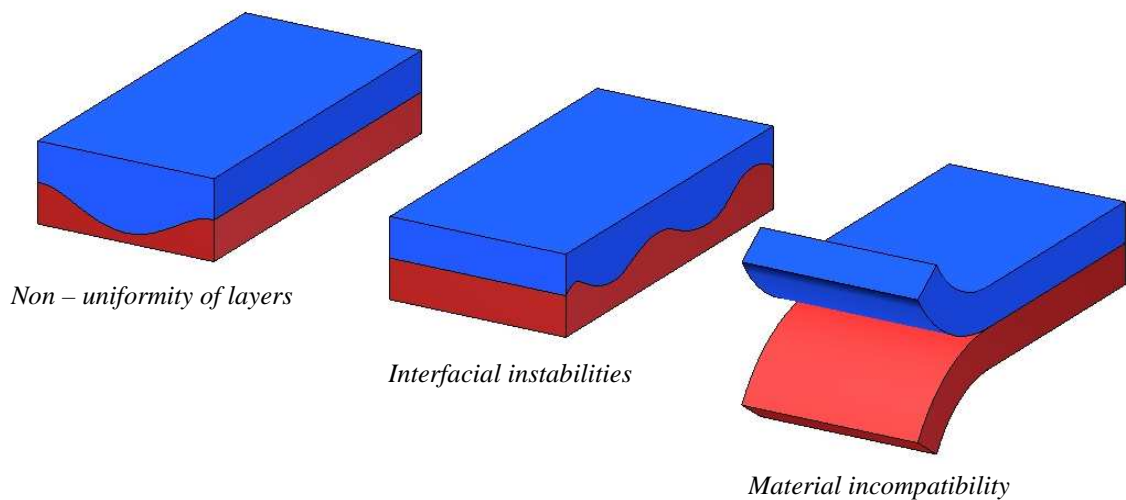


Fig. 17: Coextrusion instabilities

1.2.6 Injection moulding instability

Injection moulding process is shown in *Appendix A V*. In this technology, the polymer material is transferred from solid state to molten state in an extruder and afterwards the polymer melt is pumped with high pressure through the runners into a cavity of mould (the cavity has a negative shape of the product). The injection machine has two parts. First, the injection part contains the extruder and the fixed part of a mould. Second, the clamping unit includes a clamping mechanism and the moving part of a mould.

An ideal product of injection moulding is free of depressions and warpage, has smooth surface and sufficient mechanical strength and stiffness for its end use. The foregoing is significantly influenced by residual stresses due to the viscoelastic nature of flow and shrinkage during cooling of the mould.

As can be seen in *Fig. 18* (adapted from [17]), polymer melt in injection demonstrates “*fountain flow*” into runners and the elements on the forehead of polymer melt are stretched (the rectangles in this figure show the deformation of a nearly squared element). This phenomenon causes tear of the melt, which creates optical defects on the final product.

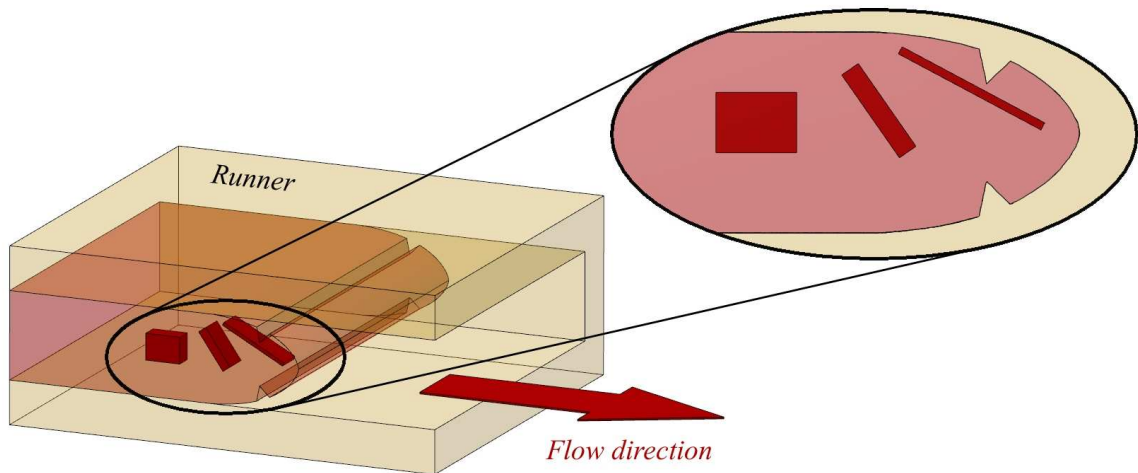


Fig. 18: Cross section view of runner with detail of deformation element and tear forehead of melt

From above initiate overview of polymer processing technologies and its instabilities is evident that is necessary to investigated these problems in order to increase the production rate of all these technologies. Furthermore, majority of these instabilities is caused by elongational flow in these processes. Therefore, improvement in measurement of elongational viscosity as well as in mathematical modelling of each process is essential.

2 CAPILLARY RHEOMETRY

“CYLINDRI, QUI SECUNDUM LONGITUDINEM SUAM UNIFORMITER PROGREDITUR, RESISTENTIA EX AUCTIONE VEL DIMINUTIONE EJUS LONGITUDINE NON MUTATUR; IDEOQUE EADEM EST CUM RESISTENTIA CIRCULI EADEM DIAMETRO DESCRIPTI ET EADEM VELOCITATE SECUNDUM LINEAM RECTAM PLANO IPSIUS PERPENDICULAREM PROGREDIENTIS.”

(If a cylinder move uniformly forwards in the direction of its length, the resistance made thereto is not at all changed by augmenting or diminishing that length; and is therefore the same with the resistance of a circle, described with the same diameter, and moving forwards with the same velocity in the direction of a right line perpendicular to its plane.)

Sir Isaac Newton (1643 – 1727),

PHILOSOPHIÆ NATURALIS PRINCIPIA MATHEMATICA (*The Mathematical Principles of Natural Philosophy*).

Capillary rheometry is the oldest and most widely used method of qualitative estimation and viscosity measurement. The first viscosity tests with small capillaries were carried out by Hagen [23] (in Germany) and independently Poiseuille [24] (in France) in the 19th century in order to determine the viscosity of water. Since then the capillary rheometry has gone through many improvements. In 1929 Rabinowitsch [25] developed non-Newtonian behaviour correction, which is applied on shear rate. Two years later, Mooney [26] discovered a procedure for calculation of wall slip velocity. In the 1950s, Bagley [27] presented a well - known correction to eliminate the end phenomena in a capillary. Furthermore, for determination of first and second normal stress differences at the end of sixties Broadbent *et al.* [28] found out pressure holes methodology (will be discussed in *Chapter 2.4*). The first work describing the elongational flow in capillary rheometer was published in 1972 by Cogswell [29]. With the aid of first and second normal stress differences measurement Han [30] in 1974 replaced the circular capillary die by a slit die with more than one pressure transducer. Binding [31] and independently Gibson [32] published two different additional entrance pressure drop techniques for elongational viscosity determination in the late 1990s. Recent work published by Kim and Dealy [14] was focused on improvement of the design of orifice capillary die.

From the above it is clear that capillary rheometer is a universal viscometer which can be used to determine shear viscosity, elongational viscosity, first/second normal stress difference and wall slip. On the following pages all these methods are described in detail.

Capillary rheometer can be produced in several modes, which are distinguished by the: *number of barrels* (single or twin bore), *manner of pressure generation* (compressed gas, gravity or piston), *measured quantity* (controlled-pressure and controlled-rate). Another type is an on-line capillary rheometer that is mounted on an extruder.

In our research we are going to use a twin-bore capillary rheometer (controlled-rate mode), which is outlined in *Fig. 19*. From this figure it is evident that the principle of capillary rheometer is similar as the principle of a real extruding machine. Before the start of a test, the measured material in the form of granules is filled to both reservoirs and perfectly compacted. Then it is melted through the reservoir walls, which are warmed from the heated barrel. Subsequently, the pistons press the molten material through two calibrated capillary dies. In order to measure the pressure drop, two highly precise pressure transducers in the entrance region of capillary dies are located. It should be noted that all the quantities measured on controlled-rate capillary rheometer are determined only through the knowledge of dies geometry, load shear rate and measured pressure drop.

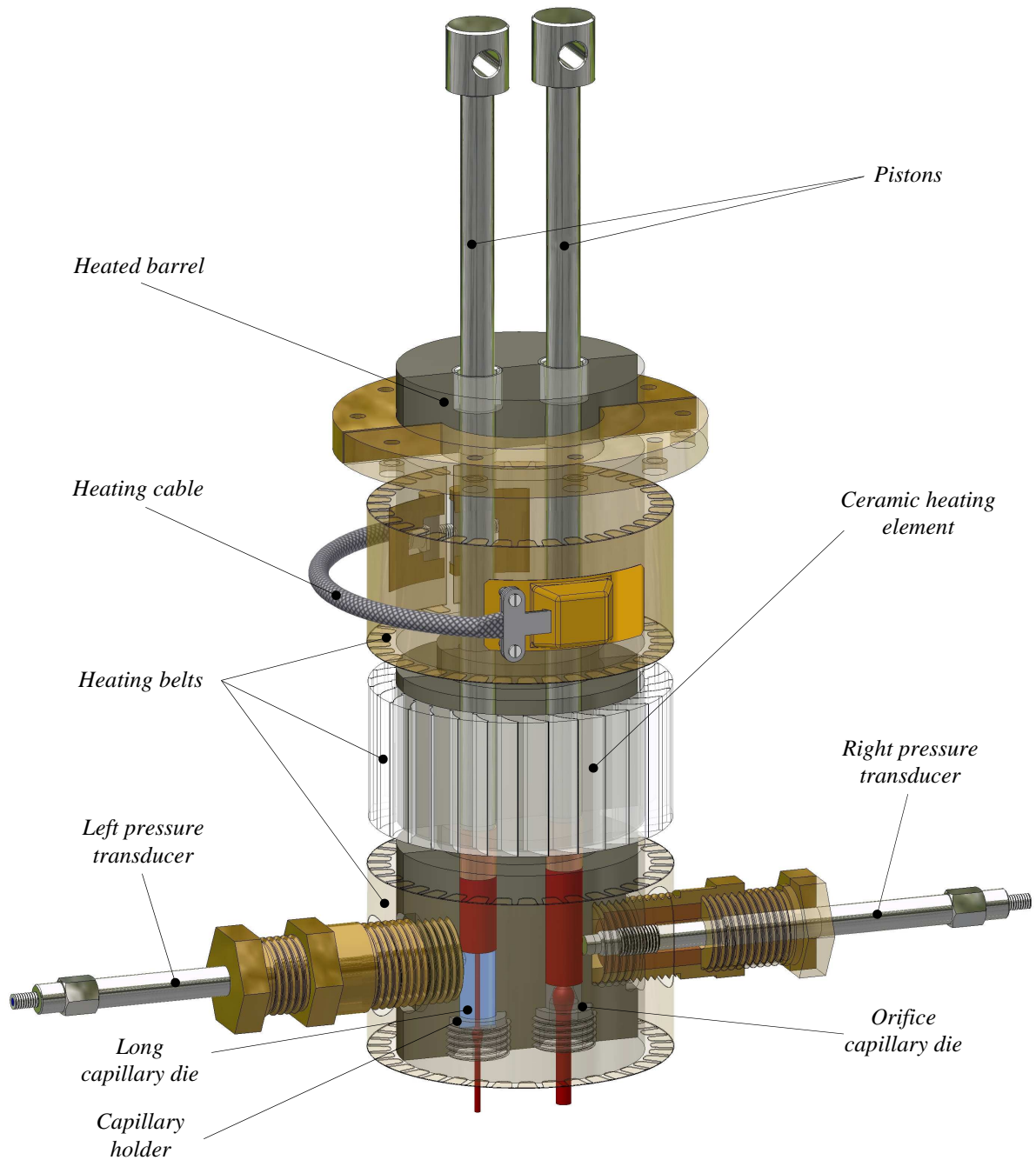


Fig. 19: Transparent section view of barrel part of twin-bore capillary rheometer (controlled-rate mode)

2.1 Pressure drop components

From the theory of capillary rheometry [20] it is well known that to press the measured material through a capillary die it is necessary to apply energy that is measured as a total pressure drop. However, this total pressure drop consists of three partial pressure components:

- *Entrance pressure drop* (Δp_{ENT}): This pressure is necessary to relocate the fluid from a wide barrel to a narrow capillary die; it is a consequence of elongational viscosity of fluid.
- *Capillary pressure drop* (Δp_{CAP}): This difference expresses energy that must be supplied into a polymer melt in order to flow the fluid through the capillary die; it depends on shear viscosity of the polymer melt.
- *Exit pressure drop* (Δp_{EXIT}): This pressure represents the resistance of fluid to the outflow from capillary die; it is the result of non-zero first normal stress difference of the measured fluid.

The sum of the entrance and exit pressure is called end pressure drop (Δp_{END}). *Fig. 20* (adapted from [17]) depicts all pressure drops, including the location of origin of these drops.

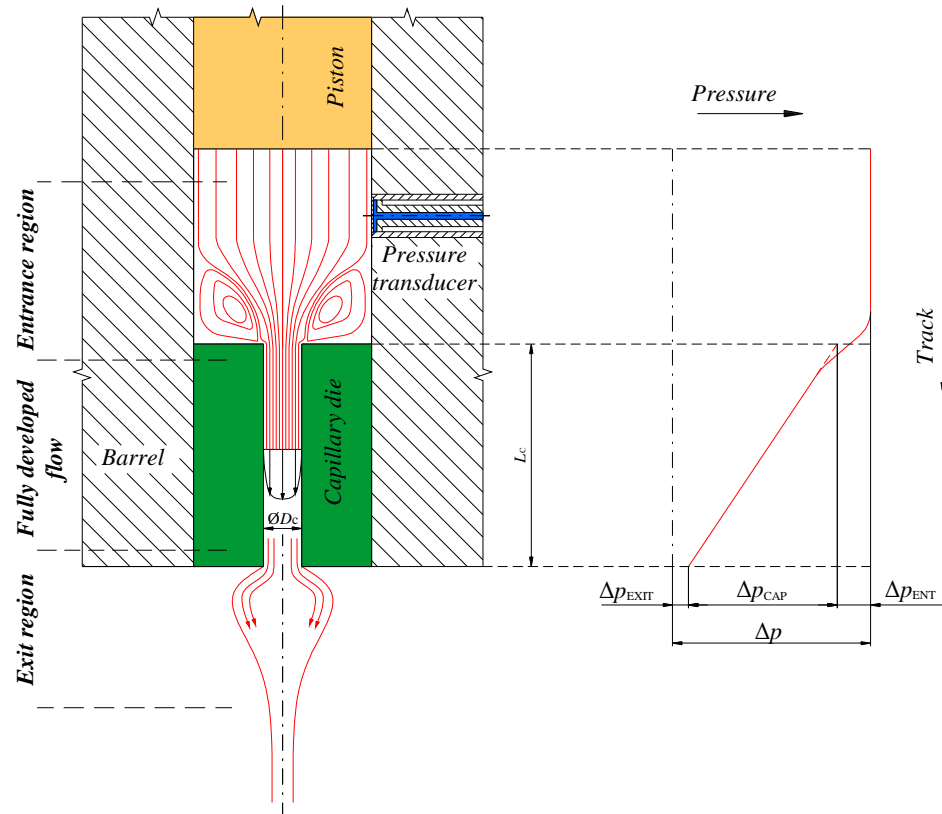


Fig. 20: The behaviour of pressure along the capillary

As introduced above, in capillary rheometers the pressure transducers are placed only in die entry regions. Therefore, only the total pressure drop (Δp) can be measured.

2.2 Extensional viscosity

Extensional viscosity, which represents the resistance of melt to stretching, is one of the most important properties of polymer melts. The extensional viscosity measurement on capillary rheometer is very complicated due to non-existence of a homogenous extensional flow region; therefore the extensional viscosity cannot be measured directly. However, in the entrance region of the capillary die, the material elements are significantly stretched due to an abrupt contraction, which enables, with some difficulties, determination of the property. In order to calculate the extensional viscosity from entrance pressure drop, three basic analyses were developed by Cogswell [29], Binding [31] and Gibson [32]. These techniques are based on many simplifications and assumptions.

Extensional viscosity determined in a capillary rheometer is not as accurate as from pure extensional rheometers but on the other hand no extensional viscosity devices measure at such high extensional rates as capillary rheometers [20].

2.2.1 Entrance viscosity

As introduced above, extensional viscosity determination in capillary rheometer is based on the entrance pressure drop which can be either measured directly (in the case of orifice capillary die) or extract from Bagley plot (for more details see *Chapter 2.6.1*). The entrance viscosity is a basic quantity which allows to calculate the extensional viscosity. It can be expressed as [33]:

$$\eta_{\text{ENT}} = \frac{\Delta p_{\text{ENT}}}{\dot{\gamma}_{\text{APP}}} \quad (21)$$

where $\dot{\gamma}_{\text{APP}}$ is apparent shear rate, which is defined below by Eq. (50).

In a capillary rheometer, it is very difficult to determine the entrance viscosity at very slow apparent shear rates due to problems connected with sensitivity of pressure transducers. For this reason, the fit of entrance viscosity by a suitable model can be used. An equation which can successfully be used to fit the entrance viscosity dependence on apparent shear rate was suggested in [33] and has the following form:

$$\log(\eta_{\text{ENT}}) = \log \left\{ \frac{\eta_{\text{ENT},0}}{\left[1 + (\lambda' \dot{\gamma}_{\text{APP}})^{a'}\right]^{\frac{1-n'}{a'}}} \right\} \left[\frac{\tanh(\alpha \dot{\gamma}_{\text{APP}} + \beta')}{\tanh(\beta')} \right]^{\xi'} \quad (22)$$

This empirical model is combination of the well-known Carreau-Yasuda model and an additional term, which allows to control the strain-hardening behavior; $\eta_{\text{ENT},0}$ represents the plateau-value of entrance viscosity, and λ' , a' , n' , α' , β' , ξ' are adjustable parameters.

As also suggested in [33], Eq. (22) can be simplified into:

$$\log(\eta_{\text{ENT}}) = \log \left\{ \frac{\eta_{\text{ENT},0}}{\left[1 + (\lambda' \dot{\gamma}_{\text{APP}})^{a'}\right]} \right\} \left[\frac{\tanh(\alpha \dot{\gamma}_{\text{APP}} + 1)}{\tanh(1)} \right]^{\xi'} \quad (23)$$

Here, term a' is equal to $1 - n'$ and term β' is equal to 1.

2.2.2 Cogswell's analysis

Definition sketch of flow geometry which was used by Cogswell is depicted in *Fig. 21* (adapted from [29]). It is clear that the extensional character of flow is along the centerline. For many fluids, recirculation vortices in the corners are created. In these cases, the main flow is through a funnel-shape section near the center of the flow field.

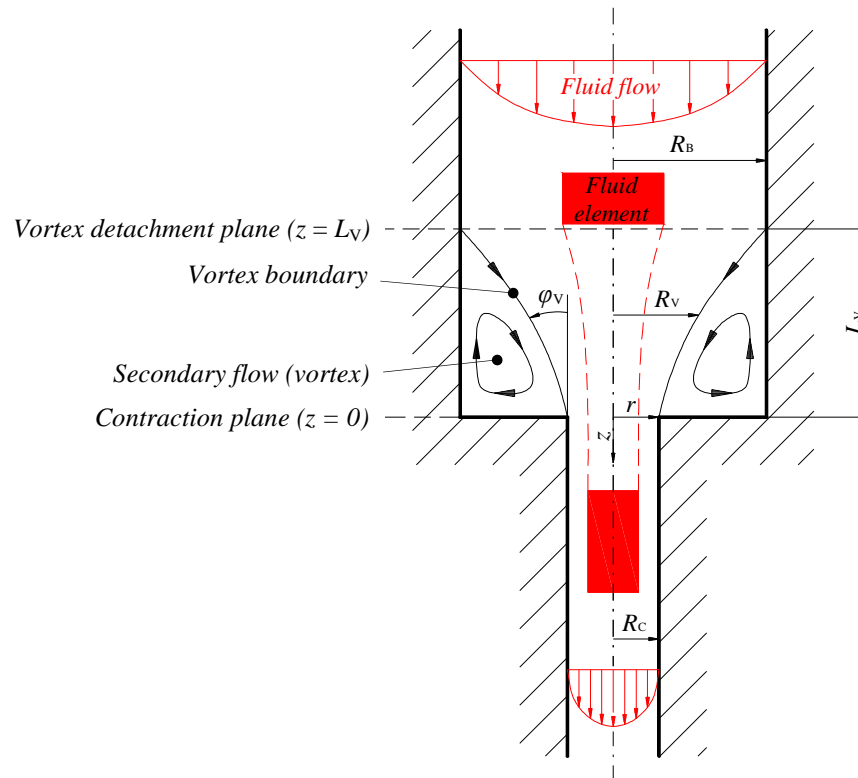


Fig. 21: Definition sketch of entry flow

On the boundary between vortices and the funnel-shaped flow region the velocity is not equal zero but its value is small and in comparison with centreline velocity it can be neglected.

In Cogswell's analysis [29] it is assumed that fluid flows through an abrupt contraction with minimal pressure requirements. This is the simplest technique of entrance flow which calculates the entrance pressure drop (Δp_{END}) as a direct summation of two pressure drops: one due to shear viscosity and the other due to extensional viscosity. Cogswell calculated each of pressure drops individually when he extracted a differential section of the funnel-shaped entry flow region, applied force balance and finally integrated over the whole entry section. For successful solution, Cogswell used many assumptions which are summarized in *Tab. 1* [19].

Tab. 1: Assumptions of Cogswell's entry flow analysis

-
-
1. Incompressible fluid;
 2. Funnel-shaped flow; no slip ($v_z = 0$) on funnel surface;
 3. Unidirectional flow in funnel region;
 4. Fully developed flow upstream and downstream;
 5. Axis symmetry;
 6. Pressure drops due to shear and elongation may be calculated separately and summed to given total entrance pressure loss;
 7. Neglected Weissenberg-Rabinowitsch correction, $\dot{\gamma} = \dot{\gamma}_{APP} = \frac{4Q}{\pi R_C^3}$;
 8. Shear stress is related to shear rate through a power law, $\tau_{Rz} = \bar{m} \dot{\gamma}_{APP}^{\bar{n}}$;
 9. Elongational viscosity is constant;
 10. Shape of funnel is determined by the minimum generated pressure drop;
 11. No effect of elasticity (shear normal stresses neglected);
 12. Inertia neglected.
-
-

Based on these assumptions, relationships for extensional viscosity determination were derived as follows. The extensional rate is expressed as:

$$\dot{\epsilon} = \frac{4}{3(n+1)} \frac{\eta \dot{\gamma}_{APP}}{\eta_{ENT}} \quad (24)$$

where η stands for shear viscosity, which is defined by Eq. (52), and n expresses power-law index:

$$n = \frac{d(\log \tau_{Rz})}{d(\log \dot{\gamma}_{APP})} \quad (25)$$

where τ_{Rz} is the shear stress at the capillary wall, which is defined by Eq. (46). The extensional stress is:

$$\sigma_E = \frac{3}{8} (n+1) \eta_{ENT} \dot{\gamma}_{APP} \quad (26)$$

and finally, the desired extensional viscosity:

$$\eta_E = \frac{\sigma_E}{\dot{\epsilon}} \quad (27)$$

This method is deeply investigated in open literature [34], [35], [36] and [37] and also compared with other extensional viscosity determination techniques. Based on these research reports, it seems that the Cogswell's analysis for particular polymer can be fairly precise at high rates but fails in lower rates.

2.2.3 Binding's analysis

Binding [31] rose from Cogswell's analysis but he allowed the elongation viscosity to vary with the deformation rate and he did not neglect Weissenberg - Rabinowitsch correction (for more details about this correction see *Chapter 2.6.2*). The definition sketch of entry flow used by Binding is the same as Cogswell (see *Fig. 21*). Binding focused on recirculating of regions or vortices in which the energy is dissipated and this loss in energy is reflected as an entrance pressure drop (Δp_{ENT}). Therefore, this analysis is based on minimizing of the viscous energy dissipation in the converging region. Assumptions used by Binding are summarized below [19].

Tab. 2: Assumptions of Binding's entry flow analysis

-
1. Incompressible fluid;
 2. Funnel-shaped flow; no slip ($v_z = 0$) on funnel surface;
 3. Unidirectional flow in funnel region (see assumption 10);
 4. Fully developed flow upstream and downstream;
 5. Axis symmetry;
 6. Shear viscosity is related to shear rate through a power law, $\eta = \bar{m}\dot{\gamma}_{\text{COR}}^{\bar{n}-1}$;
 7. Elongational viscosity is given by power-law, $\eta_E = \bar{l}\dot{\epsilon}^{\bar{k}-1}$;
 8. Shape of funnel is determined by the minimum work to drive flow;
 9. No effect of elasticity (shear normal stresses neglected);
 10. Quantities $\left(\frac{dR_V}{dz}\right)^2$ and $\frac{dR_V^2}{dz^2}$ related to funnel shape are neglected; this has the implication that the radial velocity is neglected when calculating the rate of deformation;
 11. Neglect of energy required to maintain corner circulation;
 12. First normal stress difference due to the shear flow is neglected ($N_1 = 0$);
 13. Inertia neglected.
-

The final equations which allow to determined extensional viscosity curve are following. The extensional rate along the centerline can be calculated from:

$$\dot{\epsilon} = \frac{(3n+1)(1+k)^2}{3k^2(1+n)^2} \frac{\eta \dot{\gamma}_{APP}}{\eta_{ENT}} \left(\frac{3n+1}{4n} \right)^n \quad (28)$$

Subsequently, the extensional stress is formulated as:

$$\sigma_E = \frac{2^{(k-1)} 3k(1+n)^2}{(3n+1)(1+k)^2} \frac{\eta_{ENT} \dot{\gamma}_{APP}}{I_{nk}} \quad (29)$$

where integral I_{nk} is given as:

$$I_{nk} = \int_0^1 \left\{ \text{abs} \left[2 - \left(\frac{3n+1}{n} \right) \zeta^{\frac{(1+n)}{n}} \right] \right\}^{(k+1)} \zeta d\zeta \quad (30)$$

The unknown parameter k in Eqs. (28), (29) and (30) is determined from the following equation:

$$k = \frac{t'}{1+n-t'} \quad (31)$$

where t' is formulated as:

$$t' = \frac{d \log(\eta_{ENT})}{d \log(\dot{\gamma}_{APP})} - 1 \quad (32)$$

As shown in [33], Eq. (30) can be simplified, when $n \in (0;1)$ into:

$$I_{nk} = \frac{n \left[\frac{(1+n)}{n} \right]^{(k+1)}}{2n + (1+n)(k+1)} \quad (33)$$

The extensional viscosity is then determined from Eq. (27).

The extensional viscosity obtained from Binding's analysis is discussed in [35], [37] and [38]. It has been found that the Binding model is quite reasonable in the case of shear-thinning fluids but for elastic fluids (called *Boger fluids*) is not accurate enough. On the other hand, for commonly used polymers, such as linear low density polyethylene Binding's analysis has been found to be more precise than Cogswell's analysis [39].

2.2.4 Gibson's analysis

In order to estimate the extensional viscosity of glass fiber filled polymer melts, commonly used in the injection molding technology, Gibson [32] derived another analysis of entry flow. The definition scheme of entry flow region employed by Gibson is illustrated in *Fig. 22*. As can be seen, this analysis enables to vary the entry die angle. Furthermore, Gibson assumed no vortices in the entry region, thus he applied sink flow kinematics to estimate the entrance pressure drop (Δp_{ENT}). He assumed that entrance pressure drop is mainly caused by extensional flow, which does not strongly depend on the velocity across the die. Originally, Gibson used cylindrical coordinates for his calculations, but to describe entry flow behaviour over the full range of possible die semi-angles up to 90° he successfully applied the spherical coordinates.

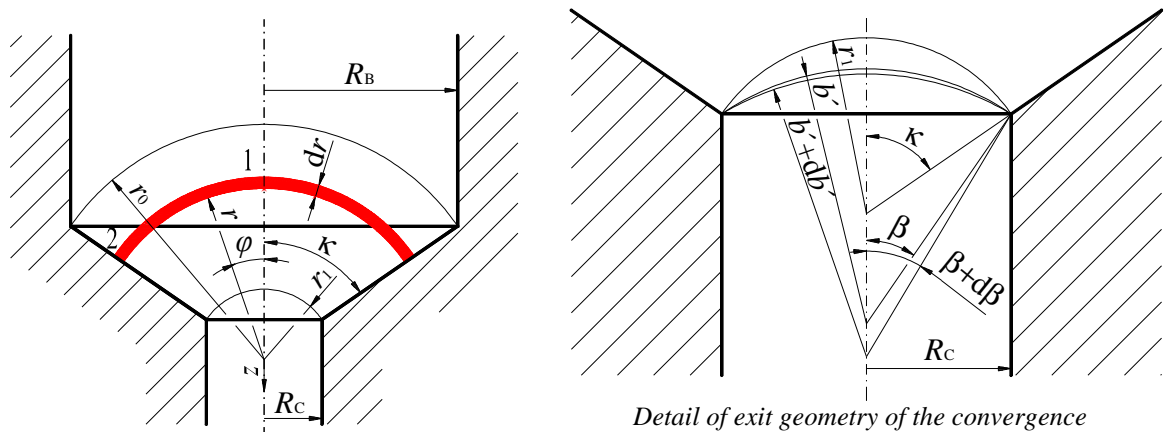


Fig. 22: Definition scheme of entry flow in Gibson's analysis

Gibson, as well as Cogswell and Binding, performed many assumptions which are summarized in the following table.

Tab. 3: Assumptions of Gibson's entry flow analysis

-
-
1. Incompressible fluid;
 2. Sink flow; no slip ($v_z = 0$) at wall surface;
 3. Unidirectional flow in entry region;
 4. Fully developed flow upstream and downstream;
 5. Spherical coordinates;
 6. Axis symmetry;
 7. Shear viscosity is related to shear rate through a power law, $\eta = \bar{m}\dot{\gamma}_{\text{COR}}^{\bar{n}-1}$;
 8. Neglected vortices in entry region;
 9. No effect of elasticity (shear normal stresses neglected);
 10. First normal stress difference due to the shear flow is neglected ($N_1 = 0$);
 11. Inertia neglected.
-
-

The basic relationships which lead to determination of extensional viscosity are in general form (die entry angle can be varied from 0° to 90°) formulated in the following equations. The extensional rate is:

$$\dot{\epsilon} = \frac{1}{4} \dot{\gamma}_{\text{APP}} \sin(\kappa) [1 + \cos(\kappa)] \quad (34)$$

and the extensional stress:

$$\sigma_E = \frac{\overline{\eta_{\text{ENT}}} \dot{\gamma}_{\text{APP}}}{\frac{2}{3k'} \left[1 - \left(\frac{R_C}{R_B} \right)^{3k'} \right] + \frac{I(k', \kappa)}{\{\sin(\kappa)[1 + \cos(\kappa)]\}^{k'}}} \quad (35)$$

where R_B is the barrel radius, κ is the entrance angle (see Fig.22) and term $I(k', \kappa)$ is given as:

$$I(k', \kappa) = \int_0^\kappa [1 + \cos(\beta)]^{k'-1} [\sin(\beta)]^{k'+1} d\beta \quad (36)$$

Term $\overline{\eta}_{\text{ENT}}$ in Eq. (35) is the entrance viscosity calculated from the entrance pressure drop arising from extensional flow, and it is given by the relation:

$$\overline{\eta}_{\text{ENT}} = \eta_{\text{ENT}} \frac{2\eta[\sin(\kappa)]^{3n} \left[1 - \left(\frac{R_C}{R_B} \right)^{3n} \right]}{3n \left(\frac{\pi}{2} \right)^{3n+1}} \left(\frac{3n+1}{4n} \right)^n \quad (37)$$

Finally, the unknown parameter k' is formulated as:

$$k' = \frac{\text{dlog}(\overline{\eta}_{\text{ENT}})}{\text{dlog}(\dot{\gamma}_{\text{APP}})} + 1 \quad (38)$$

The main advantage of Gibson's model is its capability to properly predict Trouton ratio for isotropic fluids (which is useful for melt anisotropy quantification) and possibility to take entrance angle correctly into account (see the following research papers for more detail of model analysis [40], [41]).

2.2.5 Haul-off Rheotens

Haul-off Rheotens is another technique to estimate extensional viscosity. Furthermore, with the aid of this technique, the rupture tensile stress can also be determined.

As can be seen in *Fig. 23*, the principle of this technique is uniaxial stretching of filament. Polymer melt is extruded by the piston with velocity (v_E) and led to a pulley which is placed on a balance. Finally, it is wound-up by dual drums which have velocity v_D . If $v_D > v_E$ thus, force F_S can be determined by the balance.

The tensile stress in the filament is given by following equation [42]:

$$\sigma_T = \frac{F_S}{A_0} V \quad (39)$$

where A_0 represents the cross-section area of the die and V is the draw ratio defined as:

$$V = \frac{v_D}{v_E} \quad (40)$$

where v_D is the drawdown velocity and v_E is the exit velocity.

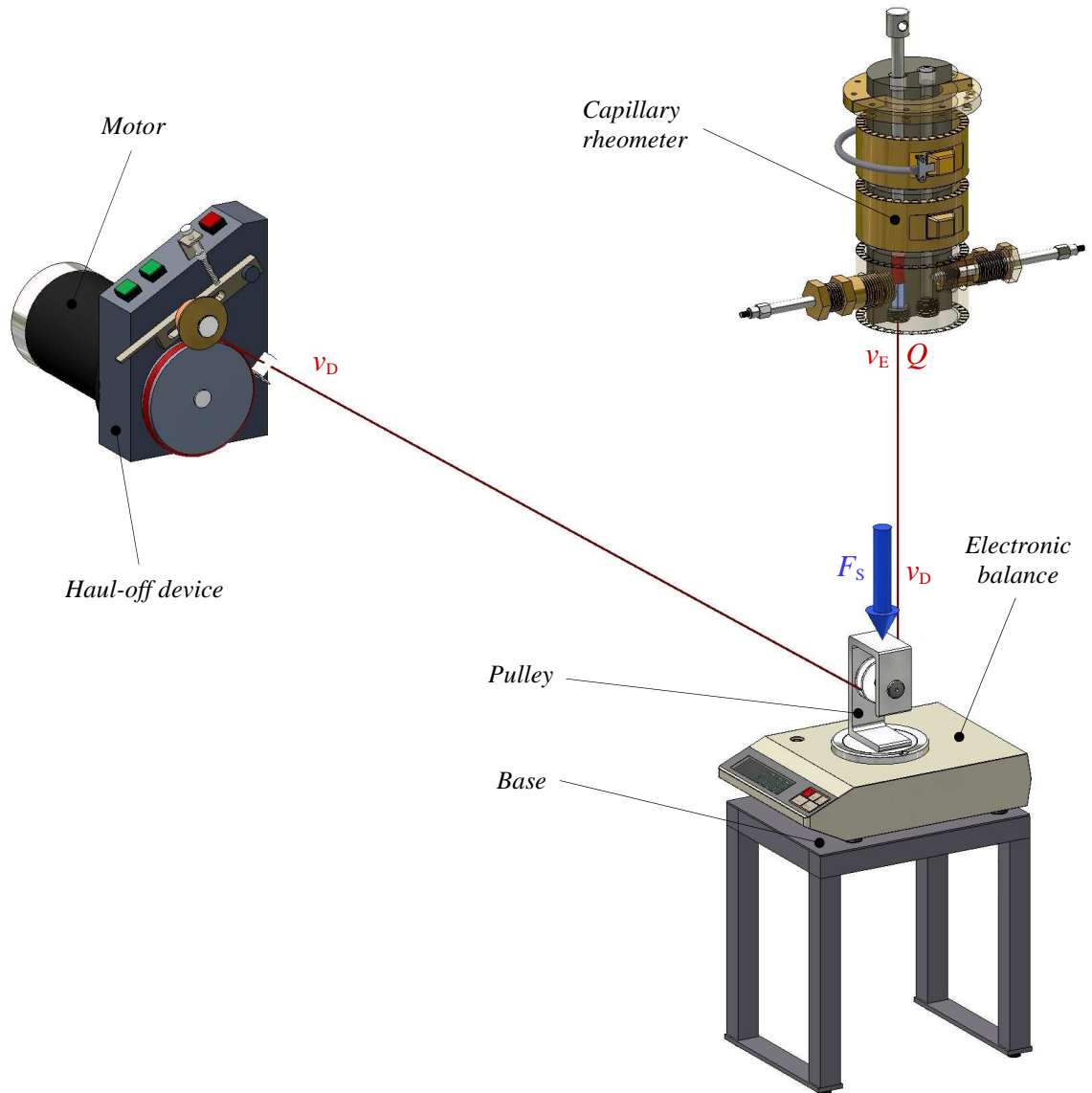


Fig. 23: Principle of Haul-off Rheotens measuring technique of extensional viscosity and rupture stress

If the tensile stress is plotted in dependence on draw ratio, a tensile curve is obtained. In this curve, draw resonance region (force F_s oscillates) as well as rupture stress (maximum tensile stress value before the filament rupture) can be found. The start of draw resonance and rupture stress is crucially important in some polymer processing, such as fibre spinning or film blowing.

In order to determine apparent extensional viscosity at the end of the spinline ($x = L$), Wagner *et al.* [42] proposed the following relation:

$$\eta_E(L) = \frac{\sigma_P}{\left(\frac{v_E}{L}\right)\left(\frac{V_P}{V_S}\right)} \left(\frac{V}{V_P}\right)^{\frac{m'-1}{m'}} \quad (41)$$

where σ_P is the critical tension, L represents the length of the spinline, V_P stands for the critical draw ratio, m' symbolizes power-law index in melt tension dependence on extensional rate, and V_S expresses the extrapolated starting point of the drawdown:

$$V_S = \frac{v(x=0)}{v_E} \quad (42)$$

The extensional rate at the end of the spinline ($x = L$) is:

$$\dot{\epsilon} = \frac{v_E}{L} (V_P - V_S) \left(\frac{V}{V_P}\right)^{\frac{1}{m'}} P(V) \quad (43)$$

where $P(V)$ is defined as:

$$P(V) = 1 + \frac{m'}{(m'-1)(V_P - V_S)} \left[\left(\frac{V}{V_P}\right)^{\frac{m'-1}{m'}} - 1 \right] \quad (44)$$

Although this technique provides reasonable results, the measured quantities are dependent on the velocity of piston, shape and length of capillary die and distance between capillary die and balance.

2.3 Shear viscosity

Shear viscosity is another important property of polymer melts which expresses the resistance of polymer melt to the shear flow. In capillary rheometry the shear viscosity is determined from shear stress and shear rate.

2.3.1 Shear stress

In order to derive the relationship for shear stress, the differential ring shape element will be considered. Furthermore, the *Poiseuille flow* in a circular flow channel (capillary die) will be assumed. In this case, cylindrical coordinates are the most advantageous (for explanation see *Fig. 24*). Moreover, several assumptions, which are summarized in *Tab. 4* [19], will be taken into account.

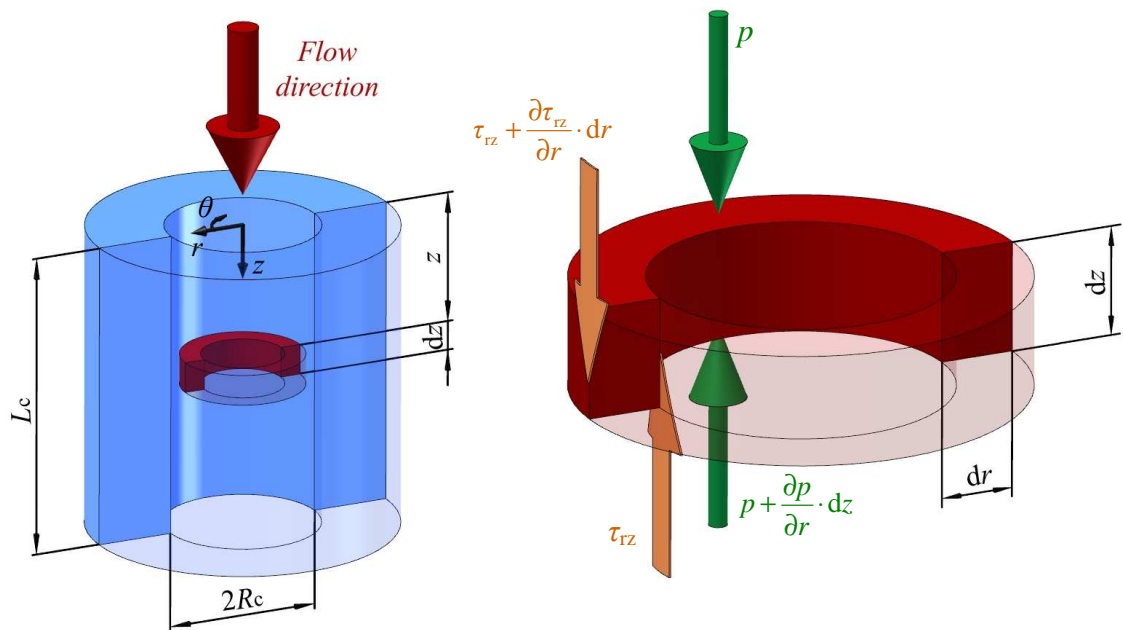


Fig. 24: Differential ring shape element in a capillary and forces acting on it.

Tab. 4: Assumptions for Poiseuille flow in a capillary die

-
1. Unidirectional flow;
 2. Incompressible fluid;
 3. θ symmetry;
 4. Long capillary die (z – variation is negligible);
 5. Symmetric stress tensor;
 6. $\frac{\partial p}{\partial z} = \text{constant}$;
 7. Zero stress at $r = 0$.
-

If the momentum conservation equation is applied on this element and the infinitely small second order quantities are neglected, after derivation the formulation for shear stress will be obtained [20]:

$$\tau_{rz} = \frac{\Delta p_{CAP}}{2L_C} r \quad (45)$$

where L_C is length of capillary die, r expresses the radius which can vary from 0 (axis of capillary die) to R_C (capillary die wall). In the case of $r = R_C$, the shear stress changes to wall shear stress:

$$\tau_{Rz} = \frac{\Delta p_{CAP}}{2L_C} R_C \quad (46)$$

As mentioned above, in a capillary rheometer the pressure transducers are located above the capillary (in entrance region), thus only the total pressure drop is measured. Therefore, from the measured data it is possible to determine only the apparent shear stress:

$$\tau_{RzAPP} = \frac{\Delta p}{2L_C} R_C \quad (47)$$

Eq. (46) presents Eq. (47) with applied Bagley correction (for more details see *Chapter 2.6.1*).

2.3.2 Shear rate

In order to determine the shear rate at the capillary wall it is necessary to express velocity $v_z(r)$ along coordinate r and then to seek the expression for $r = R_C$. If the velocity field is known, the apparent wall shear rate $\dot{\gamma}_{APP}$ can be directly calculated. The simplest calculation is for Newtonian fluids, where the velocity profile is parabolic [19]:

$$v_z(r) = \frac{2Q}{\pi R_C^3} \left[1 - \left(\frac{r}{R_C} \right)^2 \right] \quad (48)$$

where Q is the volume flow rate. Now, the derivative of this equation according to coordinate r is outlined:

$$\dot{\gamma} = \frac{dv_z}{dr} = \frac{4Q}{\pi R_C^3} \frac{r}{R_C} \quad (49)$$

and finally, Eq. (49) rewritten for $r = R_C$ has the following form:

$$\dot{\gamma}_{APP} = \frac{4Q}{\pi R_C^3} \quad (50)$$

This equation is necessary to adapt for non-Newtonian fluids by Weissenberg-Rabinowitsch correction, which is elaborately described in *Chapter 2.6.2*.

The shear viscosity is obtained as the shear stress divided by shear rate. In the case of apparent (uncorrected) shear viscosity, the apparent shear stress, Eq. (47), and apparent shear rate, Eq. (50), are used:

$$\eta_{APP} = \frac{\tau_{RZAPP}}{\dot{\gamma}_{APP}} \quad (51)$$

The shear stress after Bagley correction, Eq. (46), and shear rate after Weissenberg-Rabinowitsch correction, Eq. (63), allow to calculate true shear viscosity:

$$\eta = \frac{\tau_{Rz}}{\dot{\gamma}_{COR}} \quad (52)$$

2.4 First and second normal stress differences

In the case of shear flow of polymer melts as a typical representative of viscoelastic fluids, normal stresses, perpendicular to flow direction, arise. Therefore, first and second normal stress differences are non-zero.

In order to determine the first and second normal stress differences, the slit geometry modification of capillary rheometer can be used. In this case the circular die is replaced by rectangular channel or slit die. The real view is shown in *Fig. 25*. It is evident that three or four pressure transducers are placed at the slit die wall.

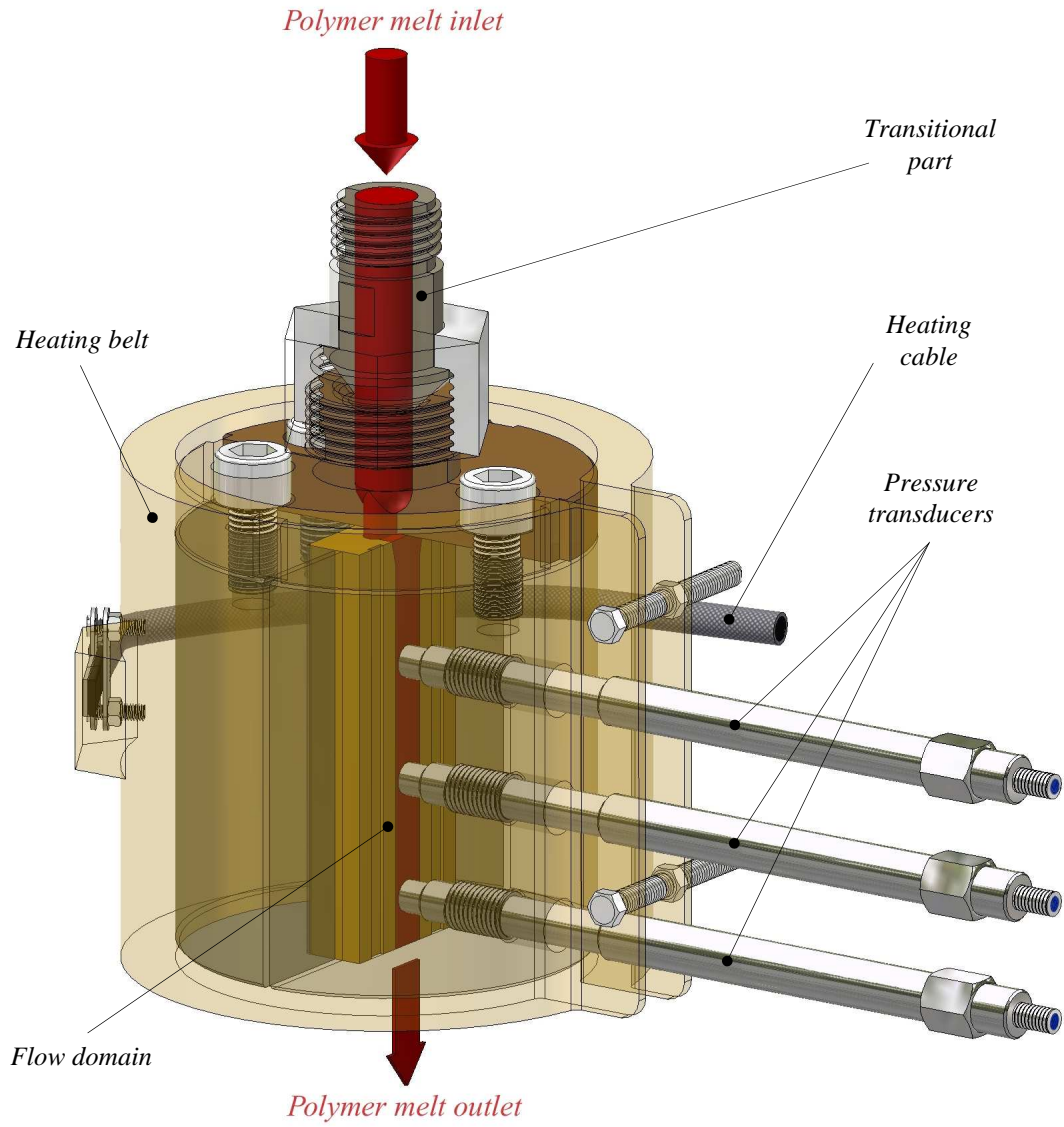


Fig. 25: Real view of slit die

For this geometry the wall shear stress (in slit die) is obtained through the pressure gradient [20]:

$$\tau_w = \frac{H_s}{2 \left(1 + \frac{H_s}{W_s} \right)} \frac{dp}{dz} \quad (53)$$

where H_s is the height of the slit die, W_s represents the width of the slit die, and $\frac{dp}{dz}$ stands for the pressure gradient along the length of the slit die.

The wall shear rate is calculated from volumetric flow rate:

$$\dot{\gamma}_{APP} = \frac{6Q}{W_S H_S^2} \quad (54)$$

The shear viscosity determination is described in *Chapter 2.3*. Here, the wall shear stress is true (end correction is not necessary to use), but the shear rate is apparent and the Weissenberg – Rabinowitsch correction for rectangular channel [20] must be used.

As a consequence of pressure transducers location on the wide flat sides of the slit die, direct measurement of pressure gradient is possible, which is the main advantage of this geometry. The pressure behaviour along the length of slit die is depicted in *Fig. 26*. The pressure data from transducers can be fitted by a linear function and the exit pressure (Δp_{EXIT}) is found at the exit plane. However, in the case of high pressures (compressibility of melts) or existence of dissipation, the data must be fitted by a non-linear function [43].

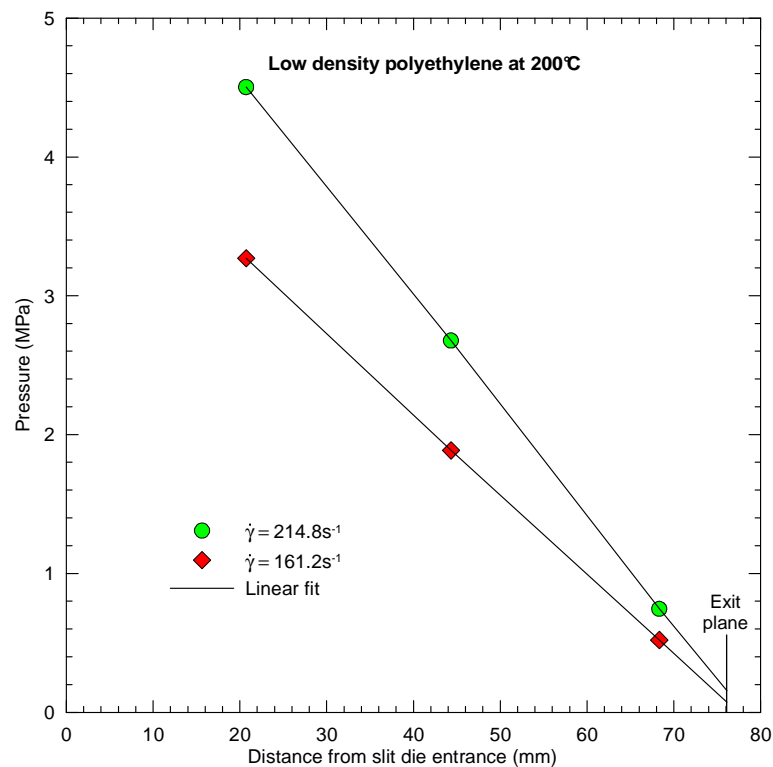


Fig. 26: Pressure profile along the slit die (taken from [44])

In order to determine both normal stress differences, two basic techniques can be used. Firstly, the exit pressure (Δp_{EXIT}) obtained from linear pressure data fit (see *Fig. 26*) is applied. Normal stresses determination from this part of total pressure drop is possible to use because the tension along streamlines causes extrudate swell in elastic liquids as well

as the exit pressure. In the case of polymer melts, this method allows acquiring N_1 at higher shear rates than in rotational rheometers. The relationship for determination of N_1 is [30]:

$$N_1 = p_{\text{EXIT}} \left(1 + \frac{d \ln p_{\text{EXIT}}}{d \ln \tau_w} \right) \quad (55)$$

The simplification of this equation is based on neglecting of fluid inertia and any velocity profile rearrangements up to the die exit.

It should be noted that due to the physical limitation of pressure transducers, the measurement of exit pressure is very difficult and inaccurate since its values are very small. Therefore, this method can only be used for the shear stresses $\tau_w > 25$ kPa [44]. As can be seen in *Fig. 27*, the errors at lower shear stresses at the wall are significant.

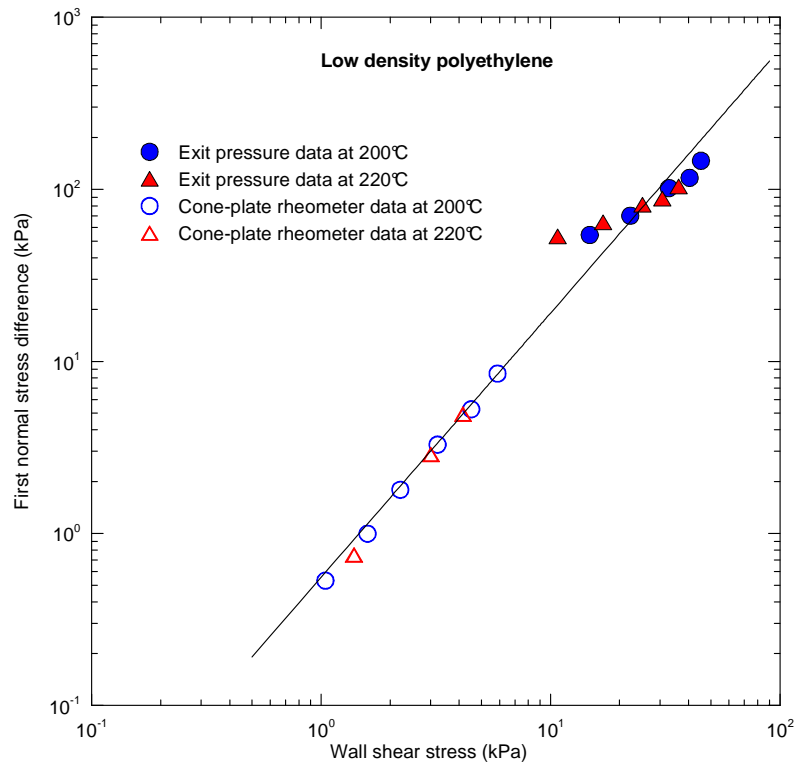


Fig. 27: First normal stress difference versus shear stress for low density polyethylene (taken from [44])

Furthermore, the difference in pressure at the recessed and flush transducers can be used. This error was firstly observed by Broadbent *et al.* [28]. For Newtonian fluids the pressures at these two transducers are the same but for elastic liquids the non-zero first and second normal stress differences cause a variance in pressures, as shown in *Fig. 28*. It is well known that in shear flow elastic fluid creates tension along flow streamlines.

The pressure hole results from the slight bending of the flow streamlines near the pressure hole entrance, which is a consequence of non-zero normal stresses incline to lift up the fluid here.

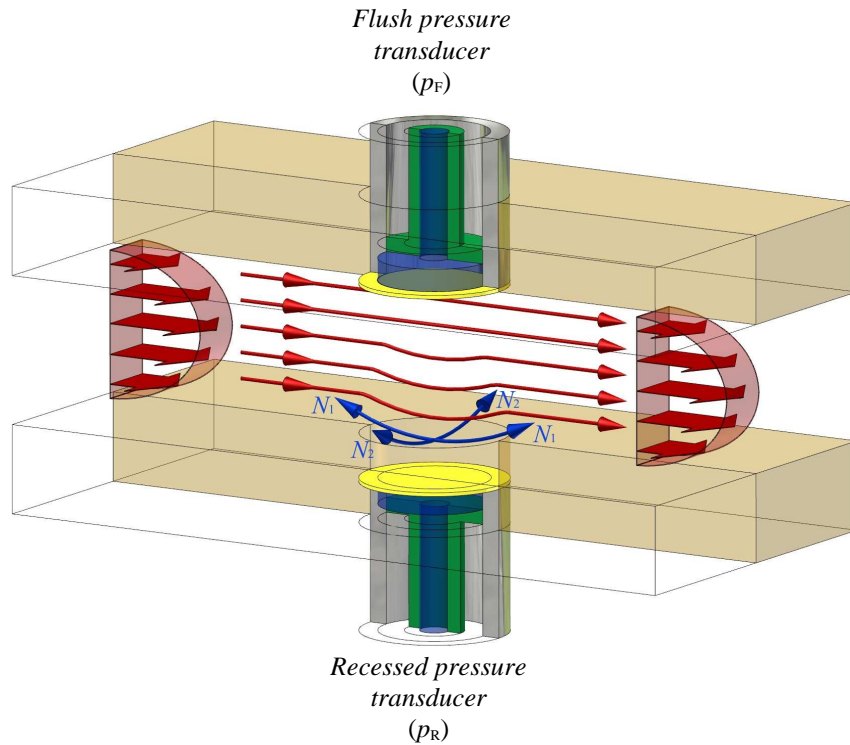


Fig. 28: Pressure hole geometry

As a result of this phenomenon, the pressure in the hole (p_R) is lower than the pressure on the slit die wall (p_F). The difference between these pressures gives the hole pressure [20]:

$$p_H = p_F - p_R \quad (56)$$

For the hole pressure measurements various types of hole can be used. Three most frequently used types are shown in Fig. 29 (adapted from [20]). However, N_1 and N_2 determination is not the same for each of them because the normal stress differences depend on how the streamlines are bent. Hence, for a long narrow gap transverse to flow direction, Fig. 29 a), N_1 is specified by the following equation:

$$N_1 = 2mp_H \quad (57)$$

where m is defined as:

$$m = \frac{d \ln p_H}{d \ln \tau_w} \quad (58)$$

For the case of gap parallel to flow, *Fig. 29 b)*, N_2 can be determined by the following relationship:

$$N_2 = -mp_H \quad (59)$$

For a circular hole, the streamlines are bent in both directions, *Fig. 29 c)*, therefore N_1 and N_2 are contained in relation:

$$N_1 - N_2 = 3mp_H \quad (60)$$

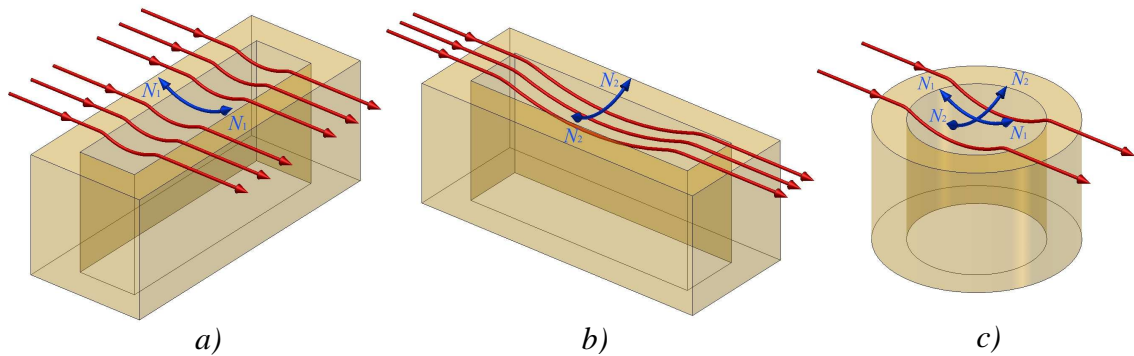


Fig. 29: Most frequently used pressure hole types: (a) transverse to flow, (b) parallel to flow, (c) circular

The results of first and second normal stress differences measurement by using exit as well as hole pressure is shown in [45] and [46].

2.5 Wall slip

Wall slip is a phenomenon in which the velocity in the shear flow at the wall is non-zero. The standard flow in capillary die is free of wall slip. However, in many cases this condition may be infringed.

For better understanding of wall slip phenomenon, *Fig. 30* (adapted from [19]), is outlined. In the case of wall slip, as compared to the no slip case, the shear rate is reduced throughout, but especially near the wall.

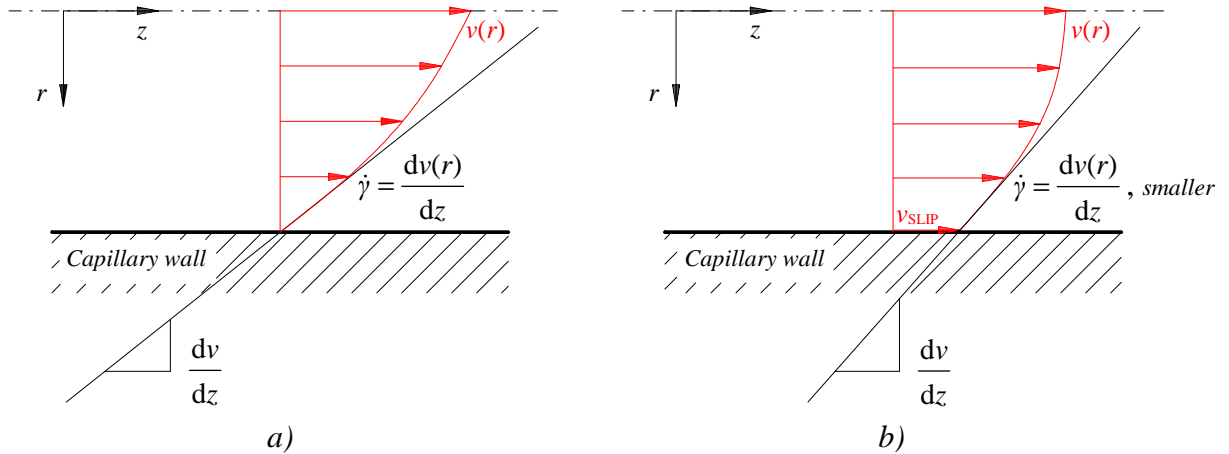


Fig. 30: Shear flow in capillary die with (a) no slip and (b) slip at the wall

The start of the wall slip is connected with achievement of critical shear stress at the wall. This is depicted in Fig. 31, which shows that in small values of shear stress there is no slip, but with higher shear stresses the slip occurs (the apparent shear rate changes from a constant value to linear dependence of inverse radius).

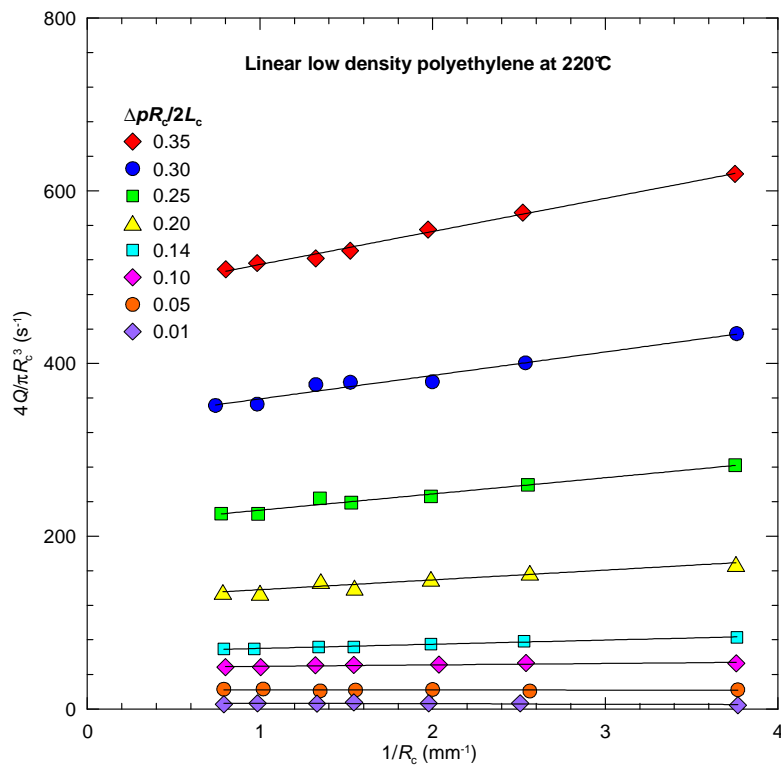


Fig. 31: Dependence of apparent shear rate on inverse capillary radius at various shear stresses for low density polyethylene (taken from [19])

It should be noted that the slip may not necessarily occur continuously, it may alternate with adhesion. It is typical for polymer melts or concentrated solutions at high shear stresses and is called the *stick-slip phenomenon*. Another similar phenomenon can be observed in the flow of multicomponent materials. In this case, low-viscosity material is diffused to a capillary wall and may affect preferentially shearing between low-density material and the wall, which leads to a change of velocity profile.

Direct observation of velocity behaviour near the die wall is difficult, thus indirect determination of slip is performed with the aid of two capillaries which have various radii (R_C) and identical (L_C/D_C) ratio. With these capillaries a set of measurements is carried out when the apparent shear rate is changed.

2.6 Corrections used in capillary rheometry

The relationships for determination of shear viscosity and also other quantities on capillary rheometer are derived for the ideal measurement conditions (see *Tab. 4*). In reality, measurements show a lot of deviations from ideal requirements. To eliminate these deviations it is necessary to use a number of corrections.

2.6.1 Bagley correction

As introduced in *Chapter 2.1*, total pressure drop (Δp) which is measured by pressure transducer in the entrance region consists from three parts - *entrance*, *capillary* and *exit* pressure drops. In order to precisely determine shear viscosity, only capillary pressure drop is necessary to obtain. This is possible to reach by two methods. Firstly, direct measurement of end pressure drop (Δp_{END}) with the aid of orifice capillary die [14], the scheme of which is presented in *Fig. 32 (right)*.

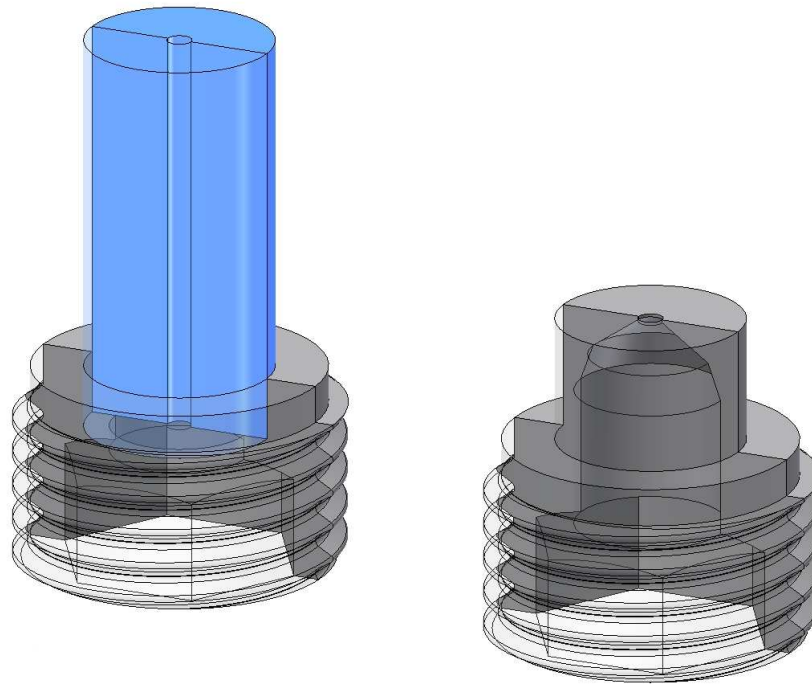


Fig. 32: Schematic view of typical capillary dies set: long capillary (left) and orifice capillary (right)

Secondly, indirect determination of end pressure drop is possible by using Bagley plot [47]. Thus, Bagley correction is the correction for capillary entrance and exit effects. The principle of Bagley correction is depicted in *Fig. 33*. Practically, the process of Bagley plot determination is based on the total pressure drop measurement on two or three capillary dies which have the same diameters (D_c) but different length to diameter ratio (L_c/D_c). Afterwards, the measured pressure drops are plotted as a dependence on (L_c/D_c). These two or three points in Bagley plot are extrapolated by linear fit and finally, the required end pressure drop (Δp_{END}) is found on the vertical axis (Δp). Thus, the capillary pressure drop is obtained through the following equation:

$$\Delta p_{\text{CAP}} = \Delta p - \Delta p_{\text{END}} \quad (61)$$

It should be noted that in literature [14], [48] it is possible to find not only linear fit but also nonlinear fit which is more precise than the former.

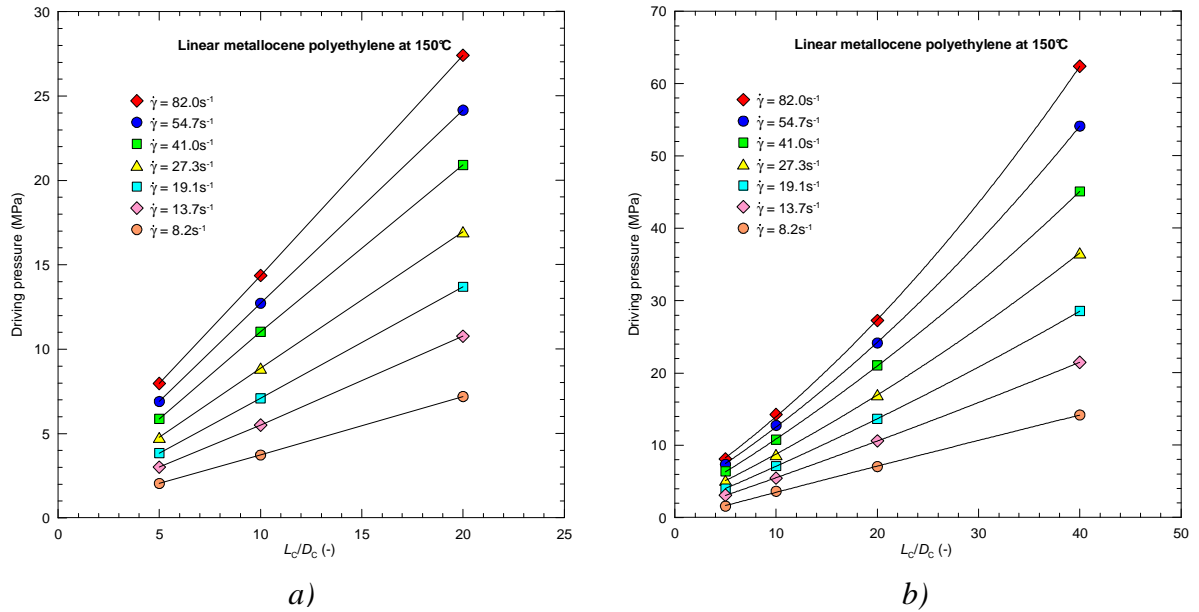


Fig. 33: Linear fit (a) and quadratic fit (b) in Bagley plots (taken from [14])

2.6.2 Weissenberg - Rabinowitsch correction

In Chapter 2.3.2 the calculation of shear rate is suggested only for Newtonian fluids with parabolic velocity profile. However, in the case of non-Newtonian fluids (polymer melts), the shape of velocity profile is non-parabolic, thus the general determination of shear rate must be done by Weissenberg – Rabinowitsch correction. This correction takes into account the equation for flow rate in a tube:

$$Q = 2\pi \int_0^{R_C} v_z(r) r dr \quad (62)$$

The whole derivation of this relationship is shown in [19]. As a result, the following expression is obtained:

$$\dot{\gamma}_{COR} = \frac{4Q}{\pi R_C^3} \left(\frac{3n+1}{4n} \right) \quad (63)$$

The second term on the right side is called Weissenberg – Rabinowitsch correction. In the case of Newtonian fluids, parameter n is equal 1, thus Eq. (63) has the same form as Eq. (50).

2.6.3 Effective entry length correction

As shown in [33], Cogswell's and Binding's extensional viscosity determination techniques do not precisely predict Trouton ratio value of 3 for the ratio of extensional viscosity to shear viscosity at low shear rates (Newtonian plateau range). Thus, the measured entrance viscosity data for Cogswell and Binding methods must be modified by *effective entry length correction* which has recently been proposed in [33]:

$$\eta_{\text{ENT,C}} = \frac{4\eta \left(\frac{L_{\text{LC}}}{D_{\text{LC}}} \right)_{\text{b}} \left[\left(\frac{L_{\text{C}}}{D_{\text{C}}} \right)_{\text{Tr}} - \left(\frac{L_{0\text{C}}}{D_{0\text{C}}} \right)_{\text{a}} \right]}{\left(\frac{L_{\text{LC}}}{D_{\text{LC}}} \right)_{\text{b}} - \left(\frac{L_{0\text{C}}}{D_{0\text{C}}} \right)_{\text{a}}} + \eta_{\text{ENT,a}} \quad (64)$$

where η stands for shear viscosity, $\left(\frac{L_{0\text{C}}}{D_{0\text{C}}} \right)_{\text{a}}$ expresses ratio of length to diameter at orifice

capillary and $\left(\frac{L_{\text{LC}}}{D_{\text{LC}}} \right)_{\text{b}}$ at long capillary, $\eta_{\text{ENT,a}}$ represents entrance viscosity measured on

the orifice capillary die. Ratio $\left(\frac{L_{\text{C}}}{D_{\text{C}}} \right)_{\text{Tr}}$ has the following form:

$$\left(\frac{L_{\text{C}}}{D_{\text{C}}} \right)_{\text{Tr}} = \frac{1}{2} \left(\frac{\eta_{\text{ENT,a,0}}}{2\eta_0} - \frac{\eta_{\text{ENT,0,e}}}{2\eta_0} \right) \frac{\left(\frac{L_{0\text{C}}}{D_{0\text{C}}} \right)_{\text{a}} - \left(\frac{L_{\text{LC}}}{D_{\text{LC}}} \right)_{\text{b}}}{\left(\frac{L_{\text{LC}}}{D_{\text{LC}}} \right)_{\text{b}}} + \left(\frac{L_{0\text{C}}}{D_{0\text{C}}} \right)_{\text{a}} \quad (65)$$

where $\eta_{\text{ENT,a,0}}$ expresses the entrance viscosity plateau that is measured on an orifice

capillary die with $\left(\frac{L_{0\text{C}}}{D_{0\text{C}}} \right)_{\text{a}}$ ratio, η_0 represents the Newtonian viscosity, and $\eta_{\text{ENT,0,e}}$ is the

entrance viscosity plateau, which is calculated as:

$$\eta_{\text{ENT,0,e}} = 1.6330\eta_0 \quad (\text{Cogswell method}) \quad (66)$$

$$\eta_{\text{ENT,0,e}} = 1.8856\eta_0 \quad (\text{Binding method}) \quad (67)$$

$$\eta_{\text{ENT,0,e}} = 1.1989\eta_0 \quad (\text{Gibson method}) \quad (68)$$

2.6.4 Mooney correction for slip near the wall

As discussed in *Chapter 2.5*, wall slip is a phenomenon which can occur in shear flow. If the wall slip arises in shear viscosity measurements, the results are distorted. For this reason, Mooney [26] derived correction which allows to calculate shear viscosity in wall slip situation.

For deeper Mooney correction analysis it is necessary to go back to *Fig. 30* (slip situation). The velocity of fluid at $r = R_C$ (capillary wall) is equal to v_{SLIP} . The mass flow rate can be mathematically divided into two parts [49]:

$$Q = Q_{SLIP} + Q_{NOSLIP} \quad (69)$$

where Q_{SLIP} is calculated as:

$$Q_{SLIP} = \pi R_C^2 v_{SLIP} \quad (70)$$

and the Q_{NOSLIP} is formulated as:

$$Q_{NOSLIP} = \frac{\pi R_C^2}{4} \dot{\gamma}_{TRUE} \quad (71)$$

where $\dot{\gamma}_{TRUE}$ is the no-slip component of apparent shear rate. When slip occurs, in calculation of apparent shear rate it is necessary to take into account the mass flow rate which comes from slip:

$$\dot{\gamma}_{APP-SC} = \frac{4Q_{NOSLIP}}{\pi R_C^3} - \frac{4Q_{SLIP}}{\pi R_C^3} = \frac{\pi R_C^2}{4} \dot{\gamma}_{TRUE} - \pi R_C^2 v_{SLIP} \quad (72)$$

The corrected value of apparent shear rate may be used in the Weissenberg – Rabinowitsch correction.

2.6.5 Hagenbach (kinetic) correction

Generally, in capillary rheometry, the investigated fluid flows from a large reservoir to a narrow capillary die. Therefore, the cross-section area in the entrance region is substantially changed. As a result of continuity equation (for more details see *Chapter 3.1.1*), the kinetic energy of flow increases because the fluid significantly accelerates. This kinetic energy increment causes the growth of viscosity, because the viscosity is measured as energy consumed to create the flow.

The kinetic correction [50] is derived from the total measured pressure drop (Δp), which consists of two parts. First, pressure drop for the increase of kinetic flow energy (p_K), and second, remaining pressure drop that is used for shear viscosity determination (spent on the flow of the melt through the capillary), $\overline{\Delta p}$. In mathematical formulation [51]:

$$\overline{\Delta p} = \Delta p - p_K \quad (73)$$

The value of p_K is determined as:

$$p_K = \frac{\rho_M \bar{v}^2}{\alpha} = \frac{\rho_M Q^2}{\alpha \pi^2 R_C^4} \quad (74)$$

where ρ_M is melt density, \bar{v} stands for the average value of velocity, and α means the coefficient representing the influence of velocity distribution on the value of kinetic correction. In the case of parabolic velocity profile (Newtonian fluids) $\alpha = 1$. Precise estimation of α value for non-Newtonian fluids is very difficult, but it is also approximately equal to 1.

This correction must be applied in measurements of low-viscosity fluids (e.g. diluted polymer solutions).

2.6.6 Temperature correction

In the derivation of basic relationships in capillary rheometry, the flow of polymer melt is assumed to be isothermal. However, in reality, viscous flow is accompanied by the dissipation of energy (transformation of mechanical energy to thermal energy), which causes the increase of temperature [52], [53]. As a consequence of this, some problems arise. First, the heat generation depends on shear rate. As a result, the heat generation is not uniform along the radius of the barrel and capillary die. Further, part of generated heat is transferred through the barrel into the environment. Therefore, the change of fluid temperature leads to a change in viscosity.

The temperature growth during adiabatic flow of a Newtonian fluid in flow time t is formulated as [51]:

$$\Delta T = \frac{\eta \dot{\gamma}^2 t}{c \rho_M} \quad (75)$$

where ρ_M represents the melt density and c means its heat capacity. The change in viscosity caused by the heat dissipation can be expressed as:

$$\eta_{\bar{T}_0} = \frac{\pi R_c^4 \Delta p}{8 Q L_c} \left(1 + \frac{A Q \Delta p}{16 \pi h_t L_c} \right) \quad (76)$$

Here, h_t stands for the heat transfer coefficient and A is a coefficient of temperature dependence of viscosity, which is determined by the following equation:

$$\eta = \eta_{\bar{T}_0} e^{A(\bar{T} - \bar{T}_0)} \quad (77)$$

where $\eta_{\bar{T}_0}$ expresses viscosity at temperature \bar{T}_0 (set during the test) and \bar{T} is the real temperature (higher than \bar{T}_0 as a result of dissipation), which causes the reduction of viscosity to value η .

The determination of $\eta_{\bar{T}_0}$ and coefficient A is based on the measurement with various values of $\frac{Q \Delta p}{L_c}$. Afterwards, the data are extrapolated to zero value of $\frac{Q \Delta p}{L_c}$, which corresponds to the absence of dissipative contribution.

2.6.7 Pressure correction

In general, polymer melts are considered as incompressible. However, at very high pressures the phenomenon of compressibility can be observed [54]. In these cases, the viscosity is expected to decrease for shear-thinning fluids (e.g. polymer melts). On the contrary to this expectation, in practice the viscosity increases. This anomaly is caused by increase in pressure, which outweighs the viscosity decrease caused by shear rate increase.

The pressure-dependent viscosity is usually formulated as an exponential function [55]:

$$\eta = \eta_{p_0} e^{Bp} \quad (78)$$

where η_{p_0} represents the viscosity at atmospheric pressure and B is a baric (piezo) coefficient of viscosity.

With the aid of Eq. (78), the volumetric flow rate for Newtonian fluids comes to following expression [51]:

$$Q = \frac{\pi R_C^4}{8L_C \eta_{p_0} B} \left(1 - e^{-B\Delta p_{CAP}}\right) \quad (79)$$

At pressure-dependent viscosity measurements the investigated fluid is not extruded to free space (atmospheric pressure) but to a chamber where the pressure can be controlled (generation of back-pressure). This correction must be taken into account in the case of viscosity measurement of polymer melts used in injection moulding.

2.6.8 Pressure losses in the rheometer reservoir

The working region of capillary rheometer is combined from two channels: a large reservoir where from the investigated material enters into a narrow capillary die. In the case of large ratio of these channels, the pressure losses during flow through a reservoir cannot be ignored. In reality, this phenomenon is caused by preferential flow of the measured fluid into the entrance of capillary die, which produces change in the apparent shear viscosity with time.

However, if the control-pressure rheometer mode is employed, the correction need not always be used, because the pressure at the entrance of capillary die, which is required for calculation of viscosity, increases as the reservoir is emptied.

In the case of control-rate rheometer mode, the pressure at the entrance into the capillary die decreases with time. This reduces pressure loss in the reservoir [51].

2.6.9 Adsorption in the channel surface

As introduced above, at the capillary wall a slip can occur. However, in some cases [56] an opposite phenomenon can be observed – *adsorption*. This is particularly observed for dilute polymer solution and a very small capillary radius. This leads to reduction of the effective flow surface area and, as a result, to an increase in apparent shear viscosity.

The adsorption phenomenon must be considered for capillaries with a diameter of up to several tens of microns (e.g. filtration through porous media, or capillary flow of

biological substances). Therefore, in the commonly used capillary rheometers for measurement of polymer melt viscosity, this correction is not considered.

2.7 Limitations of capillary rheometry

As indicated above, capillary rheometry is a universal method for determination of all basic fluid flow quantities. However, the measurement in capillary rheometer has several limitations, which are caused by the following effects [51]:

- *Transition from laminar to turbulent flow conditions*
- *Instability of flow as a result of fluid elasticity*
- *Mechanical and thermal degradation of the measured material*
- *Strong thermal effects at high deformation rates.*

These effects can influence correct shear stress as well as shear rate determination. Thus, the physical limitations for both quantities will be summarized below.

2.7.1 Shear stress

The higher values of shear stress during the measurements are restricted by several factors. First, emersion of flow instability, second, inadequate thermal effects, and third, mechanical and thermal degradation can arise. In general, the upper limit in any cases should not exceed the value of 1 MPa.

On the other hand, the lowest values of shear stress depends mainly on the sensitivity of pressure transducers used during the measurement and influence of parasitic resistance, which appears partially in any design of capillary rheometer (e.g. friction in motion mechanism). In common measurements, the shear stress of approximately 10^{-2} MPa is the ultimate lower limit.

2.7.2 Shear rate

The upper boundary of shear rates in capillary rheometry is approximately 10^6 s⁻¹. However, in common capillary rheometers the tests can be performed in shear rates up to 10^4 s⁻¹. For the tests in the range between 10^4 and 10^6 s⁻¹ it is necessary to use special experimental techniques.

The lower limit of shear rates is given by the following factors. Firstly, measurements with piston movements in order of fractions of a millimetres over a long time requires the use of a high-precision measurement technique, because potential systematic instrument errors cause protraction of measurements. Secondly, long-time measurements under the imposed experimental conditions can induce chemical and structural changes (degradation) in the investigated material. Hence, during the measurements it is difficult to achieve shear rates under approximately 10^{-2} s^{-1} .

Generally, on common capillary rheometers it is possible to determine shear viscosity in the range of $10^{-3} - 10^7 \text{ Pa.s}$.

3 POLYMER MELT FLOW MODELLING

“CALCULI DIFFERENTIALIS EST METHODUS DETERMINANDI RATIONEM INCREMENTORUM EVANESCENTIUM, QUÆ FUNCTIONES QUÆCUNQUE ACCIPIUNT, DUM QUANTITATI VARIABILI, CUIUS FUNT FUNCTIONES, INCREMENTUM EVANESCENS TRIBUTUR.”

(Differential calculus is a method for determining the ratio of the vanishing increments that any functions take on when the variable, of which they are functions, is given a vanishing increment.)

Leonhard Paul Euler (1707 – 1783),

INSTITUTIONES CALCULI DIFFERENTIALIS CUM EIUS USU IN ANALYSI FINITORUM AC DOCTRINA SERIERUM (*Foundations of Differential Calculus with Applications to Finite Analysis and Series*).

Polymer melt flow modelling is useful tool to understand both, unusual flow behaviour of polymer melts during polymer processing as well as complicated link between polymer rheology, machinery design and processing conditions which helps to optimise particular technology process. From the mathematical point of view, it is necessary to solve the conservation equation of mass, momentum and energy together with suitable constitutive equation having capability to describe non-Newtonian and viscoelastic nature of the polymer melts. In the section below, all these equations together with the most popular numerical schemes are introduced in more detail.

3.1 Conservation equations

Conservation equations express mathematically the mass, momentum and energy balances.

3.1.1 Continuity equation

The continuity equation expresses no possibility of mass origin or mass extinction. As can be seen in *Fig. 34*, for the definition of the continuity equation a volume element of fluid $dx dy dz$ is considered. If the fluid density, ρ , as a function varies with all three directions (x, y, z) and time (t) is established, we obtain [57]:

$$\left\{ \begin{array}{l} \text{Stored mass} \\ \text{per unit time} \end{array} \right\} = \left\{ \begin{array}{l} \text{Entering mass} \\ \text{per unit time} \end{array} \right\} - \left\{ \begin{array}{l} \text{Leaving mass} \\ \text{per unit time} \end{array} \right\} \quad (80)$$

In vector symbolism, Eq. (80) changes into:

$$\frac{\partial \rho}{\partial t} = -(\nabla \rho \vec{v}) \quad (81)$$

where \vec{v} is the velocity vector which contains velocity components v_x , v_y , and v_z . Eq. (81) expresses the change of density with time at a fixed reference point as a function of mass flow vector $\rho \vec{v}$.

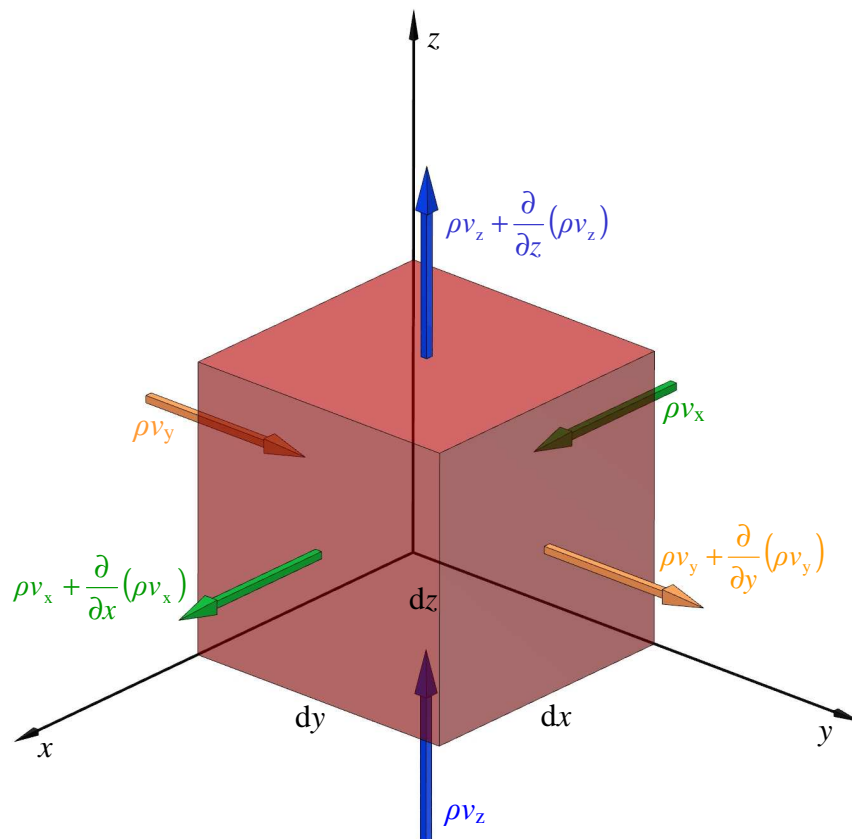


Fig. 34: Volume element of fluid

3.1.2 Momentum equation

Momentum equation represents acceleration of a differential mass element moving with a flow because of the forces acting on it. As illustrated in Fig. 35, three types of forces affect the volume fluid element. Namely, pressure forces, surface forces and gravitational forces must be taken into account.

Afterwards, the momentum equation written in words has the following form [57]:

$$\left\{ \begin{array}{l} \text{Change in the} \\ \text{momentum} \\ \text{per unit time} \end{array} \right\} = \left\{ \begin{array}{l} \text{Entering} \\ \text{momentum} \\ \text{per unit time} \end{array} \right\} - \left\{ \begin{array}{l} \text{Leaving} \\ \text{momentum} \\ \text{per unit time} \end{array} \right\} + \left\{ \begin{array}{l} \text{Forces acting} \\ \text{on the system} \end{array} \right\} \quad (82)$$

With the aid of vector and tensor symbolism Eq. (82) is rewritten to:

$$\frac{\partial}{\partial t} \rho \vec{v} = -(\nabla \rho \cdot \vec{v} \cdot \vec{v}) - \nabla p - \nabla \tau + \rho \vec{g} \quad (83)$$

where term $\frac{\partial}{\partial t} \rho \vec{v}$ expresses momentum change per unit time $(\nabla \rho \cdot \vec{v} \cdot \vec{v})$ represents change in the motion (momentum flux) per unit time and ∇p stands for pressure forces acting on the considered element, $\nabla \tau$ symbolizes surface forces change per unit time, $\rho \vec{g}$ means gravitational force acting on the considered element, all the considered terms are per unit volume.

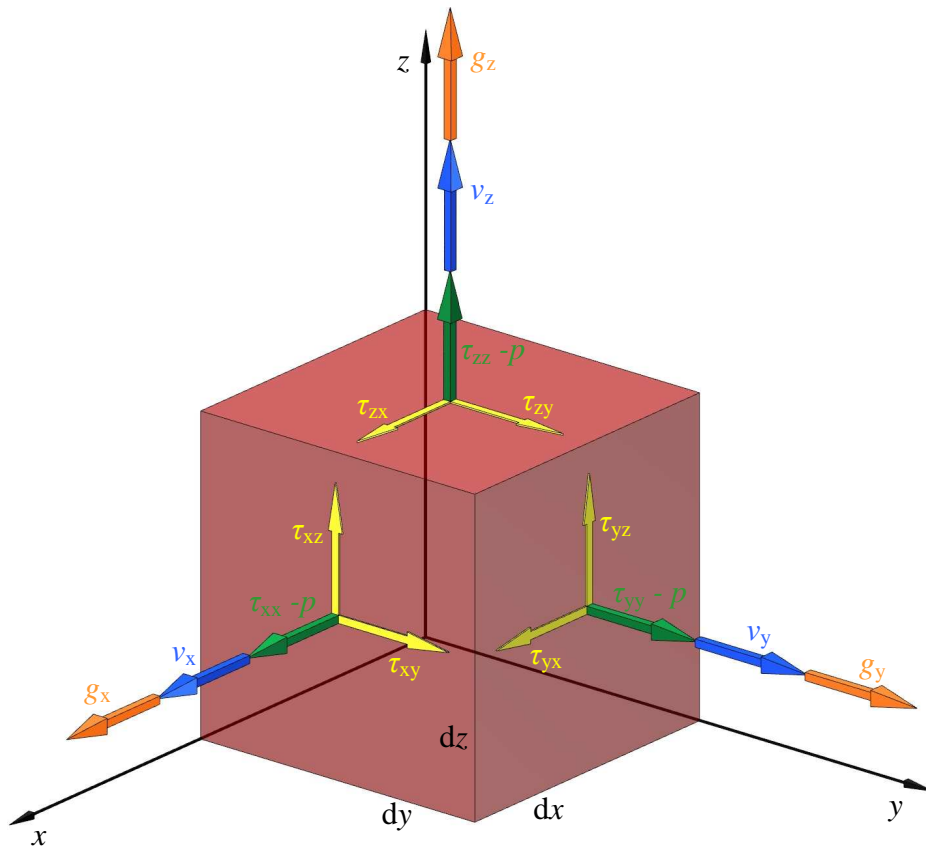


Fig. 35: Components of stress, velocity and gravitational acceleration acting on differential volume of fluid

3.1.3 Energy equation

In nature, energy can neither originate nor to fade, but it can only change the form. Therefore, the energy equation is derived from balance of energy into an elementary volume in a given time (per unit time) [57]:

$$\begin{aligned} & \left\{ \begin{array}{l} \text{Change in internal} \\ \text{and kinetic energy} \end{array} \right\} = \left\{ \begin{array}{l} \text{Increase in internal} \\ \text{and kinetic energy} \end{array} \right\} - \left\{ \begin{array}{l} \text{Decrease in internal} \\ \text{and kinetic energy} \\ \text{through convection} \end{array} \right\} + \\ & + \left\{ \begin{array}{l} \text{Change in internal} \\ \text{energy through} \\ \text{conduction} \end{array} \right\} - \left\{ \begin{array}{l} \text{Work which the} \\ \text{system carries out on} \\ \text{the environment} \end{array} \right\} + \left\{ \begin{array}{l} \text{Change in internal} \\ \text{energy due to heat} \\ \text{sources} \end{array} \right\} \quad (84) \end{aligned}$$

In mathematical notation the energy equation has the following form:

$$\frac{\partial}{\partial t} \rho \left(U + \frac{1}{2} v^2 \right) = - \left[\nabla \rho \vec{v} \left(U + \frac{1}{2} v^2 \right) \right] - \nabla \vec{q} + \rho (\vec{v} \cdot \vec{g}) - p \vec{v} - \nabla [\tau \cdot \vec{v}] + \phi \quad (85)$$

where the term $\frac{\partial}{\partial t} \rho \left(U + \frac{1}{2} v^2 \right)$ expresses change in energy, $\left[\nabla \rho \vec{v} \left(U + \frac{1}{2} v^2 \right) \right]$ represents change in energy through convection, $\nabla \vec{q}$ means change in energy due to heat conduction, $\rho (\vec{v} \cdot \vec{g})$ stands for work due to gravitational forces, $p \vec{v}$ symbolizes work due to pressure forces, $\nabla [\tau \cdot \vec{v}]$ signifies work due to viscous forces, all the considered terms are per unit time and volume. Finally, ϕ is change in internal energy due to heat sources.

3.2 Constitutive equations for polymer melts

Constitutive equations represent the molecular stresses generated in the flow due to kinetic variables, such as velocities, strains, and derivates of velocities and strains. In each of these equations many assumptions and idealizations of produced stress and molecular or structural forces are included.

According to the mathematical form two groups of constitutive equations (CE) are recognized. Firstly, in differential CEs the actual stress is computed from particular set of differential equations. This group contains a number of constitutive models (e.g. Leonov model [58], PTT model [11], XPP model [12] etc.). Secondly, integral CEs give the stress tensor as the integral of all stress contributions from the remote past ($t = -\infty$) to the present

time (t). The most general integral constitutive equation is K-BKZ model [59], [60] and many derived integral CEs can be found in open literature [61]. In order to calculate the stress for a particle at a specific location, the differential models give the present stress without flow history requirements, whereas in the case of integral CEs, integrating over the whole flow history of particle is necessary. For a particular purpose there are a number of models [61].

In this work modified White-Metzner model [62], whose main advantage consists in analytical form of equations for description of shear and extensional viscosities, will be used. For this reason, the model parameters identification from the experimental data is direct and simple by using last square minimization method, which is not possible when more sophisticated constitutive equations are employed.

3.2.1 Modified White-Metzner model

In generalization of Maxwell model proposed by White, Metzner and Barnes [62], the viscosity and relaxation time are allowed to vary with second invariant of strain – rate tensor. Mathematically

$$\underline{\underline{\tau}}_{ij} + \bar{\lambda}(II_D) \overset{\nabla}{\underline{\underline{\tau}}} = \eta(II_D) \underline{\underline{D}}_{ij} \quad (86)$$

where $\underline{\underline{\tau}}_{ij}$ and $\underline{\underline{D}}_{ij}$ is given by the Eqs. (1) and (2) respectively, $\bar{\lambda}(II_D)$ represents the deformation rate – dependent relaxation time, $\overset{\nabla}{\underline{\underline{\tau}}}$ expresses upper convected stress tensor derivate, and $\eta(II_D)$ stands for the deformation rate – dependent viscosity. Term $\eta(II_D)$ in Eg. (86) is the Carreau-Yasuda function:

$$\eta(T, II_D) = \frac{\eta_0 a_t}{\left[1 + \left(\lambda a_t \sqrt{2II_D}\right)^\alpha\right]^{\left(\frac{1-\bar{n}}{\alpha}\right)}} \quad (87)$$

Here, a_t is exponential equation for temperature – dependent shift factor:

$$a_t = \exp[-A(T - T_0)] \quad (88)$$

or Arrhenius equation for temperature – dependent shift factor:

$$a_t = \exp\left[\frac{E_A}{R_G}\left(\frac{1}{273.15 + T} - \frac{1}{273.15 + T_0}\right)\right] \quad (89)$$

where E_A expresses activation energy, R_G is the universal gas constant, A stands for temperature sensitivity, T_0 represents reference temperature, and η_0 , λ , a , \bar{n} are adjustable parameters. Furthermore, the uniaxial extensional viscosity is determined according following relationship:

$$\eta_E = \frac{2\eta(T, II_D)}{1 - \frac{2}{\sqrt{3}}\lambda(T, II_D)II_D} + \frac{\eta(T, II_D)}{1 + \frac{1}{\sqrt{3}}\lambda(T, II_D)II_D} \quad (90)$$

As also shown by Barnes and Roberts [62], with the aid of specific functions of $\eta(T, II_D)$ and $\bar{\lambda}(T, II_D)$ (Eqs. (86), (87), (88) or (89) and (90)) the model can be used for very good description of elongational viscosity of real polymer melts, because it does not predict infinite elongational viscosity:

$$\bar{\lambda}(T, II_D) = \frac{\lambda_0 a_t}{1 + K_1 a_t II_D} \quad (91)$$

where λ_0 , K_1 are constants defined by the following constrain: $\frac{\lambda_0}{K_1} < \frac{\sqrt{3}}{2}$ [62].

The modified White-Metzner model is represented in Eqs. (86), (87), (90) and (91) together with the physical limitation for λ_0 and K_1 . The modified White-Metzner model can be applied only in steady flows because in this model the relaxation time depends on II_D .

As can be seen in *Fig. 36*, the agreement between shear and uniaxial extensional viscosity obtained experimentally for various polymeric materials (unfilled polymers, polymers filled with glass beads, polymer blends) and through the modified White-Metzner model is very good.

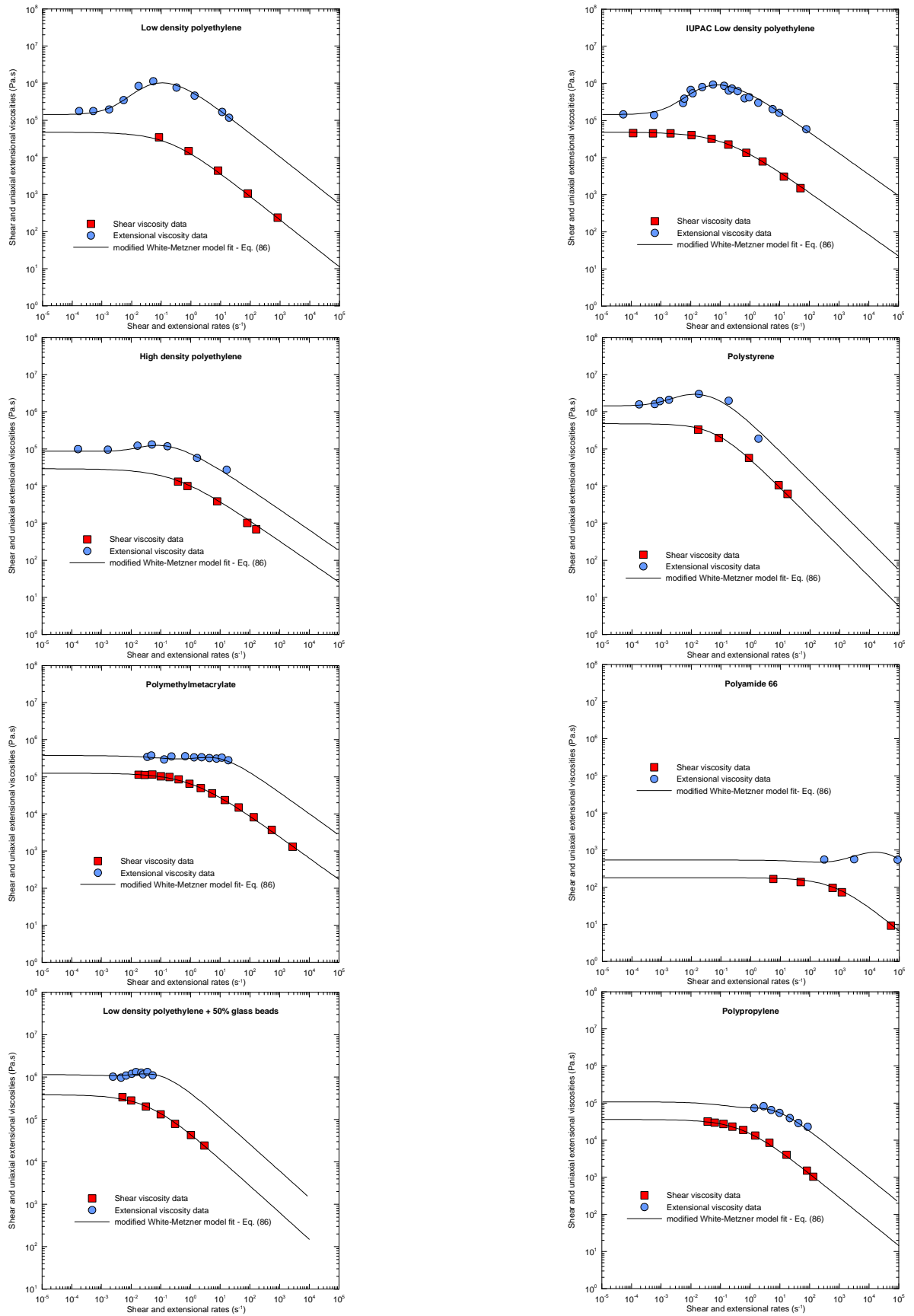


Fig. 36: Comparison of shear and extensional viscosity obtained experimentally (symbols) and through modified White – Metzner model (lines) (taken from [62])

3.3 Computer aided analysis and design

As introduced earlier, during all types of polymer processing a lot of instabilities can be observed (see *Chapter 1.2*). In order to eliminate these instabilities, expensive and time-consuming trial-and-error procedures were previously used without knowledge of physical and chemical basis of these phenomena. Nowadays, mathematical description of basic material properties (e.g. shear and extensional viscosity, first and second normal stress differences) and progress in computational technique allow using numerical modelling in order to predict these instabilities.

Mathematical modelling is based on the solution of mathematical equations which describe physical (and/or chemical) interactions in the given process. It should be kept in mind that an exact solution of viscoelastic flow problems is not possible due to non-linear nature of conservation and constitutive equations. All of these equations together create a system of partial differential equations that are very difficult to solve by common mathematical tools. However, sufficiently accurate results can be obtained by numerical methods.

In numerical solution some important steps have to be performed. Firstly, the flow domain is discretized to small elements which create a grid. The shape and type of grid depends on the flow domain shape and numerical method choice. Generally, the grid density is an independent parameter and at higher grid density (smaller elements) the obtained results are more exact; on the other hand, the computing time is larger. Second, the differential conservation and constitutive equations are applied in all grid nodes, hence, the complicated differential equations are reduced only to simple algebraic equations. Finally, the primary variables (velocities, pressure, temperature) as well as other important quantities (local stresses, shear rates, streamlines etc.) are computed from a large number of algebraic equations.

As mentioned above, polymer melt flow problems are non-linear, therefore iterative solutions are necessary to use until acceptably small tolerance convergence is reached. An iterative process means a series of steps, where the first step is a solution with basic input values (set by the user) and the other steps have input values from the previous solution. If the solution from the previous step and the last step are in desirable tolerance, the last solution is the final solution of the given problem. Two basic situations can

arise: *convergence* or *divergence process*. In convergence process the solutions are approaching, which leads to a right solution. On the other hand, in divergence process the solutions recede and the solution will not be found. It should be noted that all numerical methods are not absolutely accurate and the precision of each of the methods is dependent mainly on the grid density.

Three basic numerical methods are usually employed: *Flow analysis network (FAN)*, *Finite differences method (FDM)* and *Finite elements method (FEM)*.

3.3.1 Flow Analysis Network (FAN)

The Flow Analysis Network (FAN), usually called the Control Volume Method (CVM), employs physical principles for solution of differential equations. In this method it is not necessary to use discretization of the flow domain but only simplification of a complex shape of flow domain to basic geometrical shapes is required. In this method the pressure drop (Δp) and mass flow rate (Q) through channels are in relation [63]:

$$\Delta p = \text{const} Q^{\bar{n}} \quad (92)$$

At the beginning of computing, the flow domain is divided into elementary subregions (e.g. tubes, rectangles), where Eq. (92) is approximately valid. Subsequently, the flow relations applied in each subregion are step-by-step affixed in computer program, which includes algebraic equations with local pressure (p) and local mass flow rate (Q) as unknowns. The other secondary variables from the solution can be determined. As already said, for the case of polymer melts the iterative procedure is necessary to use. *Fig. 37* depicts a typical flow problem solvable by the FAN method, which is flow of polymer melt in a spiral mandrel die used in film blowing process.

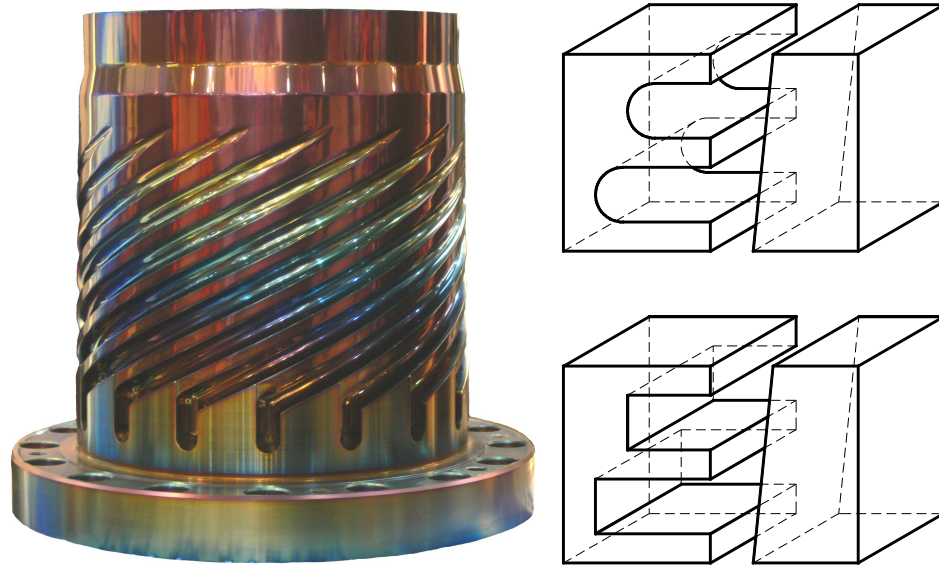


Fig. 37: Typical spiral mandrel die geometry (real die on the left side, real model of channels on the top of the right side and FAN grid of channels below it)

3.3.2 Finite Difference Method (FDM)

The finite difference method is based on the creation of suitable FD grid (as can be seen in *Fig. 38*) and subsequently, the replacement of derivatives by difference approximations at each point of FD grid. This method is mainly used to solve heat conduction problems.

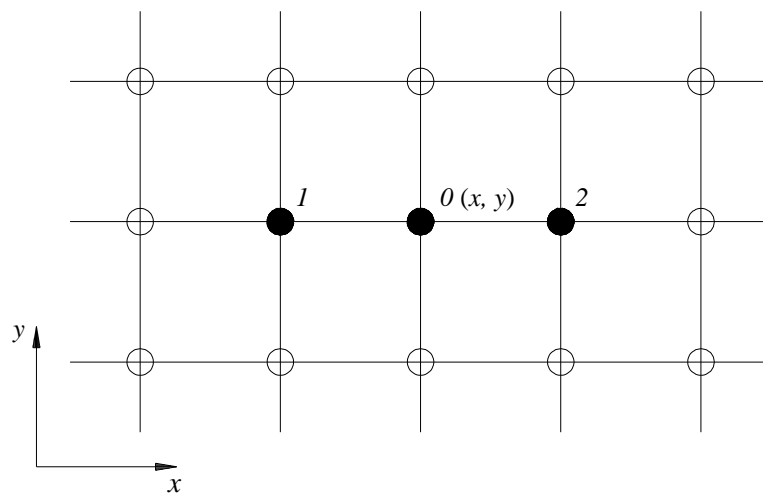


Fig. 38: Typical Finite difference grid

The computational procedure is, for example at point 0 (x,y), following: The first derivative for velocity can be approximated as [63]:

$$\frac{dv}{dx} = \frac{v_2 - v_1}{2\Delta x} \quad (93)$$

and the second derivative as:

$$\frac{d^2v}{dx^2} = \frac{v_2 - 2v_0 + v_1}{(\Delta x)^2} \quad (94)$$

Another step is substitution of each differential equation by difference approximations at each nodal point of the FD grid. As a result, a system of algebraic equations is obtained, which are then solved by a relevant technique. For the solution of 3D problems including mass, momentum, heat transfer and chemical reactions, one version of this method, known as Finite Volume (FV), is often used.

3.3.3 Finite Element Method (FEM)

In finite element method (FEM) the solution of equations is approximately searched by simple polynomials (e.g. linear for pressure and quadratic for velocity) for each element of an FEM grid using variational principles. In order to determinate the unknown variables, algebraic solution of a very large number of equations is necessary to do. A flat spiral die used in film blowing process is a typical viscoelastic flow problem in which the FEM method is suitable to use.

Fig. 39 shows a real flat spiral die (on the left side) and the FEM grid of distribution system of this die (on the right side) as example.

Two essential conditions of *Finite element method* as well as the *Finite difference method* are necessary to control during the computation. First, stability condition includes boundless growth or controlled decay of errors associated with the solution of the algebraic equations. Second, convergence condition represents the approach to successful numerical solution. Mathematically this successfulness is expressed as a decrease of the step sizes (Δx , Δy , Δz) down to zero. In the case of viscoelastic simulations it is necessary to use special solution techniques because these simulations are prone to loss of stability or divergence. Frequently, the solution of these problems is carried out with the aid of two

(or more) significantly different grid densities. Afterwards, the results obtained from different grid densities should have very small differences.

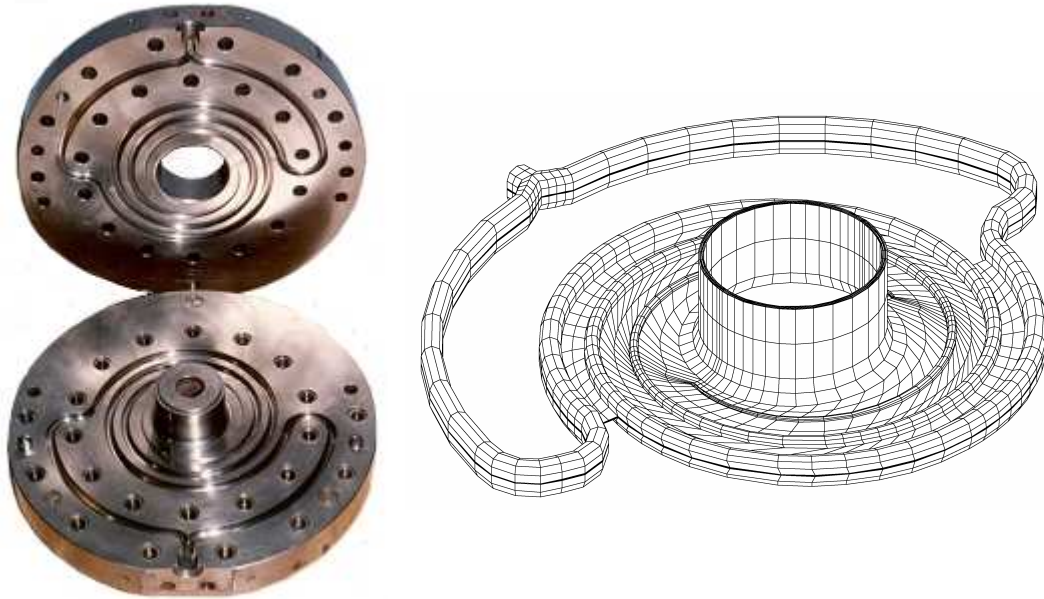


Fig. 39: Typical flat spiral die geometry (real die-left, and FEM grid of distribution system-right) (taken from [64])

Analytical methods and various numerical methods differ in the amount of computation required, as well as in accuracy and applicability of the results. The FE method allows solving more geometrically complex flow domains than FD and FAN methods. However, the realization of FEM solution is more difficult than of the others. The main advantages of FAN method, on the other hand, are easier implementation than FD or FE methods and better convergence procedure, even in the case of rough grids. Nevertheless, the FAN method is not able to give precision results on local flow details.

As result of above mention discussion, the FEM has been chosen for theoretical analysis in this work.

4 AIMS OF THE WORK

“MAGISTER ARTIS INGENIQUÉ LARGITOR VENTER.”

(Necessity is the mother of all invention.)

Aulus Persius Flaccus (A.D. 34 – 62),

SATURAE (*The Satires*).

The main aim of this work is to theoretically and experimentally evaluate different techniques for extensional viscosity determination from the entrance pressure drop measurements by using orifice die with respect to highly branched, slightly branched and linear polymer melts. Special attention will be paid to the development and testing of the novel orifice die design as well as to novel calibration procedure which will leads to very precise entrance pressure drop measurements even at pressure transducer down resolution limit.

II. EXPERIMENTAL

5 MATERIALS

“NAMQUE MOVETUR AQUA ET TANTILLO MOMINE FLUTAT QUIPPE VOLUBILIBUS PARVISQUE CREATA FIGURIS. AT CONTRA MELLIS CONSTANTIOR EST NATURA ET PIGRI LATICES MAGIS ET CUNCTANTIOR ACTUS; HÆRET ENIM INTER SE MAGIS OMNIS MATERIAI COPIA, NIMIRUM QUIA NON TAM LEVIBUS EXTAT CORPORIBUS NEQUE TAM SUPTILIBUS ATQUE RUTUNDIS.”

(For water is moved, and flows, with so trifling a force acts upon it, inasmuch as it is composed of voluble and small particles. But the nature of honey, on the other hand, is more dense, and its fluid sluggish, and its movement more tardy; for whole mass of material particles clings more closely together; because, as is evident, it consist of bodies neither so smooth, nor so small and round.)

Titus Lucretius Carus (ca. 99 – ca. 55B.C.),
DE RERUM NATURA (*On the Nature of Things*).

In this work, the following materials have been used:

- **LDPE, Escorene LD 165 BW1 (Exxon, USA):**

$$\rho_s = 0.922 \text{ g.cm}^{-3}, M_w = 366,300 \text{ g.mol}^{-1}, M_n = 30,280 \text{ g.mol}^{-1}$$

- **LDPE, Lupolen 1840H (Basell, Germany):**

$$\rho_s = 0.919 \text{ g.cm}^{-3}, M_w = 258,000 \text{ g.mol}^{-1}, M_n = 15,542 \text{ g.mol}^{-1}$$

- **mLLDPE, Exact 0201 (Exxon, USA):**

$$\rho_s = 0.902 \text{ g.cm}^{-3}, M_w = 88,700 \text{ g.mol}^{-1}, M_n = 41,449 \text{ g.mol}^{-1}$$

- **HDPE, Tipelin FS 450 – 26 (TVK, Hungary):**

$$\rho_s = 0.945 \text{ g.cm}^{-3}, M_w = 212,300 \text{ g.mol}^{-1}, M_n = 22,430 \text{ g.mol}^{-1}$$

6 EQUIPMENT AND METHODS

“ILLUD INSUPER PRÆCIPIMUS, UT OMNIA IN NATURALIBUS TAM CORPORIBUS QUAM VIRTUTIBUS, QUANTUM FIERI POTEST, NUMERATA, APPENSA, DIMENSA, DETERMINATA PROPONATUR. OPERA ENIM MEDITAMUR, NON SPECULATIONES. PHYSICA AUTEM ET MATHEMATICA BENE COMMISTÆ GENERANT PRACTICAM.”

(We moreover recommend that all natural bodies and qualities be, as far as possible, reduced to number, weight, measure, and precise definition. For we are planning actual results and not mere theory. And it is a proper combination of physics and mathematics that generates practice.)

Francis Bacon (1561 – 1626),

PARASCEVE AD HISTORIAM NATURALEM ET EXPERIMENTALEM (*A Preparation for a Natural and Experimental History*).

In this section, all experimental devices used in consequent experimental work are introduced in more detail. Specific attention is paid here to the calibration procedure utilized for the orifice die pressure transducer to take possible nonlinearities occurring in their down resolution limit properly into account.

6.1 Capillary rheometer ROSAND RH7-2

The *RH7-2* (*ROSAND Precision*, Ltd., England) is advanced floor standing controlled-rate capillary rheometer which can be used to determinate the rheological properties of thermoplastic materials at a wide range of deformation rates and temperatures. As can be seen in *Figs. 19* (transparent section view of barrel section) and *40* (real view of complete device) this rheometer is designed in twin-bore technology which allows to perform two simultaneous measurements by using two different capillaries. This allows determining Bagley and Rabinowitsch corrected shear viscosity during one test.



Detail of pistons and entry area into barrel

Detail of heated barrel with three heated belts and two pressure transducers

Fig. 40: Real view of twin-bore capillary rheometer ROSAND RH7-2

The rheometer essentially consists of the drive sub-system (motor, gear box, lead screw and crosshead), the barrel assembly, which is attached to the drive system by the tie rods, and a frame on which the drive system is mounted. Via the drive sub – system is realized the piston movement (the pistons are mounted at the bottom of the crosshead) and the piston position is controlled through closed loop system, with an optical shaft encoder feeding back to the motor drive board. Required temperature is reached by the three ceramic heaters which create three separate zones. Each of this zone has independent regulation that is pursued through platinum resistance thermometers and three term (PID) control algorithm. As a final measurement units are two pressure transducers which are located in entry die regions and they contain resistive bridge strain gauges. These transducers work in analogue mode and in order to pressure data processing the analogue/digital conversion must be used. Furthermore, all above mentioned controls and analysis of measured data are carried by *Rosand Flowmaster™ 2000* software.

The measurements were carried out in a constant piston speed mode at the shear rate of $(0.04 - 3000) \text{ s}^{-1}$. For measure of pressure drops in high deformation rates we used pressure transducers (Dynisco, USA) in ranges of (10,000) PSI (68.9476 MPa), and (1,500) PSI (10.3421 MPa). In order to obtain the most accurate rheological data at low deformation rate range, two high sensitive pressure transducers (500) PSI (3.4473 MPa) and (250) PSI (1.7237 MPa) calibrated with specific care (see *Chapter 6.2* for pressure calibration details) were used to determine entrance pressure drop.

Three sets of capillaries were used for the measurements. Their dimensions were following:

- orifice capillary die: $L_{OC} = 0,125 \text{ mm}$, $D_{OC} = 1 \text{ mm}$
 $L_{OC} = 0,250 \text{ mm}$, $D_{OC} = 2 \text{ mm}$
 $L_{OC} = 0,375 \text{ mm}$, $D_{OC} = 3 \text{ mm}$

- long capillary die: $L_{LC} = 16 \text{ mm}$, $D_{LC} = 1 \text{ mm}$
 $L_{LC} = 32 \text{ mm}$, $D_{LC} = 2 \text{ mm}$
 $L_{LC} = 27 \text{ mm}$, $D_{LC} = 3 \text{ mm}$

The scheme of conventional orifice die is depicted in *Fig. 41*. The diameter of barrel was $D_B = 15 \text{ mm}$.

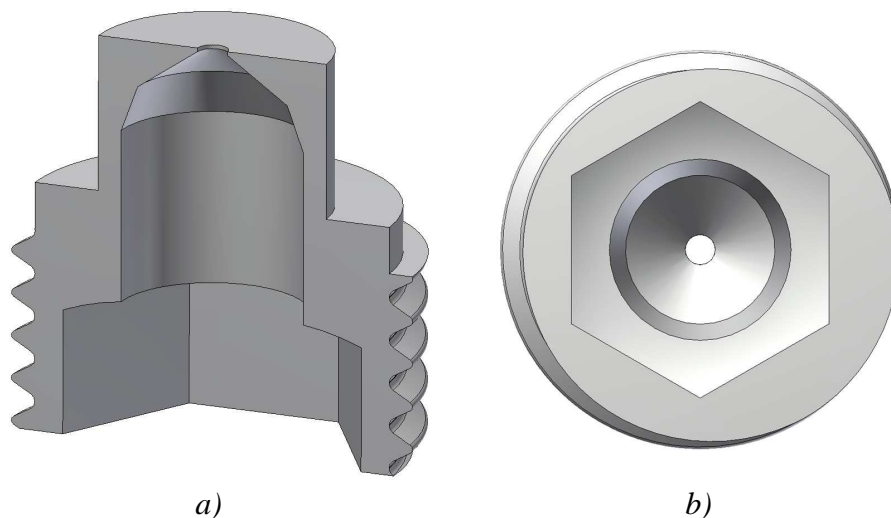


Fig. 41: Conventional orifice die – section view (a), bottom view (b)

The rheological tests of investigated polymer materials were performed at temperatures 150°C, 200°C and 250°C for highly branched *LDPE Lupolen 1840H*, 180°C for slightly branched *mLLDPE Exact 0201* and linear *HDPE Tipelin FS 450 – 26*. Before each of test *auto-gain calibration* of pressure transducers was performed and the polymer granules was perfectly compacted to eliminate air bubbles. As additional, two preheating steps (for 3 and 6 minutes) as well as two compression steps (to 0.5 MPa) were utilized.

6.2 Pressure transducer calibration

As introduced in *Chapter 2*, all rheological quantities which are measured on twin – bore controlled-rate capillary rheometer are determined only through the knowledge of barrel/die geometry, piston speed and measured pressure drop at particular capillary. Since the values of entrance pressure drop are very low (especially in low deformation rates) specific care has to be done with respect to pressure transducer calibration, especially at down resolution limit region. The principle of pressure calibration is based on an application of known pressure (by using pressure source) on the calibrated transducer with consequent detection of its response. The pressure is either applied by a *dead-weight system* (using calibrated weights to produce a known pressure), or by applying the pressure through the *fluid medium* (oil or compressed air). Calibration curve is determined from reference pressure and pressure transducer response.

The *ROSAND RH7-2* software (*Rosand Flowmaster™ 2000*) allows a *single – point* or *multi - point* calibration, which are discussed bellow in more details.

6.2.1 Single - point calibration

The *single - point calibration* is in fact a two-point calibration. The principle of this type of calibration consist in zeroing the pressure transducer output at zero pressure (first point) with consequent application of particular pressure from the pressure source which usually represents 80% from the full transducer scale (second point). These two points create a straight line – *calibration curve* (its slope is usually called a “*gain*”) according to which the pressure transducer output is corrected. The main disadvantage of this single point calibration is assumption of linear extrapolation between these two calibration points which do not take pressure transducer nonlinearities properly into account. Therefore, the measurements at down pressure transducer resolution limit can be highly erroneous.

6.2.2 Multi - point calibration

In this case, the *calibration curve* obtained from *single-point calibration* is followed by number of additional calibration points covering the whole pressure transducer range and the possible nonlinearities are expressed as percentage deviation (correction) from the linear calibration curve. This correction is defined as following:

$$correction = \frac{100(p_{REF} - p_{TRANS})}{P_{TRANS}} \quad (95)$$

where p_{REF} represents the reference pressure from calibration device and p_{TRANS} is pressure transducer response.

In this work, the calibration has been performed in the following way. First, the certain pressure value was generated by the calibration device and corresponding pressure transducer response has been recorded. After that, the compressed air from the calibration device was emptied to achieve zero pressure. The correction factor was calculated for this particular case only if the pressure transducer indicated the zero pressure value. If the indicated pressure was non-zero, *auto-gain calibration* was performed and the procedure has been repeated again until the zero pressure was achieved on pressure transducer for zero pressure conditions. The procedure has been repeated for all chosen calibration points. Obtained calibration curve was used to calibrate the particular pressure transducer with consequent three times check. This step by step methodology eliminates possible errors which can arise from residual currents in rheometer electrical systems. In this work, the 500 PSI pressure transducer has been calibrated by using 39 calibration points whereas for highly sensitive 250 PSI pressure transducer 69 calibration points were used. As a final step following after the calibration of each pressure transducer three times repeated control was performed.

6.2.3 Pressure calibration device

In this work, compressed air based calibration device CCS 20 from *AMV Messgeräte GMBH* has been utilized. As can be seen in *Fig. 42* the air pressure is generated by calibration hand pump. Afterwards, the pressure is roughly regulated by emptying valve or more precisely controlled by the fine pressure regulation. Furthermore, the calibration hand pump has two pressure outputs. First one is connected to the pressure

transducer through transition part whereas the second one is attached to the pressure indicator through air hose. In order to determine calibration curve very precisely, two pressure indicators with various ranges (0 – 20 kPa and 0 – 2000 kPa) were used.

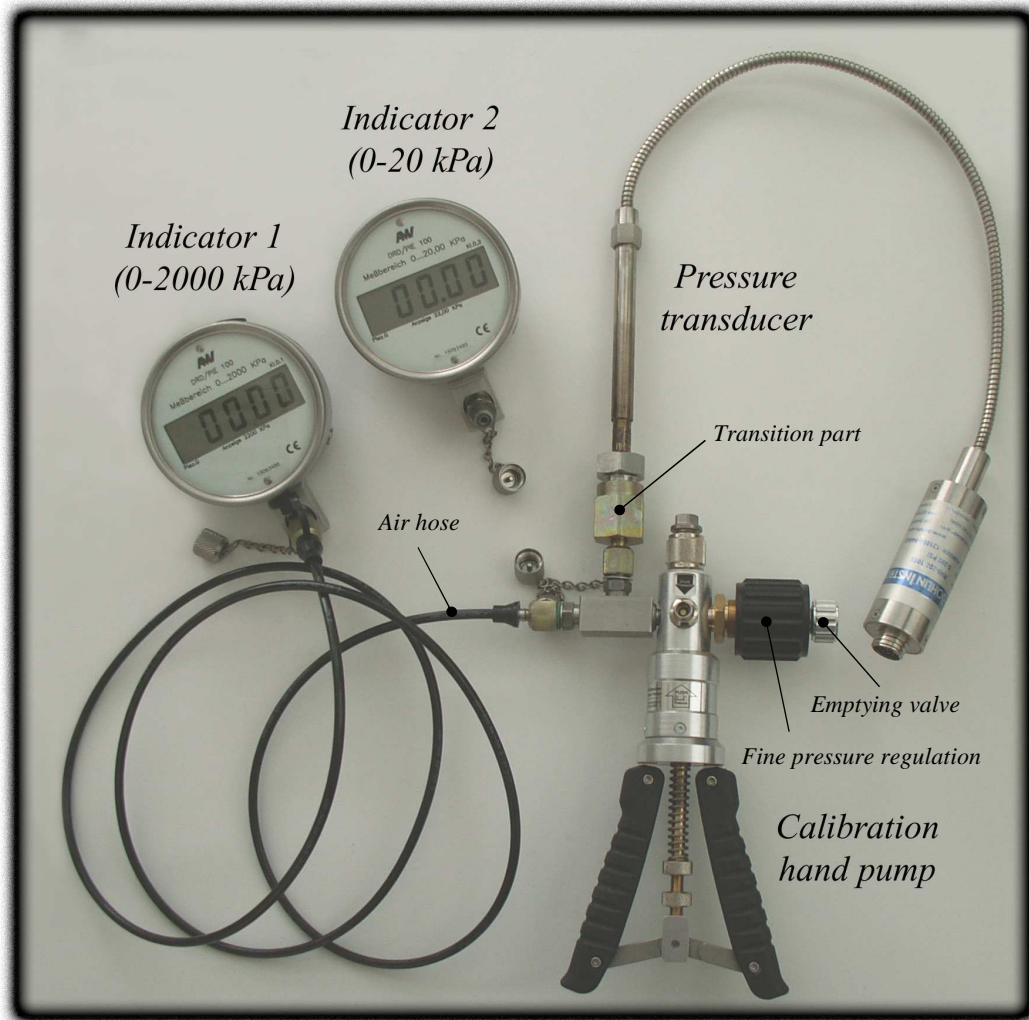


Fig. 42: Real view of calibration device in operation state

6.3 SER-HV-A01 Universal Testing Platform

Sentmanat Extensional Rheometer (SER) Universal Testing Platform is a novel type of extensional rheometer, which was developed by M. L. Sentmanat [15]. It is designed as a detachable fixture for commercially available rotational rheometers and it allows measuring not only uniaxial extensional rheology of polymer melts and elastomers but it also possible to perform another tests: T – peel/adhesion, friction, tear and tensile [10].

As can be seen in *Fig. 43* Sentmanat extensional rheometer consists of two (master and slave) wind-up drums mounted on bearings, housed in a chassis, and mechanically connected through intermeshing gears. As a result of drive shaft rotation both drums are revolved with same speed but opposite orientation (intermeshing gears have gear ratio 1:1). Polymer sample is placed between drums and securing clamps (one is on the master drum, the other on the slave drum) and with the rotation of both drums the sample is stretched above the unsupported length, L_0 (centreline distance between the master and slave drums). The resistance of sample is representing as a tangential force rise up on both drums. This force causes torque T_q , which is measured by torque transducer on the torque shaft. This figure also shows the behaviour of the sample during the test. The sample length increases while the sample width decreases exponentially. The main advantage of this device consists in only few milligrams of tested material need and further this platform can be used for molten or solid materials characterization over a very wide range of temperatures and kinematics deformation rates.

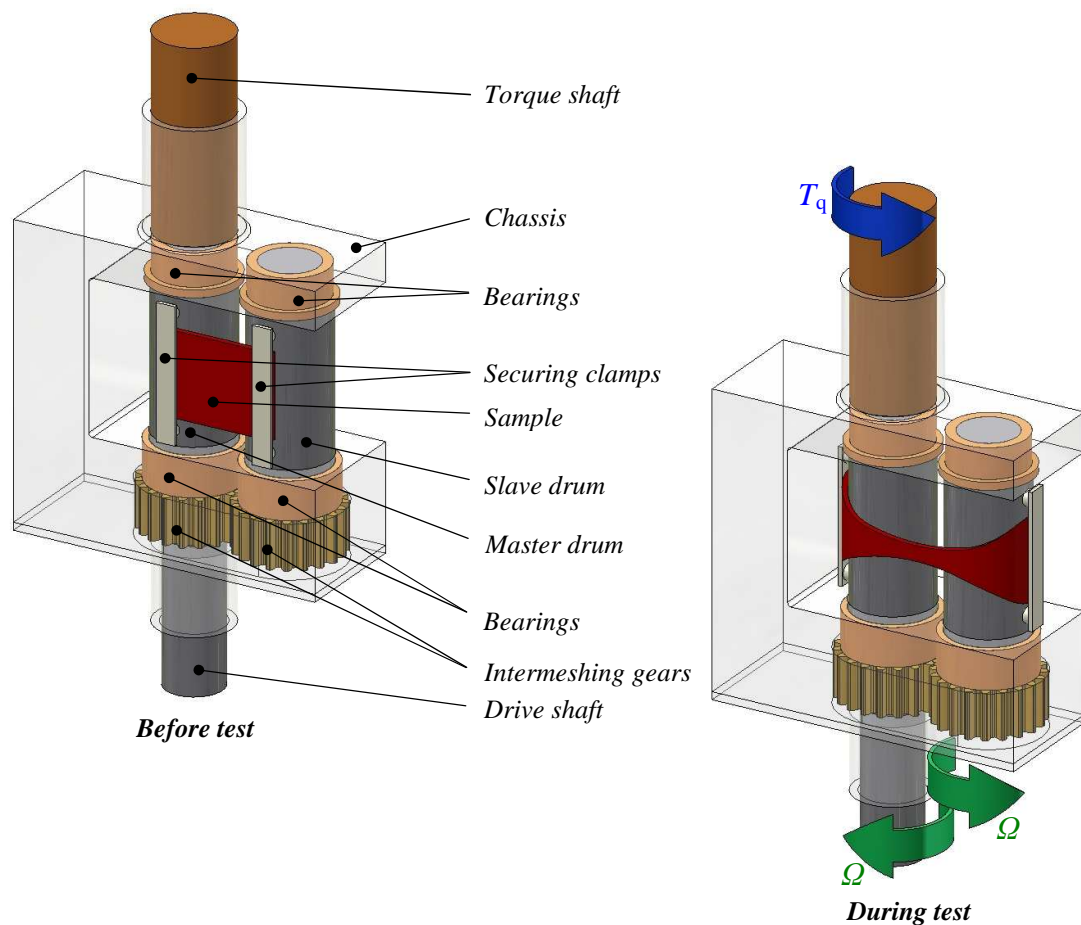


Fig. 43: Schematic view of Sentmanat extensional rheometer (SER)

6.4 Compuplast® Virtual Extrusion Laboratory™ (VEL)

Finite Element Method based analysis has been performed by using Virtual Extrusion Laboratory™ (version 6.2) software from Compuplast®, International company.

RESULTS AND DISCUSSION

“OMNE IGNOTUM PRO MAGNIFICO EST.”

(We have great notions of everything unknown.)

Publius (or Gaius) Cornelius Tacitus (A.D. ca. 55 – ca. 116),

DE VITA ET MORIBUS IULII AGRICOLAE (The Life and Character of Julius Agricola).

FEM analysis of Binding, Cogswell and Gibson models

In this part, the capability of Binding, Cogswell and Gibson models to determine extensional rheology for different polymer melts has been investigated theoretically by the modelling of the abrupt contraction flow through “*ideal orifice die*” by FEM. For this aim, *LDPE Escorene LD 165BW1* [65] together with four additional *virtual materials* having continuously decreasing extensional strain hardening level were considered (see *Figs. 51,52*). This has been done by holding parameters in Eq. (87) as a constant, whereas λ_0 and K_1 parameters in Eq. (91) were varied. The modified White-Metzner model parameters for all these samples are provided in *Tab. 5*.

Tab. 5: Parameters of modified White-Metzner model (Eqs. (86), (87) and (91)) for both, real (LDPE Escorene LD 165 BW1) and virtual (M1, M2, M3 and M4) materials

Function	modified White-Metzner model					
Material	η_0 (Pa.s)	λ (s)	a (-)	\bar{n} (-)	λ_0 (s)	K_1 (-)
LDPE Escorene LD 165BW 1	77,103	7.6286	0.4747	0.3284	248.32	293.63
Virtual material M1	77,103	7.6286	0.4747	0.3284	236.00	293.63
Virtual material M2	77,103	7.6286	0.4747	0.3284	220.00	293.63
Virtual material M3	77,103	7.6286	0.4747	0.3284	193.00	293.63
Virtual material M4	77,103	7.6286	0.4747	0.3284	0.00	293.63

The sketch of the “*ideal orifice die*” (i.e. it is assumed that the downstream region of the orifice is not filled by the melt – the extrudate flows as a free jet through the expansion) together with corresponding boundary conditions and FE mesh is provided in *Fig. 44*. The die has 90° entrance angle, 2 mm die diameter and capillary length equal to 0.24 mm (ideally this length should be zero but from machinery point of view the considered orifice die has certain very small length). According to [66], the maximum

achievable extensional strain in this domain is given by Eq. (96) i.e. 4.03 in this specific case.

$$\varepsilon = 2 \ln \frac{R_B}{R_{OC}} \quad (96)$$

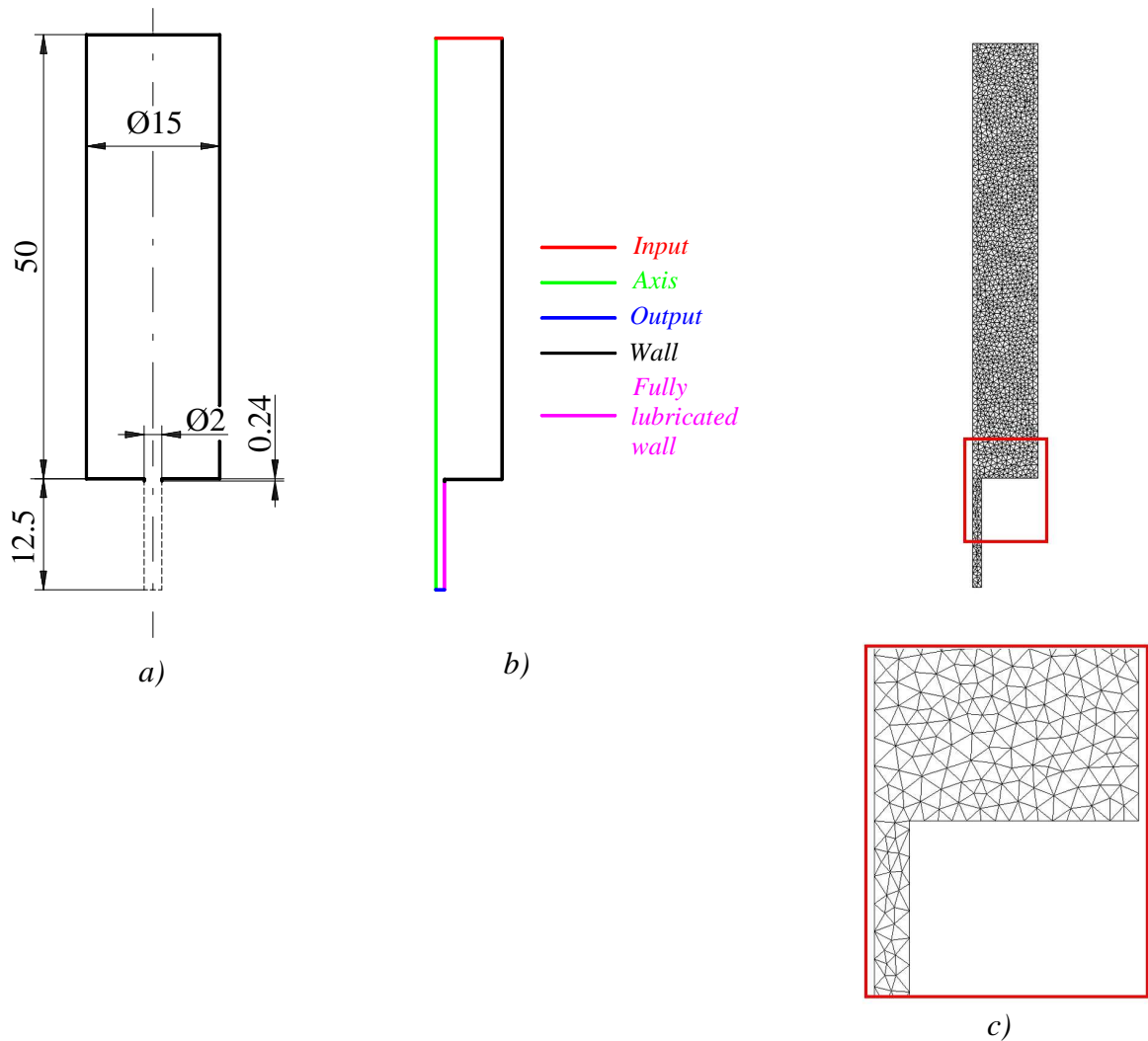


Fig. 44: Details for theoretical ideal orifice die analysis where downstream region is not filled by the polymer melt (a – geometrical sketch of ideal orifice die, b – boundary conditions, c – FEM mesh)

The FE mesh used for abrupt contraction flow modeling consists of 2949 elements with 6094 nodes, which sufficiently describes the flow domain and gives enough precise results. Edge length was chosen 0.8 mm and due to low flow rates iteration level in our research was 10^{-12} . Number of iterations was 100 and for shear rates lower than 0.03 s^{-1} was even 200. Furthermore, non – Newtonian/temperature iteration was considered and effects of inertia and gravity were neglected.

It should be mentioned that in all calculations, it is assumed that the polymer melt does not swell and that the free surface boundary conditions for free jet flow can be replaced with a wall with absolute slip (only the axial wall velocity component is allowed to vary, and the wall radial velocity is equal to zero). This assumption has several advantages. First, it allows simulation of free jet flow in which the velocity rearrangement at the end of the die is taken into account. This is the main advantage in comparison with simulations that do not consider any free jet flow. Secondly, the no-extrudate-swell assumption simplifies the flow situation, so that calculations can be made at much higher flow rates.

In order to demonstrate the role of material extensional properties on the generation of the entrance pressure drop for different polymer melts flow through an abrupt contraction, *LDPE Escorene LD 165 BW1* and four *virtual materials* (see *Fig. 52*) were used. The calculated results, in terms of entrance viscosity, are depicted in *Fig. 53* and the parameters of entrance pressure drop model are summarized in *Tab. 6*. It is clearly visible that all materials showing extensional strain hardening in the uniaxial extensional viscosity (see *Fig. 52*) also yield overshoot in the entrance viscosities (see *Fig. 53*) which is consistent with the open literature [33] supporting the validity of the used numerical approach in this work.

Tab. 6: Entrance pressure drop model (Eq. (23)) parameters for both, real (LDPE Escorene LD 165 BW1) and virtual (M1, M2, M3 and M4) materials

Function	Entrance pressure drop model				
Material	$\eta_{\text{ENT},0}$ (Pa.s)	λ' (s)	a' (-)	α' (s)	ξ' (-)
LDPE Escorene LD 165BW 1	59,550.14209	0.581123	0.6064556417	15.834387	0.299492
Virtual material M1	57,758.09353	0.782182	0.5951470027	17.037560	0.292668
Virtual material M2	55,776.31681	0.976292	0.5902599899	18.775613	0.276932
Virtual material M3	57,806.94014	1.497522	0.5749431565	16.035987	0.244389
Virtual material M4	61,906.54042	0.940443	0.6261065864	0.000000	0.000000

With the aim to test the applicability of Binding, Cogswell and Gibson model to predict uniaxial extensional viscosity, firstly, the entrance pressure drop model, Eq. (23), was used to fit theoretical entrance viscosity for each particular materials (see *Fig. 53*) and secondly, all models were utilized to calculate uniaxial extensional viscosity according to

corresponding equations provided in *Chapter 2.2*. All data needed for such calculation were taken from the numerical simulations. Moreover, *effective entry length correction* was used for all considered models.

Comparisons between the calculated extensional and theoretical viscosities are given in *Figs. 54-58*. It is shown that all used entrance techniques predict the same extensional viscosity plateau at low shear rates due to the applied *effective entry length correction*. The comparison between theoretical and calculated extensional viscosities with the applied correction for extensional strain hardening polymer melts (see *Figs. 54-58*) leads to the following conclusions:

- All methods seem to capture the same and proper slope of the extensional viscosity at high extensional rates.
- Binding model overpredicts and underpredicts η_E at low and high $\dot{\epsilon}$, respectively.
- Gibson model significantly underpredicts η_E at both, low and high $\dot{\epsilon}$.
- Cogswell model underpredicts η_E for highly extensional strain hardening melts, i. e. if the maximum uniaxial extensional viscosity divided by 3 times Newtonian viscosity, $\eta_{E_{\max}}/(3\eta_0)$, is higher than 2. On the other hand, for low extensional strain hardening materials where $\eta_{E_{\max}}/(3\eta_0) \leq 2$, Cogswell model predicts η_E very precisely within wide range of extensional strain rates.

The *Fig. 58* compares theoretical and calculated extensional viscosities with the applied correction for extensional strain thinning polymer melt. It is nicely visible that both, Binding and Gibson models provide reasonable good agreement between calculated and predicted η_E . On the other hand, the Cogswell model tends to overpredicts the uniaxial extensional viscosity especially at high extensional strain rates.

Interesting question is whether there is mathematical relationship between uniaxial extensional viscosity and entrance viscosity. The *Fig. 59* shows maximum uniaxial extensional viscosity divided by 3 times Newtonian viscosity, $\eta_{E_{\max}}/(3\eta_0)$, as a function of maximum entrance viscosity divided by entrance viscosity plateau, $\eta_{ENT_{\max}}/\eta_{ENT,0}$. It seems that exponential function given by Eq.(97) can be used to captured such dependence.

$$\frac{\eta_{E_{\max}}}{3\eta_0} = \exp \left\{ C \left[\ln \left(\frac{\eta_{ENT_{\max}}}{\eta_{ENT,0}} \right) \right]^D \right\} \quad (97)$$

where $C = 3.98$ and $D = 2.85$. Note, that both parameters were determined by the last square minimization method. It is believed that this relationship can be used to predict level of extensional strain hardening from the measured entrance viscosity for variety of branched polymers, which of course has to be tested experimentally.

Theoretical effect of die design on the measured extensional rheology

In this part, the effect of the orifice die design on the measured entrance viscosity and consequent extensional viscosity calculation has been investigated. In more detail, it may happen that, due to quite narrow downstream orifice die region (see *Fig. 41* for more detail) and extrudate swell, the polymer melt starts to fill this region. Therefore, if this happens, the question is how much this flow situation influences the measured entrance viscosity/uniaxial extensional viscosity. In order to answer this question, *virtual material M2* (having medium level of extensional strain hardening) has been chosen for FEM analysis for the case considering that downstream orifice die region is filled by the polymer melt. The sketch of such flow situation for conventional orifice die together with corresponding boundary conditions and FE mesh is provided in *Fig. 45* (grid consists of 7400 nodes and 3553 elements). The problem has been solved for different flow rates and the obtained theoretical results were plotted in *Fig. 60* and compared with corresponding theoretical data considering that downstream orifice die region is not filled by the polymer melt. In this *Figure*, it is clearly visible that entrance viscosities for both cases differ significantly within wide range of apparent shear rates. In addition, entrance viscosity parameters for this material are provided in *Tab. 7*.

Tab. 7: Parameters of entrance pressure drop model (Eq. (23)) for virtual material M2

<i>Function</i>	<i>Entrance pressure drop model</i>				
<i>Downstream die region type</i>	$\eta_{ENT,0}$ (Pa.s)	λ' (s)	a' (-)	α' (s)	ξ' (-)
<i>Unfilled</i>	55,776.31681	0.976292	0.5902599899	18.775613	0.276932
<i>Filled</i>	70,727.18176	0.654474	0.6011542038	18.599694	0.279597

In more detail, the fact that the polymer melt fills the downstream region of the orifice die leads to significant entrance viscosity increase due to additional shear flow component occurring at this region. The *Fig. 61* shows the impact of such artificial entrance viscosity increase on the uniaxial extensional viscosity determined by the corrected Cogswell model. Clearly, artificial entrance viscosity increase leads to artificial uniaxial extensional viscosity increase leading to higher level of disagreement between Cogswell model prediction and true shape of uniaxial extensional viscosity. In the other words, the main conclusion from this theoretical study is that very narrow downstream region may leads to erroneous estimation of the entrance viscosity leading to artificially high uniaxial extensional viscosity.

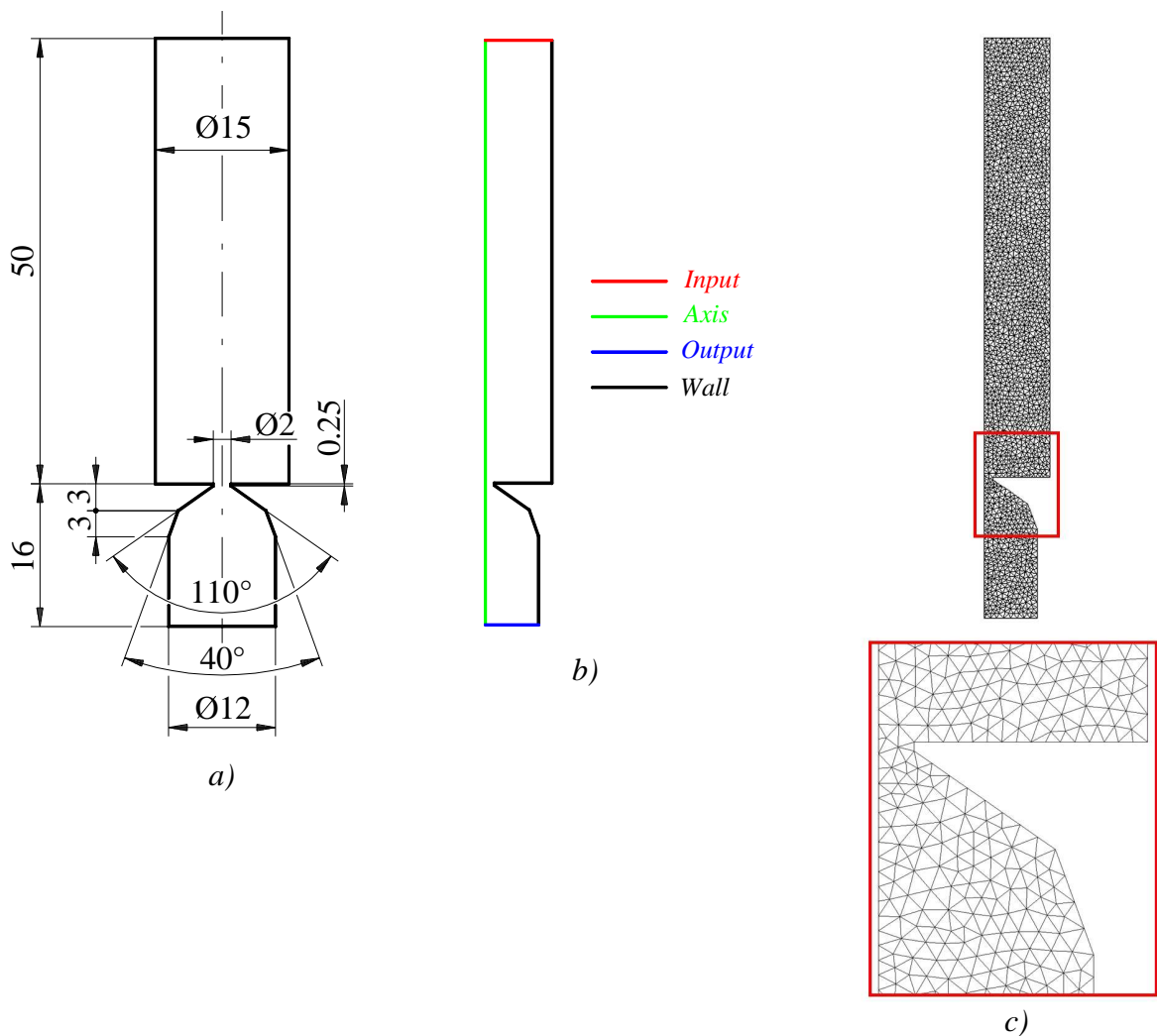


Fig. 45: Details for theoretical conventional orifice die analysis where downstream region is not filled by polymer melt (a – geometrical sketch of conventional orifice die, b – boundary conditions, c – FEM mesh)

Novel orifice die design

In order to prevent unwanted artificial entrance viscosity increase due to very narrow downstream channel, novel orifice die design has been proposed. The sketch of the novel orifice die design is depicted in *Fig. 46* whereas the more detailed geometry details are provided in the *Appendix VI* of this thesis.

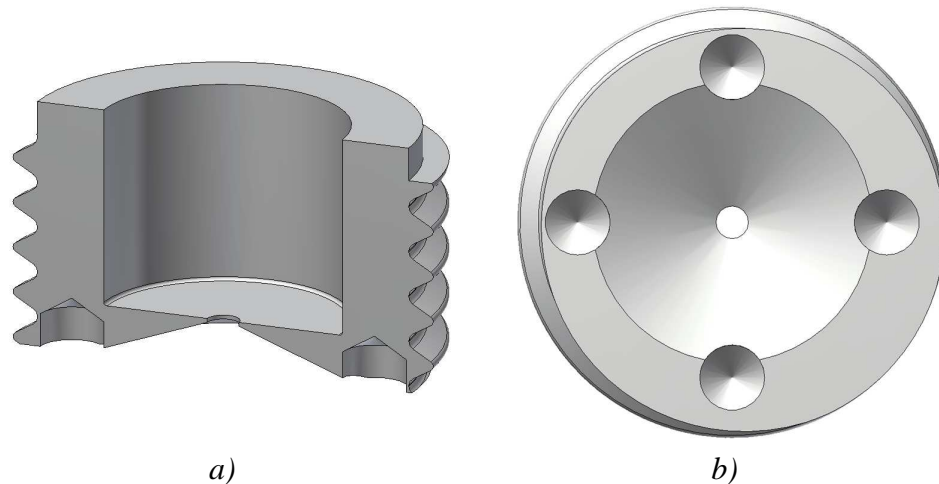


Fig. 46: Novel orifice die – section view (a), bottom view (b)

The main advantage of this novel orifice die design is occurrence of very open downstream region which consist of diverging channel and four holes which enables to use special key to crew-up the orifice die to the rheometer barrel. This downstream orifice die geometry practically eliminates any possibility for artificial pressure increase due to polymer melt sticks with the downstream wall. Moreover, possible detail view of the extrudate leaving the die during the measurements allow direct measurement of the free surface development during the extrudate swell which is practically impossible if one use the conventional orifice die design depicted in *Fig. 41*. Another expected advantage of this novel die design can be much precise detection of the melt rupture for the rupture stress determination in comparison with conventional orifice design where the melt rupture can be hidden if downstream region is filled by the polymer melt. In the next part, this novel orifice die design will be tested for different processing conditions and polymer materials.

Experimental evaluation of the novel orifice die design

For the experimental work, highly branched *LDPE Lupolen 1840H* was used. The uniaxial extensional viscosity data measured on the SER at 150°C were taken from the

open literature [15] whereas the high shear rate viscosity data were measured on *Rosand RH7-2* twin – bore capillary rheometer by using novel orifice die at three different temperatures (150°C, 200°C and 250°C). The modified White-Metzner model was used to fit both, shear and uniaxial extensional viscosity data (see *Fig. 62*). Moreover, the vortex size development predicted by FEM for *LDPE Lupolen 1840H* flow through abrupt contraction provided in *Fig. 63* clearly shows non-monotonic trend between vortex size and mass flow rate which is consistent with recent findings [67]. This indicates that both shear and extensional rheological properties for *LDPE Lupolen 1840H* are determined correctly and thus this material can be taken as the reference material for further rheological analysis. The modified White-Metzner model parameters are provided in *Tab. 8*.

Tab. 8: Temperature dependent modified White – Metzner model parameters (Eq. (86), (87), (88) and (91)) for LDPE Lupolen 1840H

Function	Temperature dependent modified White-Metzner model							
Material	η_0 (Pa.s)	λ (s)	a (-)	\bar{n} (-)	A (°C ⁻¹)	T_0 (°C)	λ_0 (s)	K_1 (-)
<i>LDPE Lupolen 1840H</i>	59,950	0.5834	0.3282	0.1000	0.0281	150	197.95	237.80

In the first step, both conventional and novel orifice dies has been used to determine entrance viscosity for *LDPE Lupolen 1840H* at 250°C, which is typical processing temperature for the film casting process. The result together with the closer view of the orifice downstream region during measurement is provided in *Fig. 64*. As expected from the theoretical study, entrance viscosity measured by the conventional orifice die is much higher in comparison with novel die design, clearly, due to the fact that polymer melt fills the downstream region of the conventional orifice die. Also, the level of the extrudate swell from the conventional orifice die is artificially high due to that reason. This leads to the conclusion that the measurements of the extensional rheology at high processing conditions is highly erroneous and novel orifice die design should be preferred.

With the aim to compare both orifice dies at the processing condition where the downstream region is not filled by the polymer melt, rheological testing has been done at 150°C. Experimentally determined entrance viscosity as the function of the apparent shear rate by using conventional and novel orifice dies is depicted in *Fig. 65*. In this case, the

entrance viscosity determined from novel orifice die is slightly lower in comparison with conventional orifice die measurements. This can possibly be caused by relatively small diverging angle of the downstream wall in conventional orifice die design (see *Fig. 41*) which can promote slight or partial stick between polymer melt and die wall at that region causing slight, artificial entrance viscosity increase.

As the result, in the further investigation, only novel orifice die design will be used for the experimental work.

Another difficulty to determine precise values of entrance viscosity at very low apparent shear rates can be caused by imprecise piston speed regulation. The occurrence of such error can be investigated by using two orifice dies having two different diameters. In such case, different piston speeds are needed to achieve the same value of the shear rate on two orifice dies having different diameter (i.e lower piston speed is needed for smaller diameter orifice die and vice versa to achieve the same value of the apparent shear rate). The rheological tests have been performed for *LDPE Lupolen 1840H* polymer at 150°C by using two orifice dies having different diameter (2mm and 3 mm) and experimental data are depicted in *Fig. 66*. Clearly, high level of entrance viscosity distortion occurs at low apparent shear rates in the case of orifice die having diameter equal to 2mm only. Moreover the reproducibility of the measured entrance viscosity data is very low at that apparent shear rate range. On the other hand, by using orifice die having diameter equal to 3mm the entrance viscosity distortions at low apparent shear rates are significantly reduced as visible in *Fig. 67*. This leads us to the conclusion that the use of orifice die having 3mm in diameter should be preferred to get precise entrance viscosity data at low apparent shear rates range.

Experimental analysis of Binding, Cogswell and Gibson models

In this chapter, novel orifice die with properly chosen capillary diameter will be utilized to determine uniaxial extensional viscosity by using Binding, Cogswell and Gibson models for highly branched (*LDPE Lupolen 1840H*), slightly branched (*mLLDPE Exact 0201*) and linear polymers (*HDPE Tipelin FS 450 – 26*).

In the first step, entrance viscosity has been determined for all three samples by the use of the novel orifice die and consequently fitted by the entrance pressure drop model, Eq.(23) as depicted in *Figs. 67-69* and fitting parameters are provided in *Tab. 9*.

Tab. 9: Parameters of entrance pressure drop model (Eq. (23))

Function	Entrance pressure drop model				
Material	$\eta_{ENT,0}$ (Pa.s)	λ' (s)	a' (-)	α' (s)	ξ' (-)
LDPE Lupolen 1840H	29,647.25498	0.051010	0.6599534062	19.951935	0.256709
mLLDPE Exact 0201	19,010.49081	0.420384	0.3817786899	6.012095	0.306068
HDPE Tipelin FS 450 - 26	1000,000.00000	8.004018	0.5778474780	0.000000	0.000000

It is nicely visible that in all three cases, Eq.(23) represents the measured viscosity data very well. In the second step, *effective entry length correction* has been applied for entrance viscosity data with respect to Binding, Cogswell and Gibson model. Finally, the extensional viscosities have been calculated for the all three samples according to all three techniques and consequently compared with SER steady state extensional viscosity data reported in the literature [15], [68] as visible in *Figs. 70-78* (the shear viscosity data needed for the uniaxial extensional viscosity calculation were measured on *Rosand RH7-2* twin – bore capillary rheometer; corresponding Carreau-Yasuda model fitting parameters are provided in *Tab.10*).

Tab. 10: Fitting parameters of Carreau – Yasuda model (Eq. (87))

Function	Carreau – Yasuda model			
Material	η_0 (Pa.s)	λ (s)	a (-)	\bar{n} (-)
LDPE Lupolen 1840H	59,950	0.5834	0.3282	0.1000
mLLDPE Exact 0201	17,998	5.6062	1.3639	0.6029
HDPE Tipelin FS 450 – 26	5,033,405	3.8745	0.1401	0.0653

It also has to be mentioned that the dotted line occurring in *Figs. 70-78* represents extensional viscosity calculated from the entrance viscosity fitting lines provided in *Figs. 67-69*, i.e. the fitting lines were taken as the measurements in this case. Closer analysis of these *Figures* reveals the following conclusions.

For highly branched *LDPE Lupolen 1840H* material where $\eta_{E_{max}}/(3\eta_0) = 3.9$, Binding model predicts extensional viscosity in good agreement with SER extensional viscosity data at low extensional extensional rates, whereas at medium and higher deformation rates the calculated data are underpredicted (see *Fig. 70*). Gibson model behaviour is even worse in this case, because calculated extensional viscosity is

underpredicted within whole extensional rate range (see *Fig. 71*). Finally, the Cogswell model gives good agreement between measured and calculated extensional viscosity at low and high extensional deformation rates but at medium deformation rates, the model underpredicts the measured data (see *Fig. 72*). Obviously, these observations are in good agreement with the conclusions obtained from theoretical analysis. Thus, we could conclude that for branched *LDPE Lupolen 1840H* polymer the Cogswell model predictions are more realistic in comparison with Binding and Gibson model in this case. The incapability of the Cogswell model to describe extensional viscosity data at medium deformation rates can be explained by the fact that the extensional strain hardening is too high in this case i.e. that $\eta_{E_{max}}/(3\eta_0) > 2$, which is consistent with the findings based on theoretical analysis.

For slightly branched *mLLDPE Exact 0201* material where $\eta_{E_{max}}/(3\eta_0) = 1.6$, Binding model overpredicts extensional viscosity at low extensional rates whereas at medium and high deformation rates, the extensional viscosity is underpredicted (see *Fig. 73*). Gibson model predicts extensional viscosity in good agreement with the measured SER data at low extensional rates, but at medium and high deformation rates, the extensional viscosity is underpredicted (see *Fig. 74*). Cogswell model predictions are surprisingly in excellent agreement with the measured SER extensional viscosity data as visible in *Fig. 75*. For slightly branched *mLLDPE Exact 0201* polymer, all above mentioned conclusions are in good agreement with the findings based on theoretical analysis for all three tested model. Here, it should be pointed out that the extensional strain hardening parameter for *mLLDPE Exact 0201* is $\eta_{E_{max}}/(3\eta_0) < 2$ i.e. it is in the range where, Cogswell model predictions are very precise as shown in the theoretical analysis.

For linear *HDPE Tipelin FS 450 – 26* where $\eta_{E_{max}}/(3\eta_0) = 1$, both, Binding and Gibson models gives excellent agreement with the measured SER extensional viscosity data within the experimentally determined extensional rates range (see *Figs. 76,77*). On the other hand, the Cogswell model failed in this case because the model overpredicts SER extensional viscosity data (see *Fig. 78*) within whole deformation rates range. Again all above mentioned conclusions for the linear *HDPE Tipelin FS 450 – 26* polymer are in very good agreement with corresponding conclusions obtained during theoretical analysis.

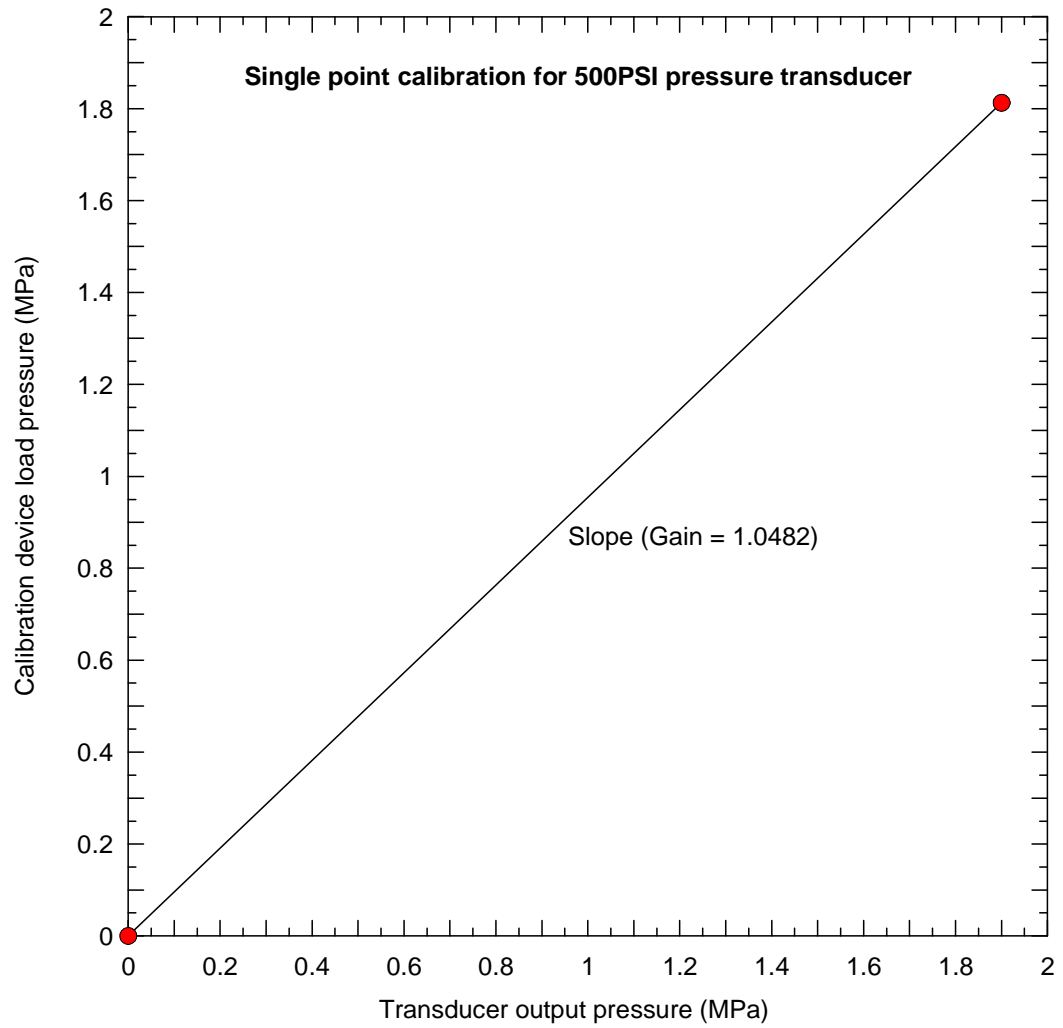


Fig. 47: Single point calibration curve for 500 PSI pressure transducer

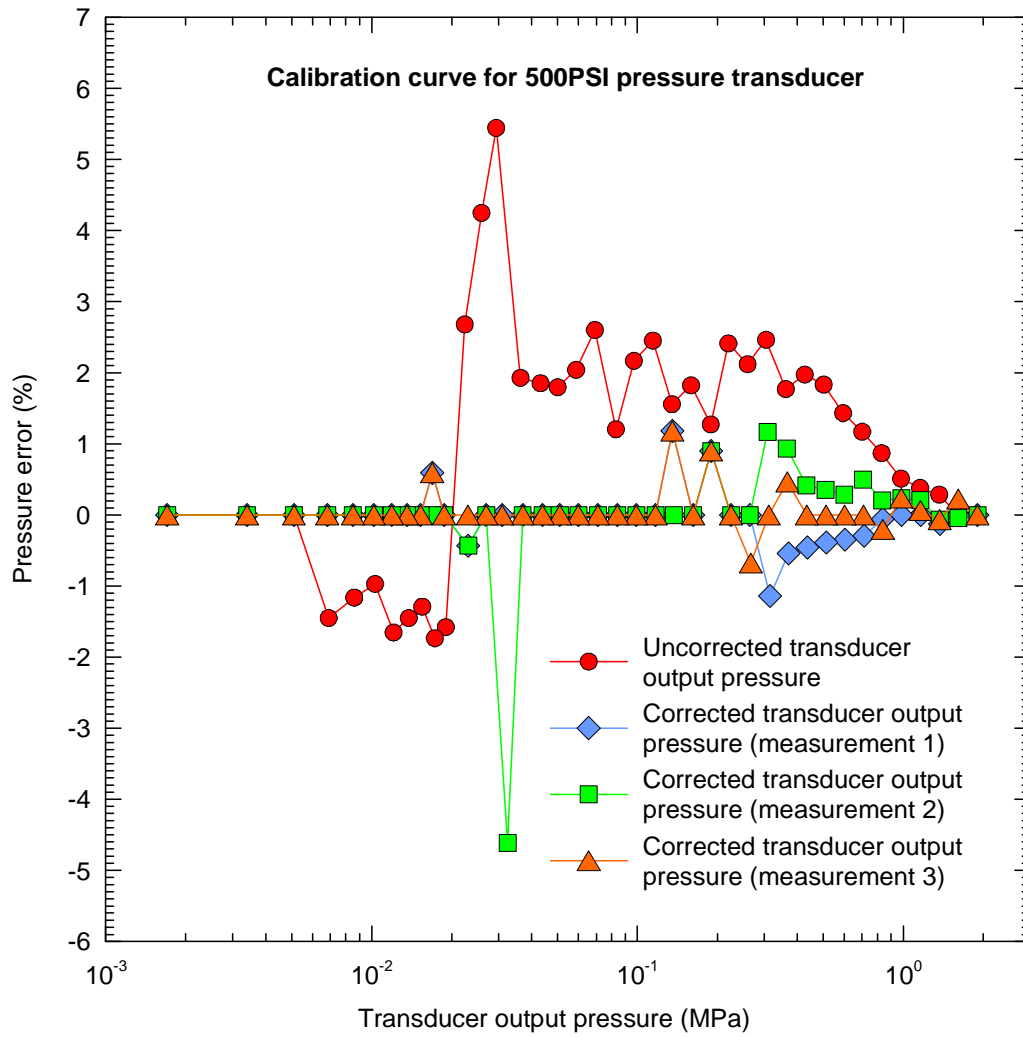


Fig. 48: Comparison between uncorrected (red circles) and corrected (green, blue and orange symbols) 500 PSI pressure transducer response

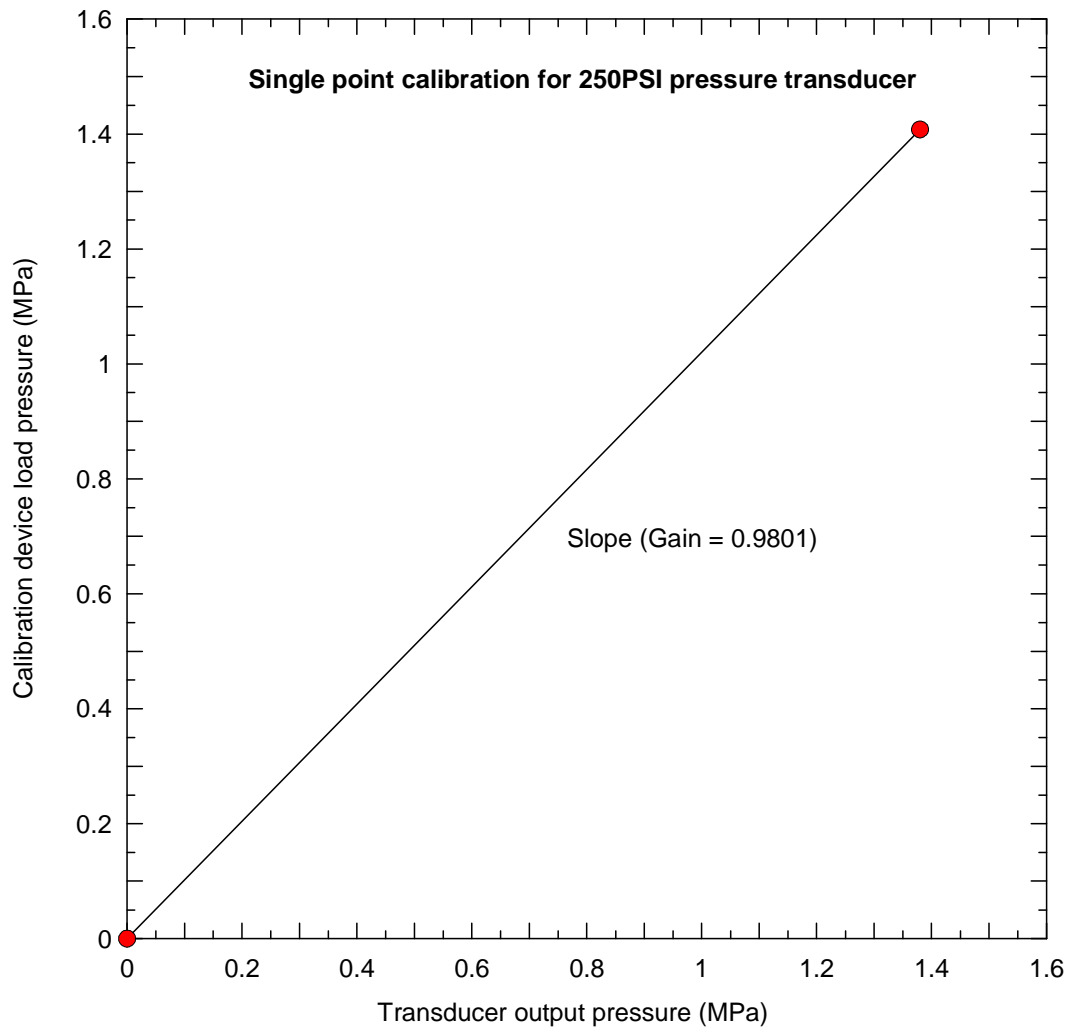


Fig. 49: Single point calibration for 250 PSI pressure transducer

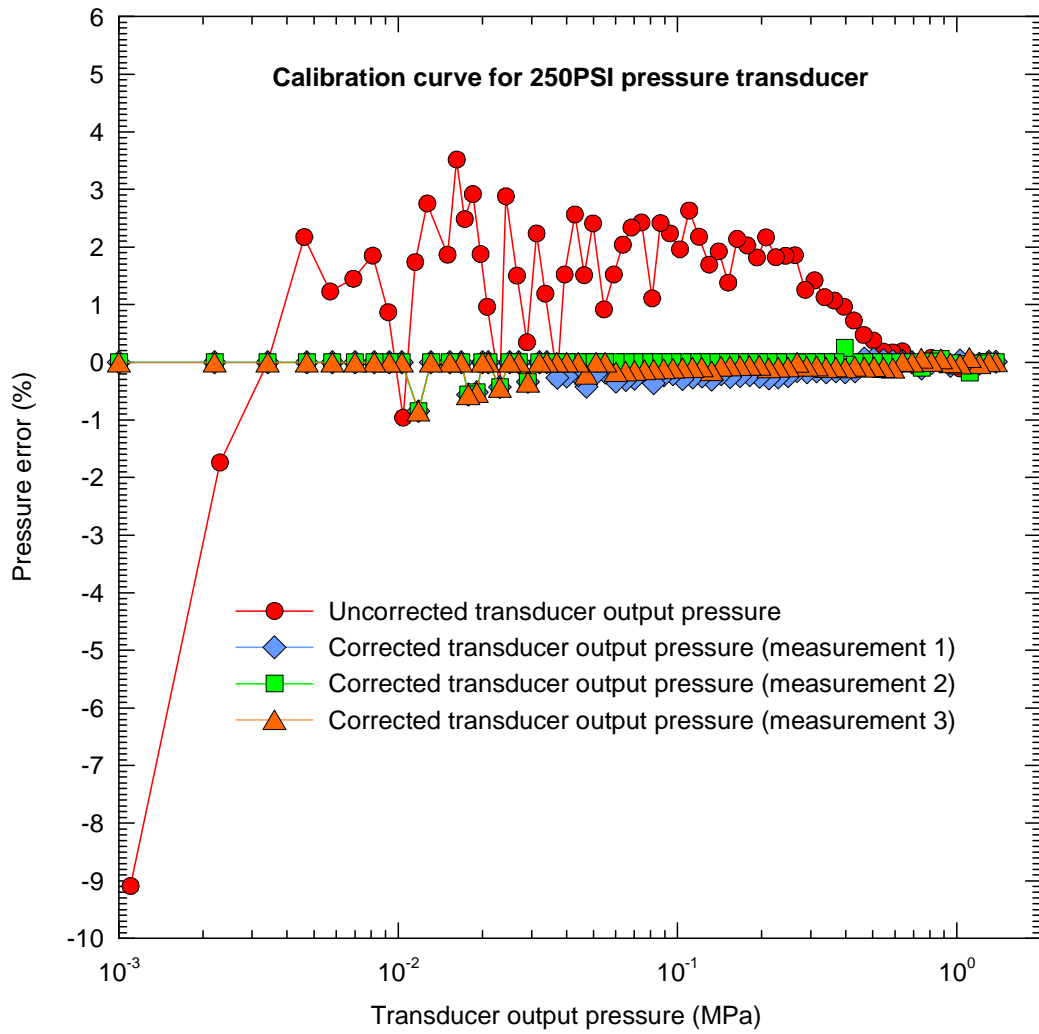


Fig. 50: Comparison between uncorrected (red circles) and corrected (green, blue and orange symbols) 250 PSI pressure transducer response

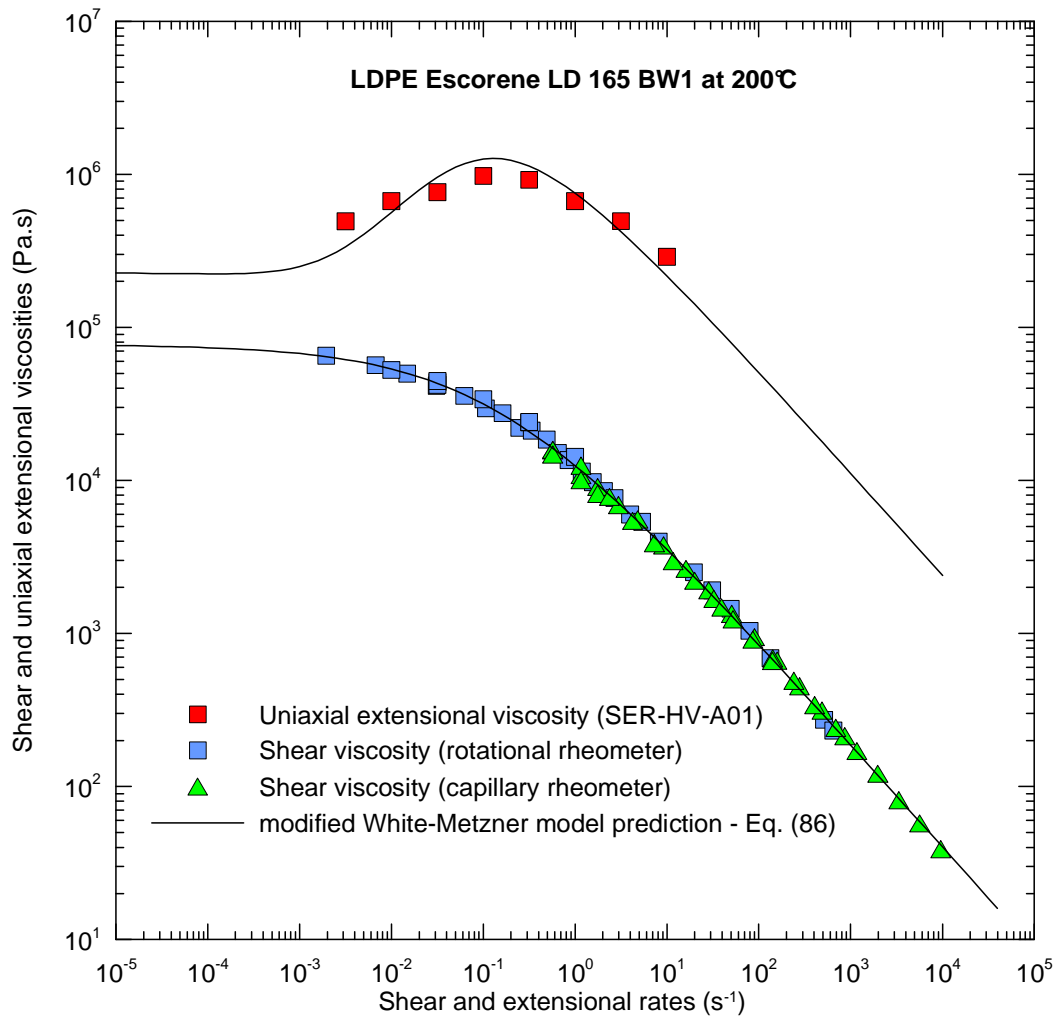


Fig. 51: Comparison between steady shear and uniaxial extensional viscosity data (symbols) and modified White-Metzner model predictions (lines) for LDPE Escorene LD 165 BW1 at 200 °C. Experimental data are taken from [65]

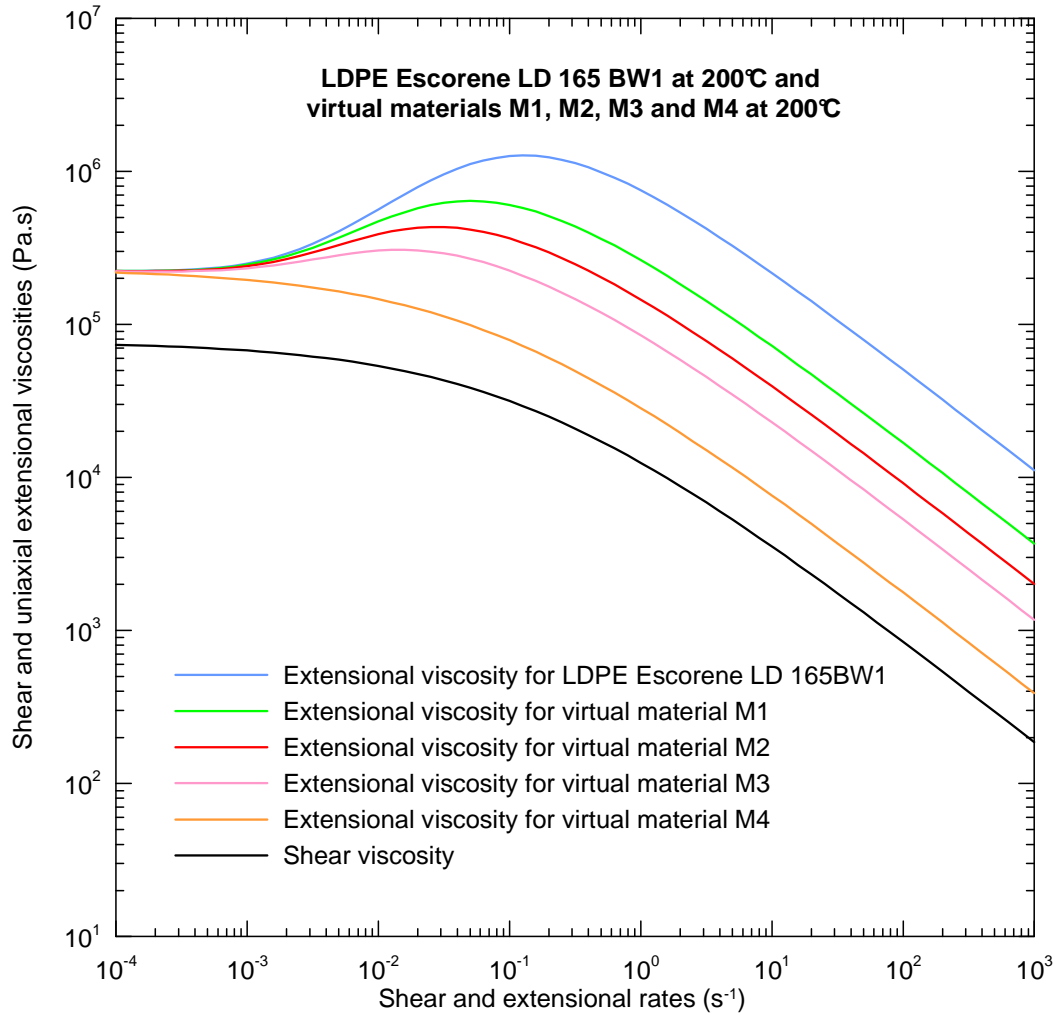


Fig. 52: Steady shear and uniaxial extensional viscosity curves predicted by modified White-Metzner model – Eq. (86) for LDPE Escorene LD 165 BW1 and four additional virtual materials (M1, M2, M3 and M4)

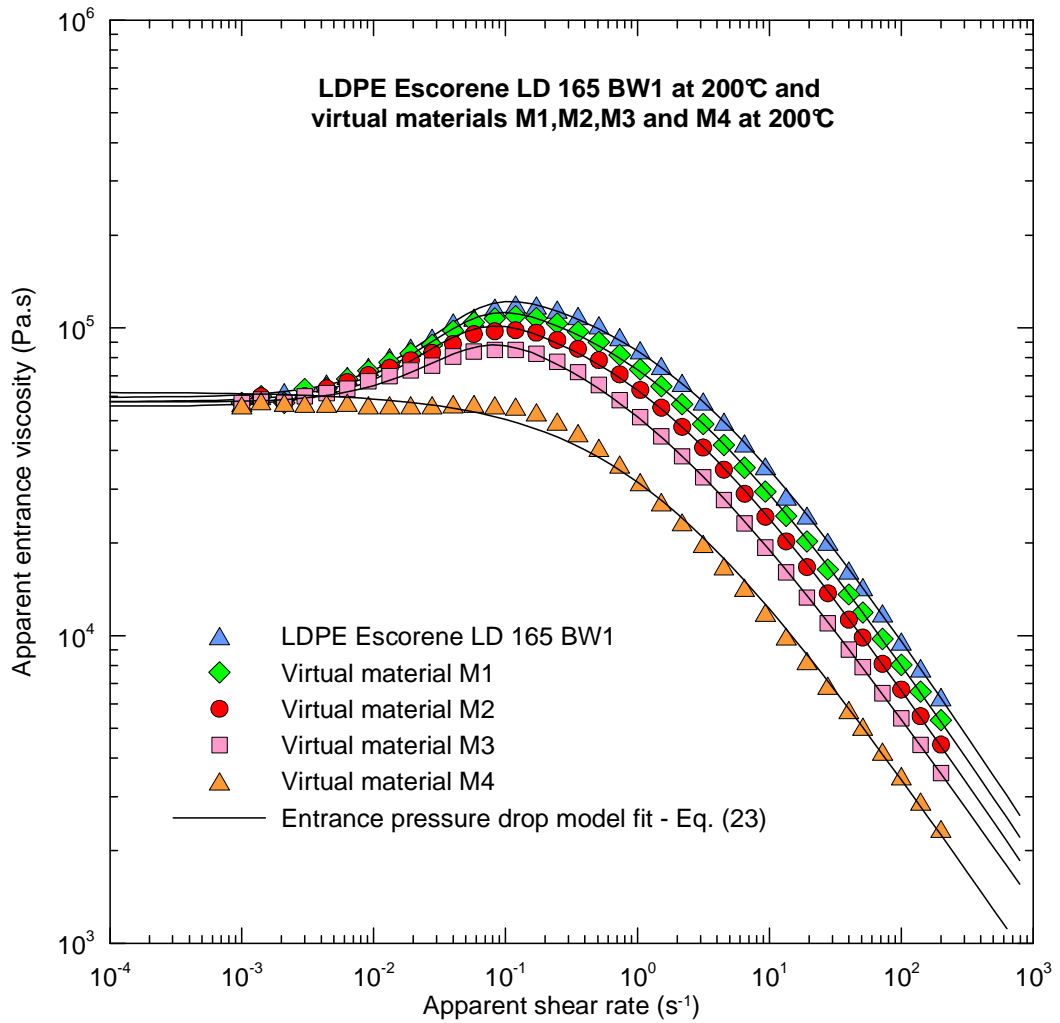


Fig. 53: Apparent entrance viscosity curves determined by viscoelastic FEM calculations for “ideal orifice die” depicted in Fig. 44

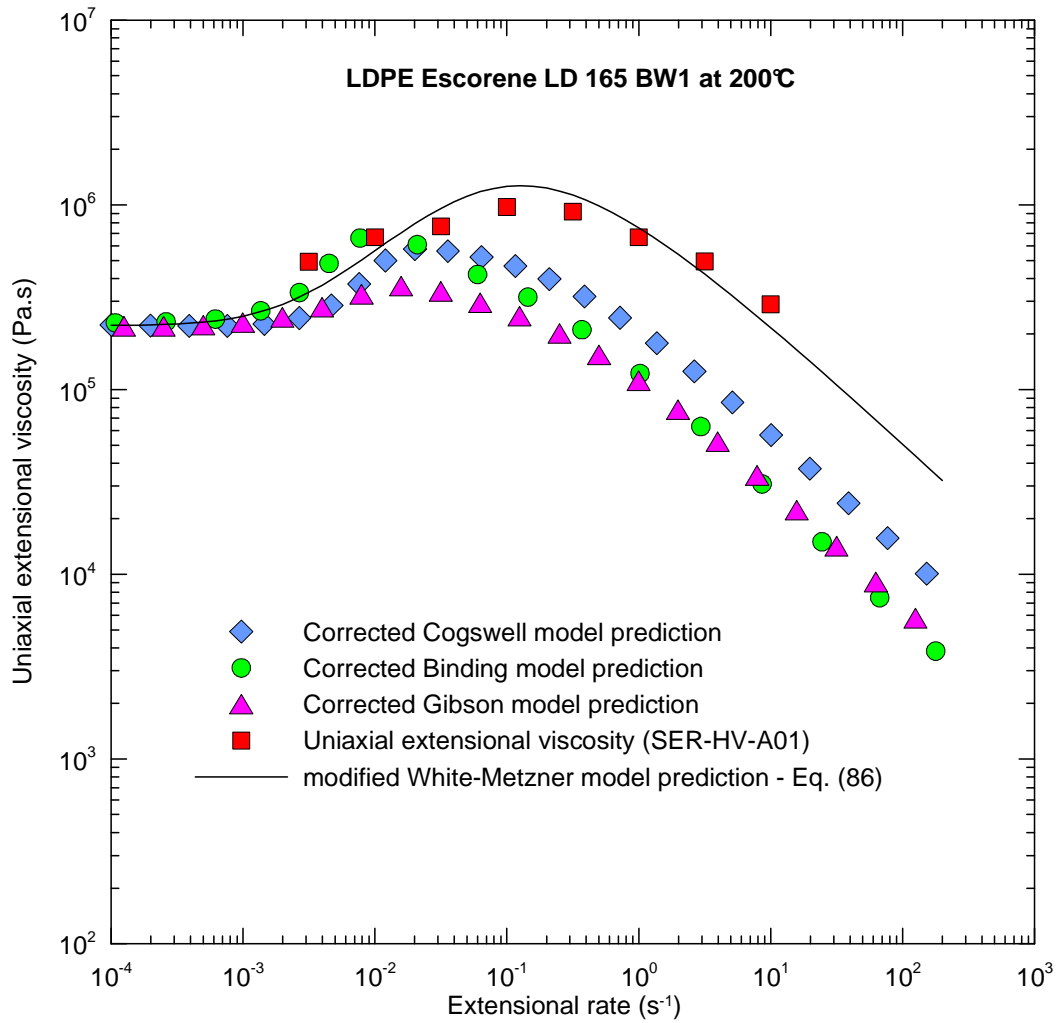


Fig. 54: Comparison of corrected Cogswell, Binding and Gibson predictions of extensional viscosity with modified White-Metzner extensional viscosity for LDPE Escorene LD 165 BW1 assuming “ideal orifice die” depicted in Fig. 44

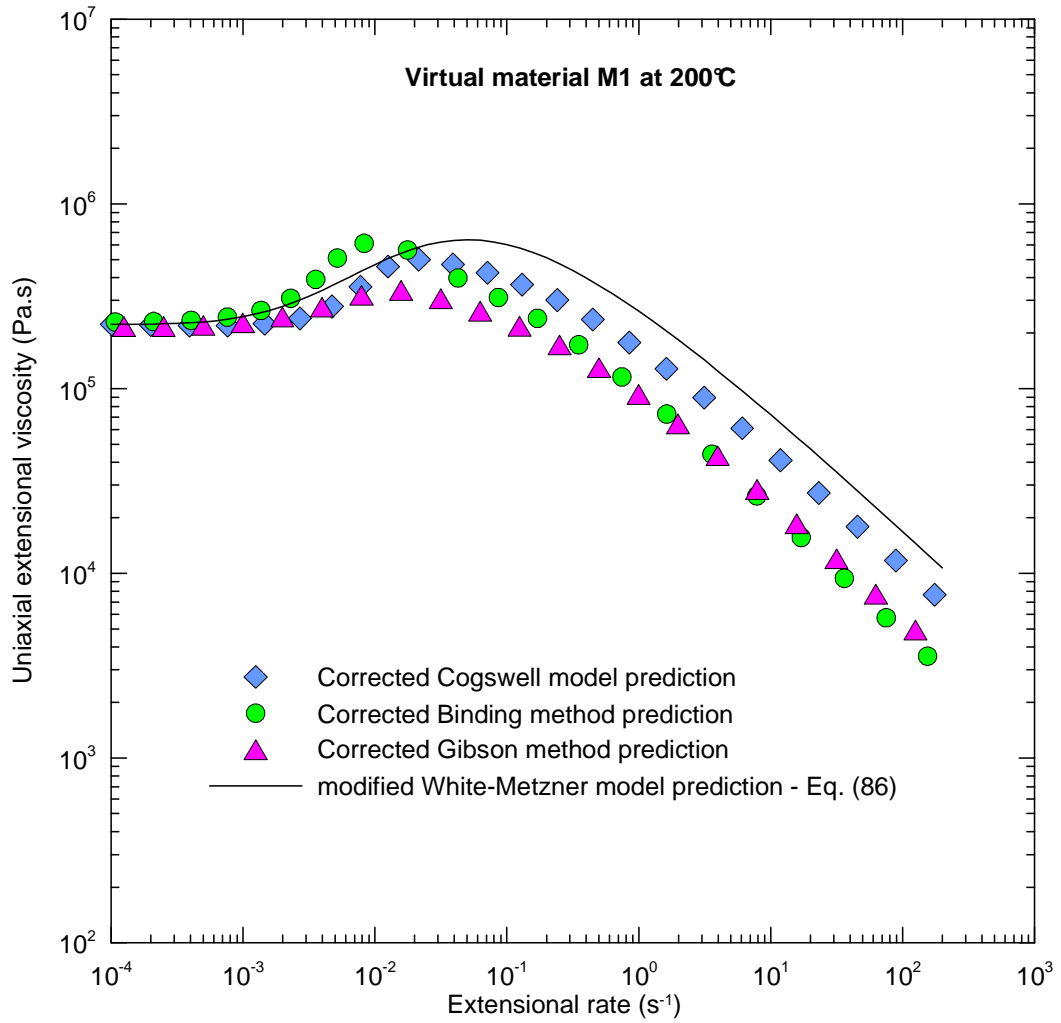


Fig. 55: Comparison of corrected Cogswell, Binding and Gibson predictions of extensional viscosity with modified White-Metzner extensional viscosity for virtual material M1 assuming “ideal orifice die” depicted in Fig. 44

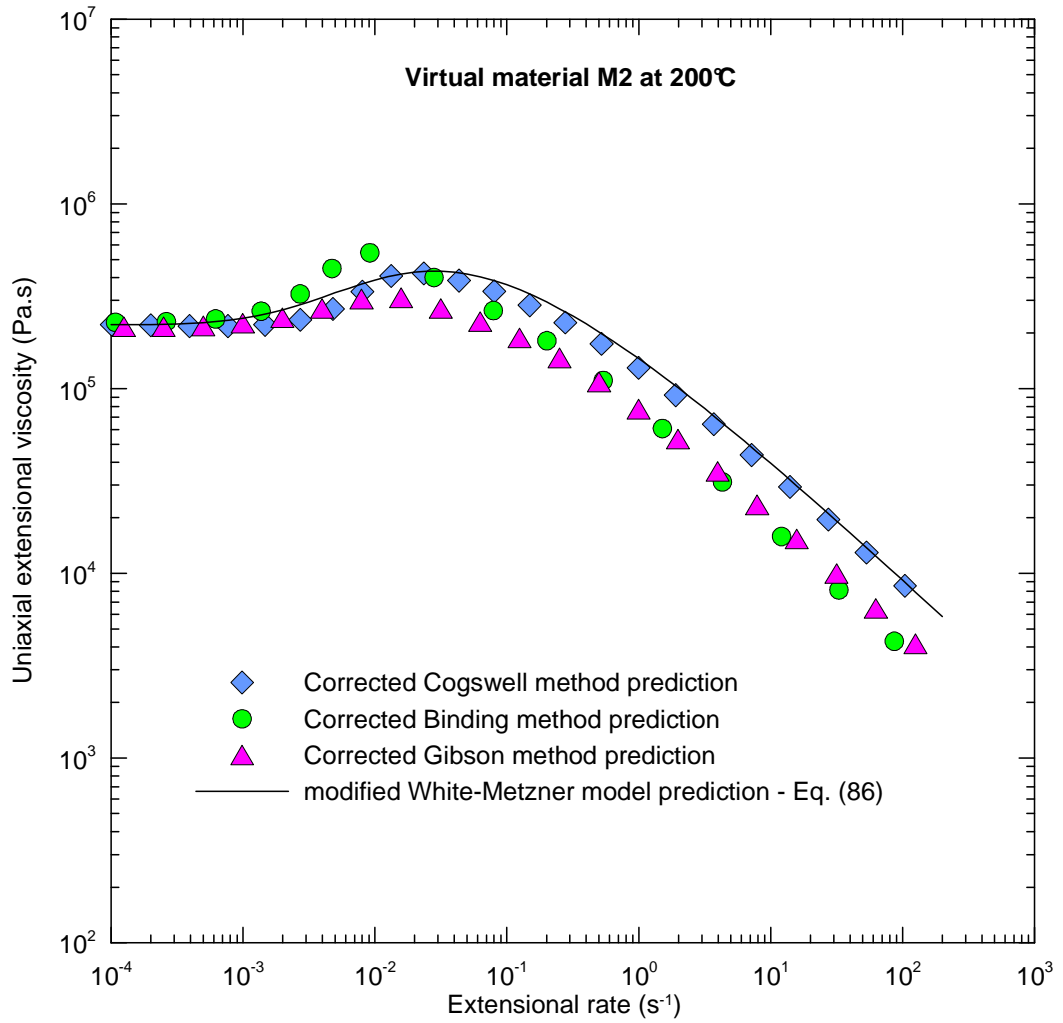


Fig. 56: Comparison of corrected Cogswell, Binding and Gibson predictions of extensional viscosity with modified White-Metzner extensional viscosity for virtual material M2 assuming “ideal orifice die” depicted in Fig. 44

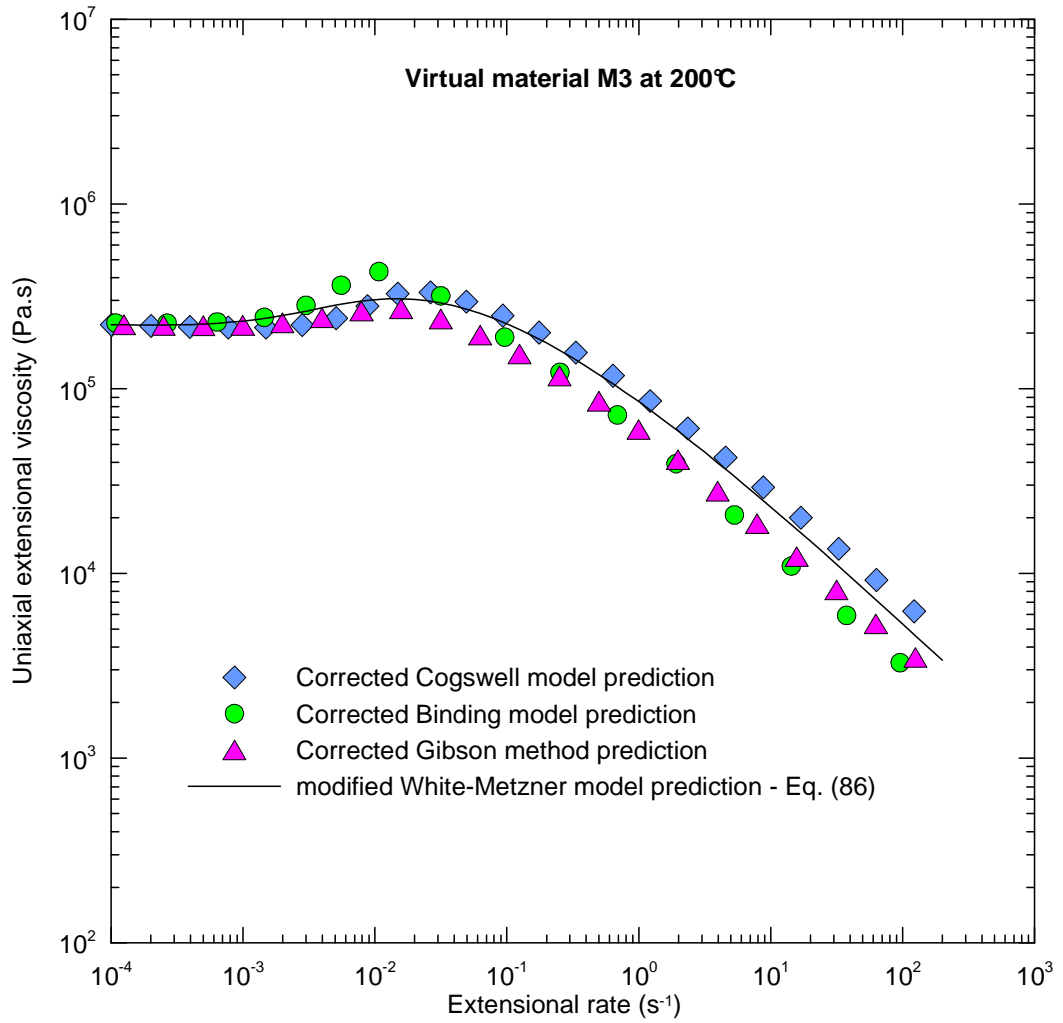


Fig. 57: Comparison of corrected Cogswell, Binding and Gibson predictions of extensional viscosity with modified White-Metzner extensional viscosity for virtual material M3 assuming “ideal orifice die” depicted in Fig. 44

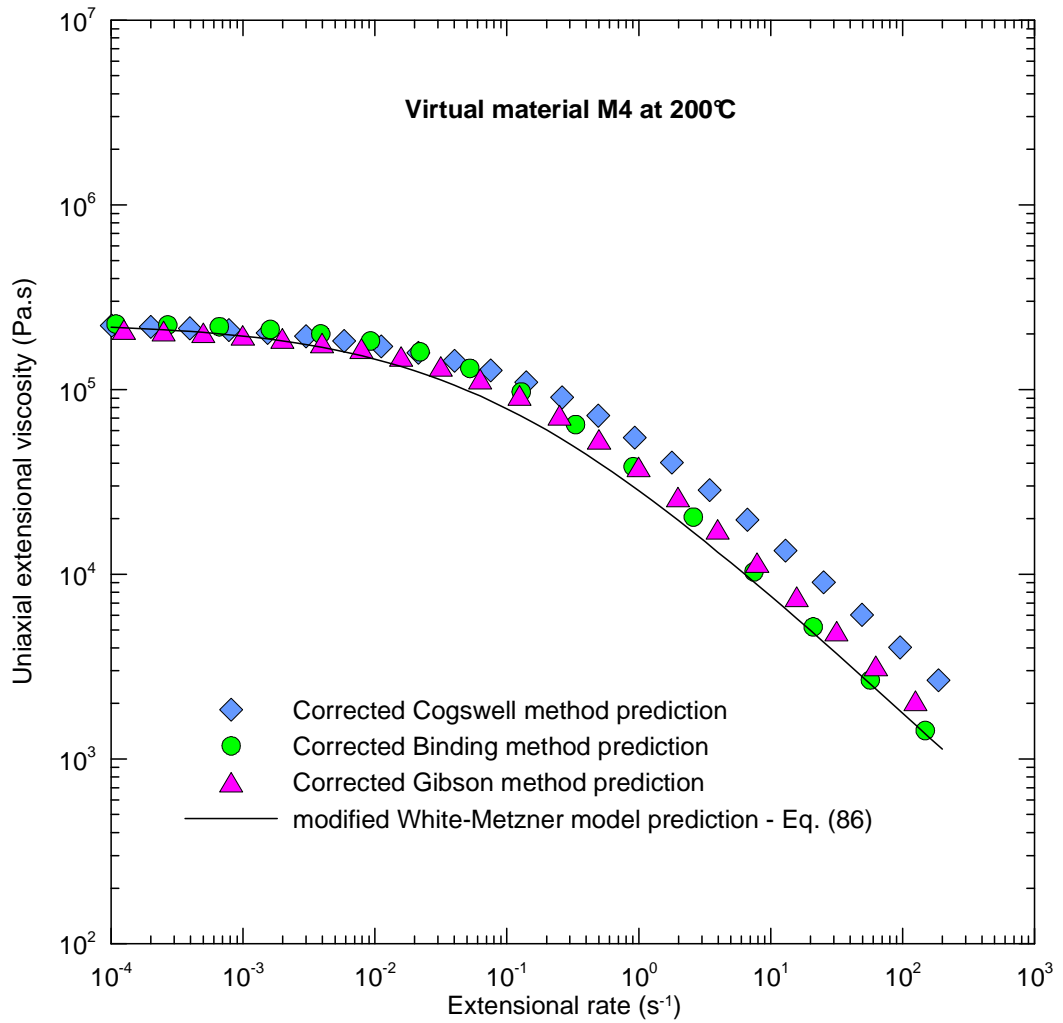


Fig. 58: Comparison of corrected Cogswell, Binding and Gibson predictions of extensional viscosity with modified White-Metzner extensional viscosity for virtual material M4 assuming “ideal orifice die” depicted in Fig. 44

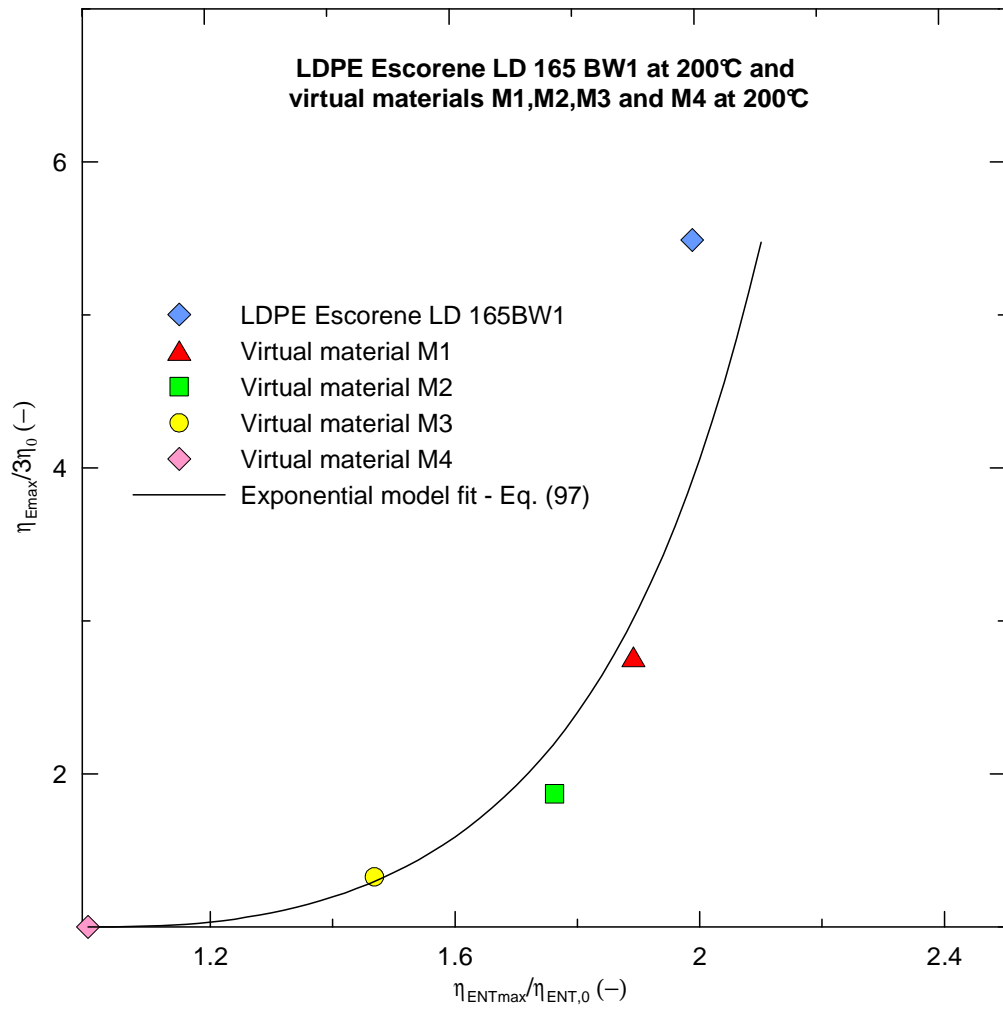


Fig. 59: Theoretically predicted relationship between attainable dimensionless maximum in uniaxial extensional viscosity curve and entrance viscosity curve for “ideal orifice die” depicted in Fig. 44

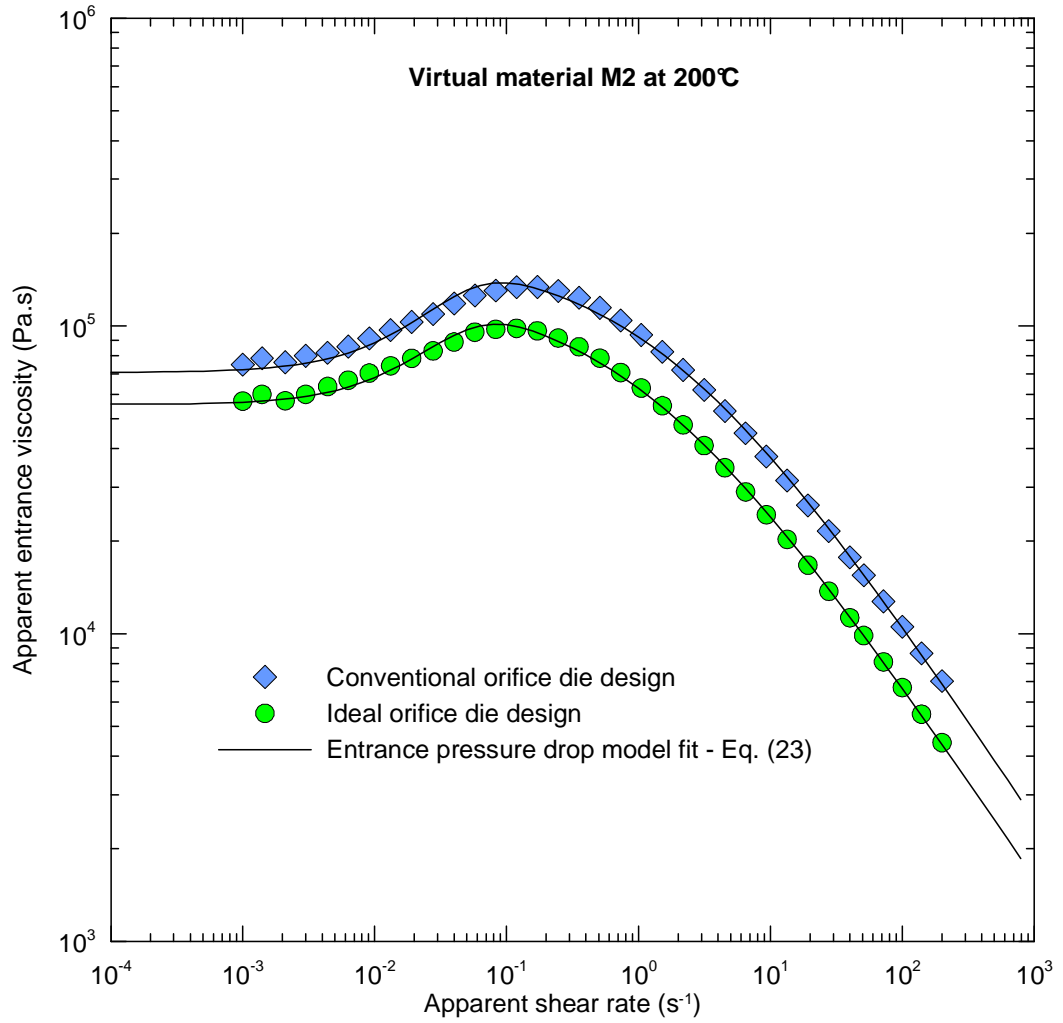


Fig. 60: Theoretically predicted effect of orifice die design on the entrance viscosity for virtual material M2

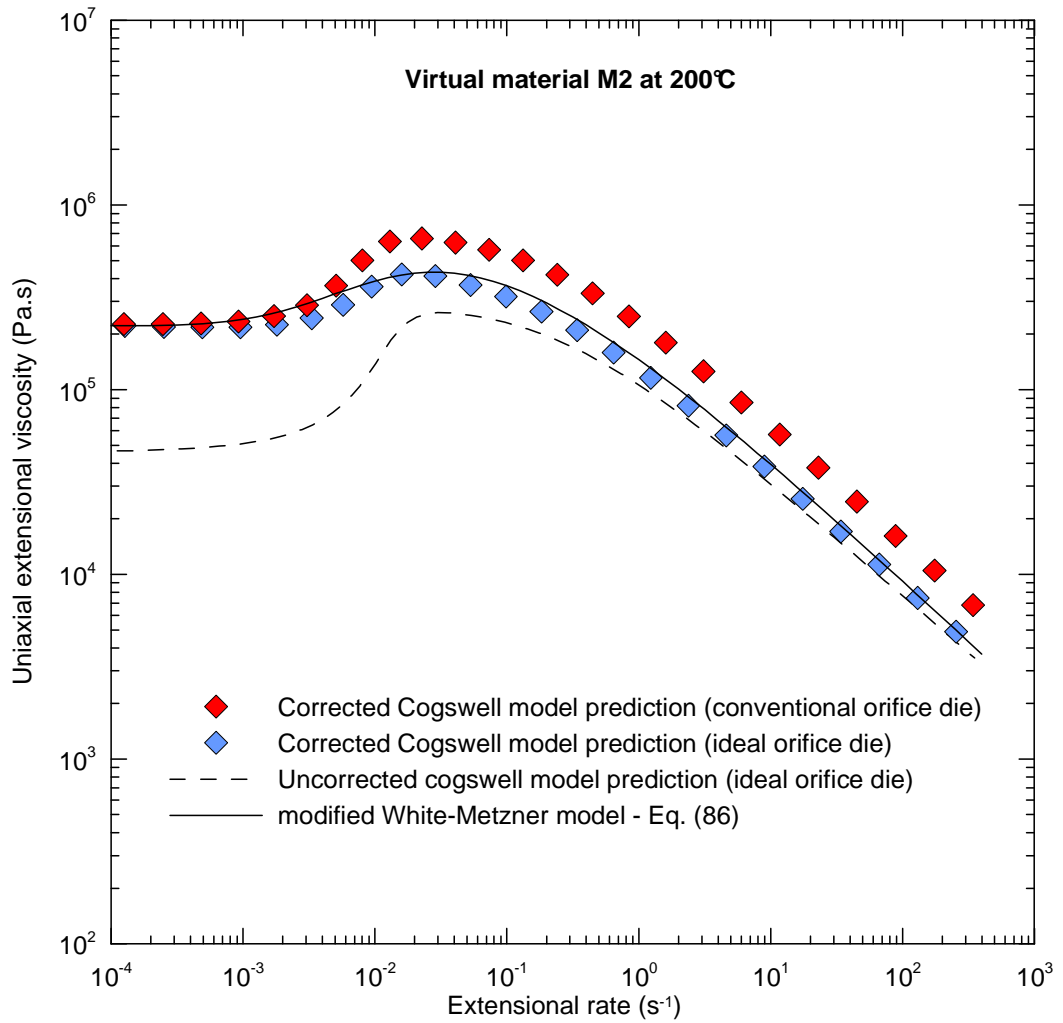


Fig. 61: Comparison between modified White-Metzner extensional viscosity and Cogswell predictions for virtual material M2 by using two different orifice dies

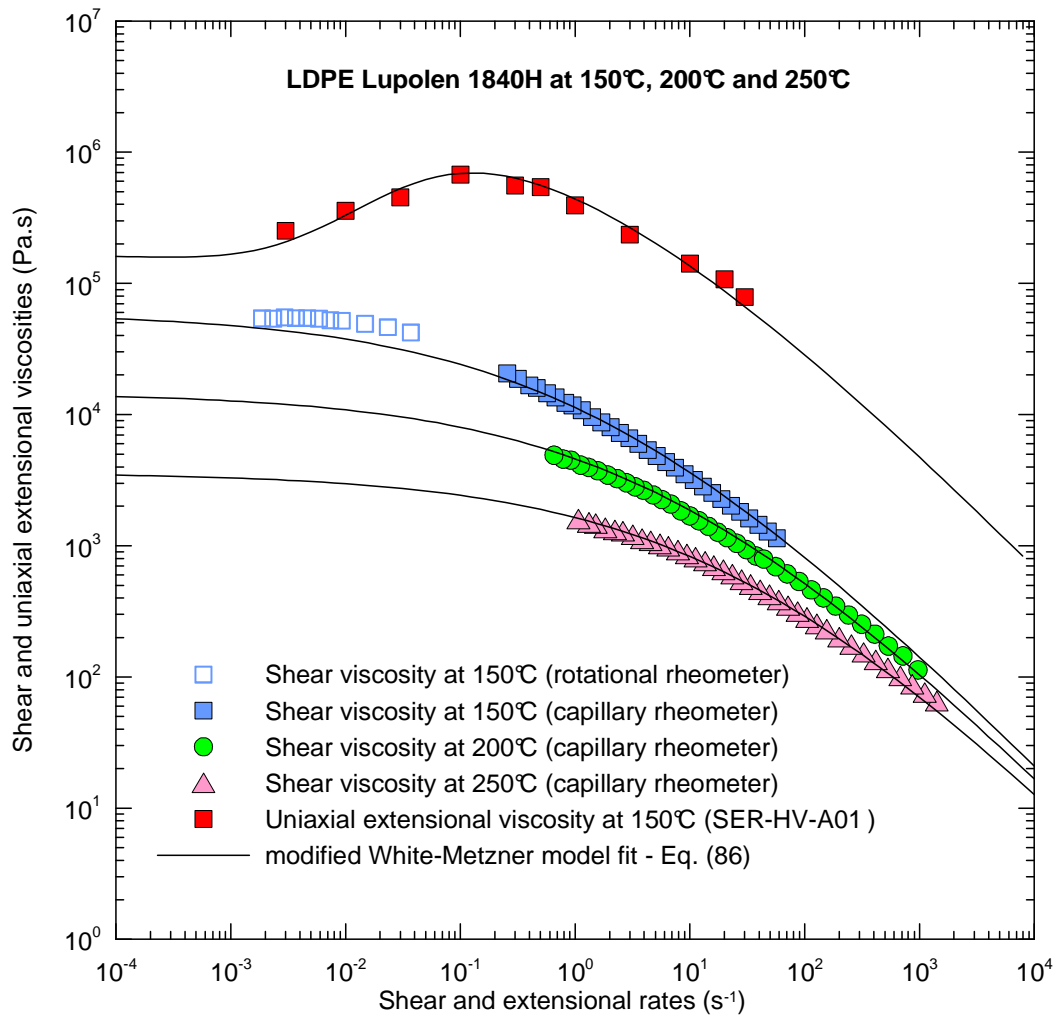


Fig. 62: Comparison between measured steady uniaxial extensional/shear viscosities and modified White-Metzner model predictions

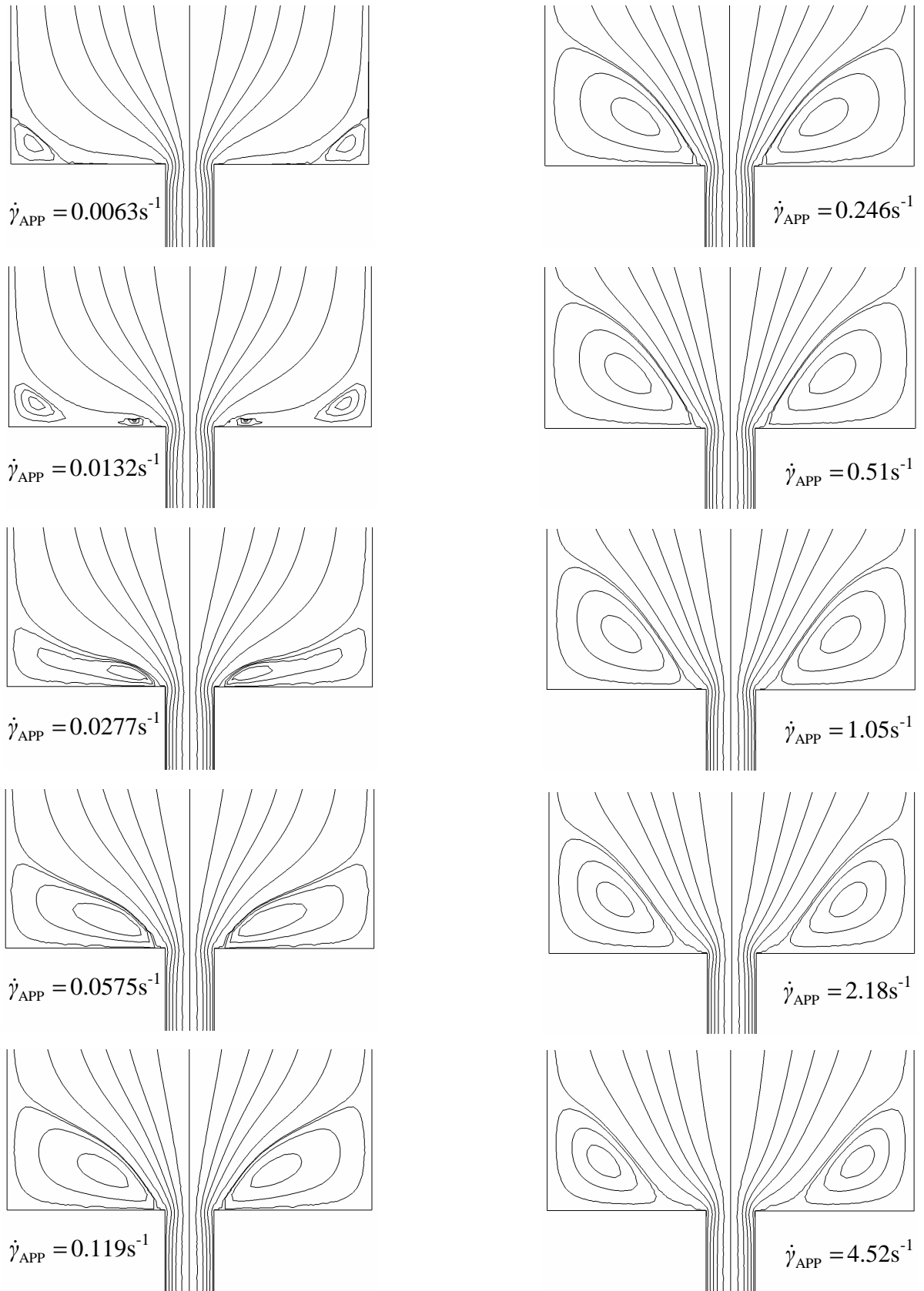


Fig. 63: Vortex size development predicted by the FEM calculation (using the modified White-Metzner model as the constitutive equation) for LDPE Lupolen 1840H melt flow through “ideal orifice die” (abrupt contraction flow) at 150°C for different mass flow rates

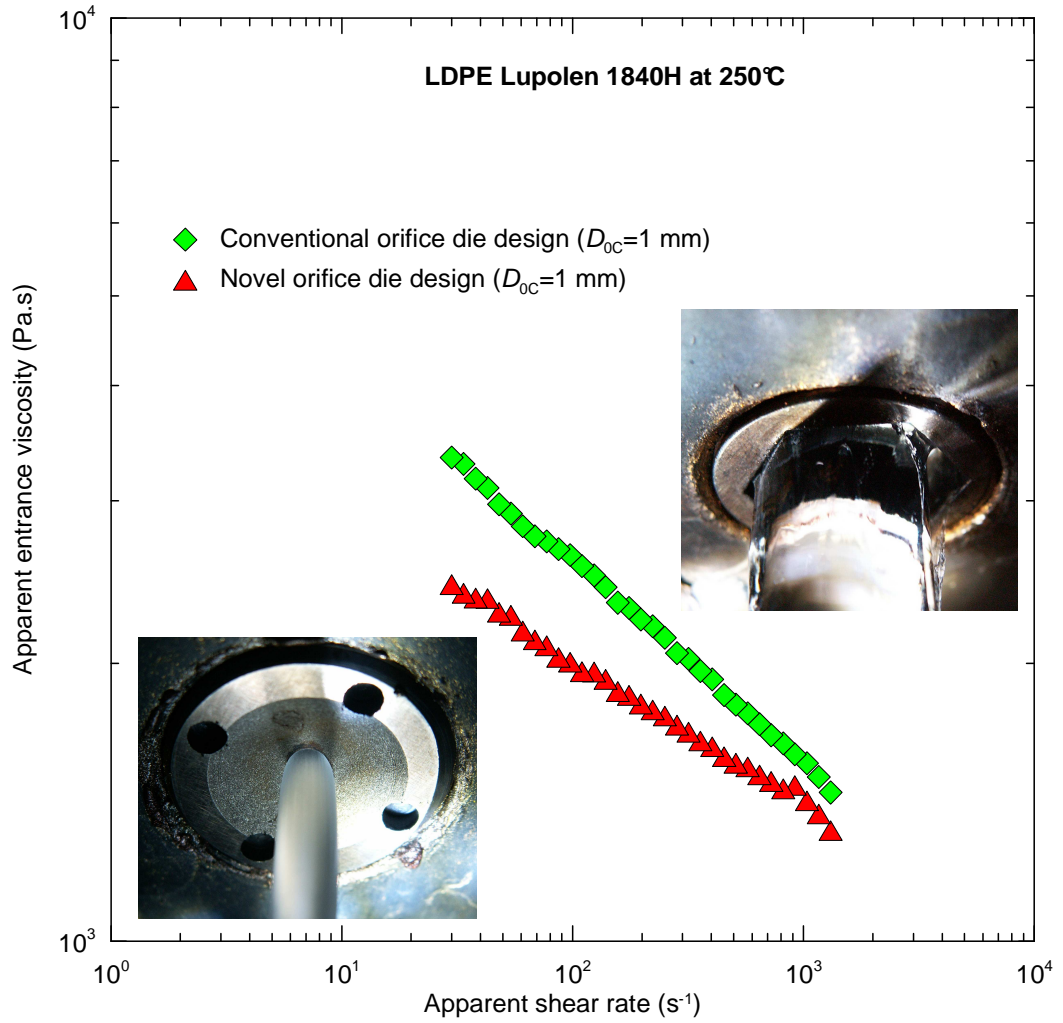


Fig. 64: Comparison between experimentally determined entrance viscosities by using conventional orifice die (green symbols) and novel orifice die (red symbols) for LDPE Lupolen 1840H at 250°C

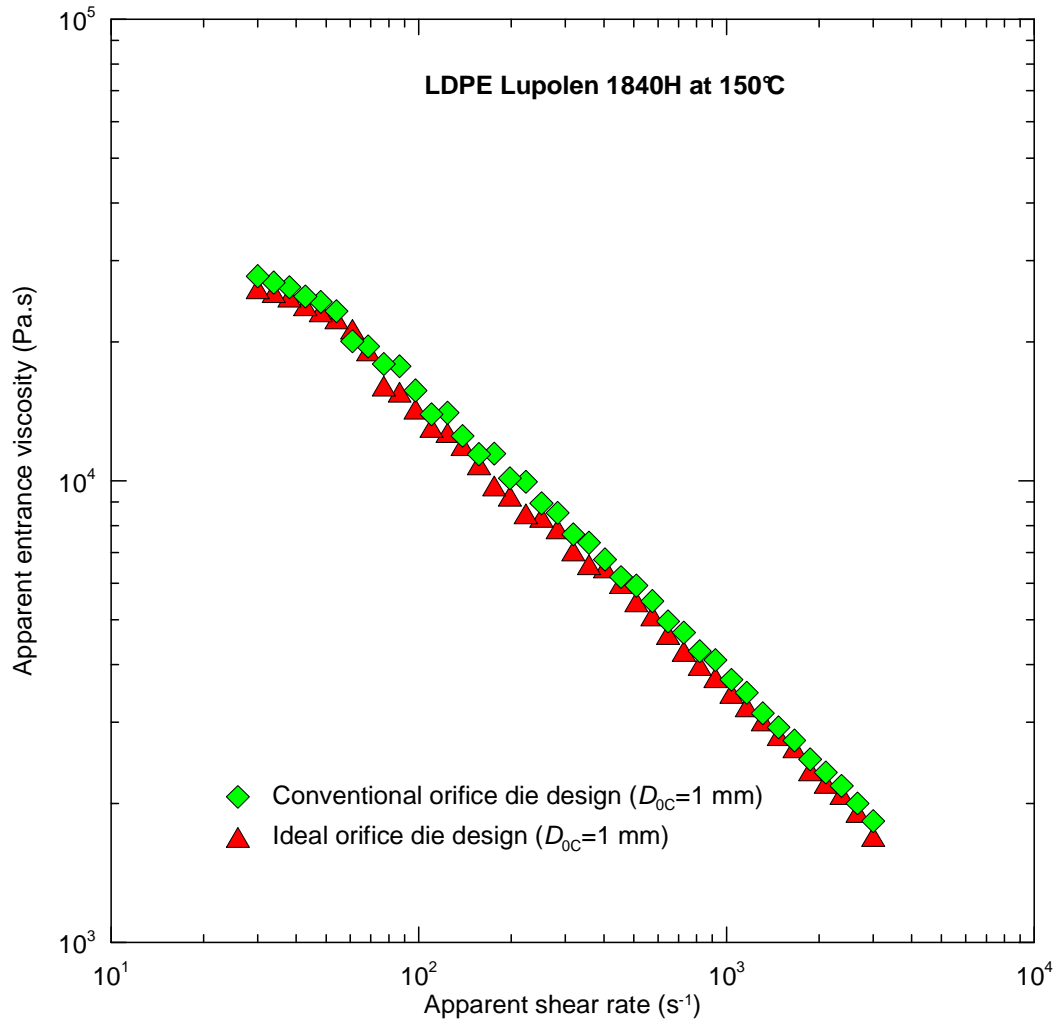


Fig. 65: Comparison between experimentally determined entrance viscosities by using conventional orifice die (green symbols) and novel orifice die (red symbols) for LDPE Lupolen 1840H at 150°C

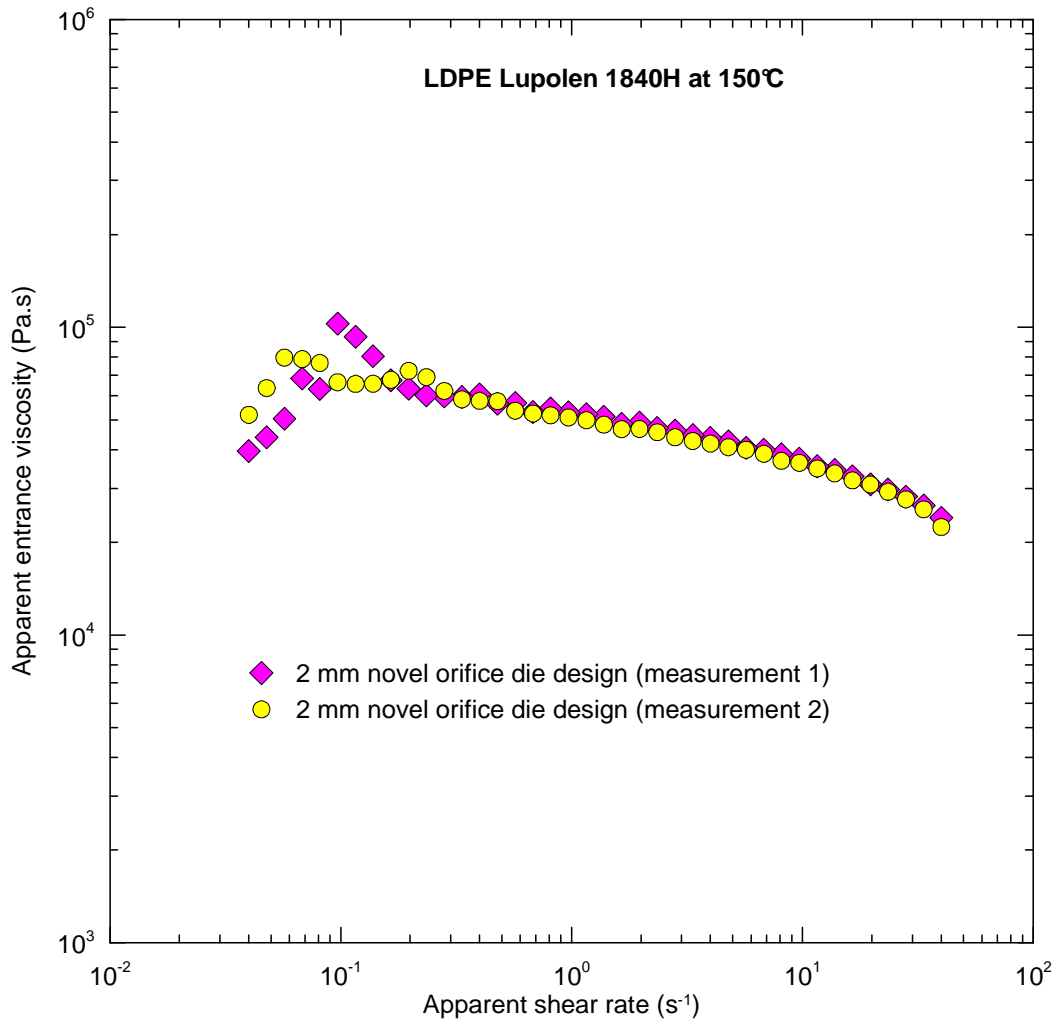


Fig. 66: Comparison of two independent measurements of entrance viscosity for LDPE Lupolen 1840H at 150°C by using novel orifice die having diameter equal to 2mm

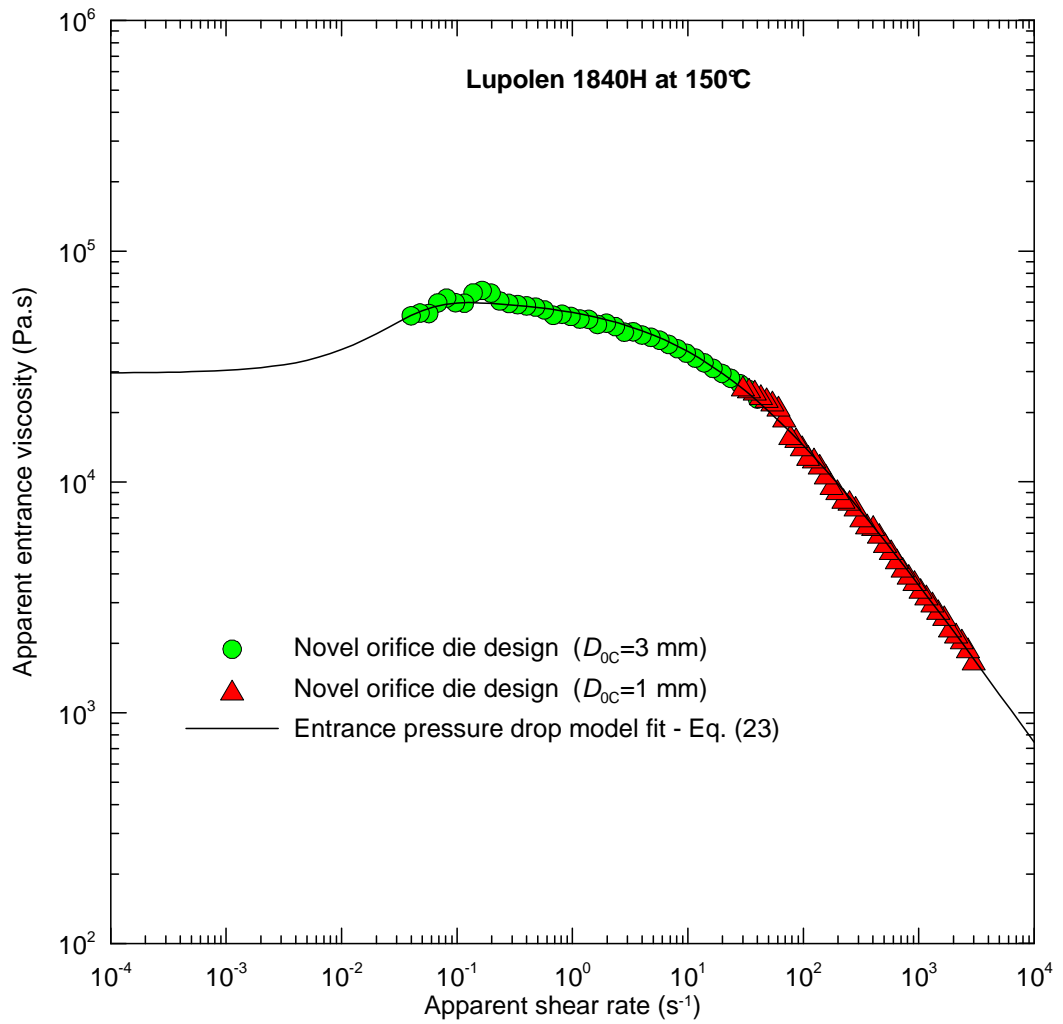


Fig. 67: Comparison of entrance viscosity measurement for LDPE Lupolen 1840H at $150^\circ C$ by using novel orifice die having diameters equal to 1mm and 3mm

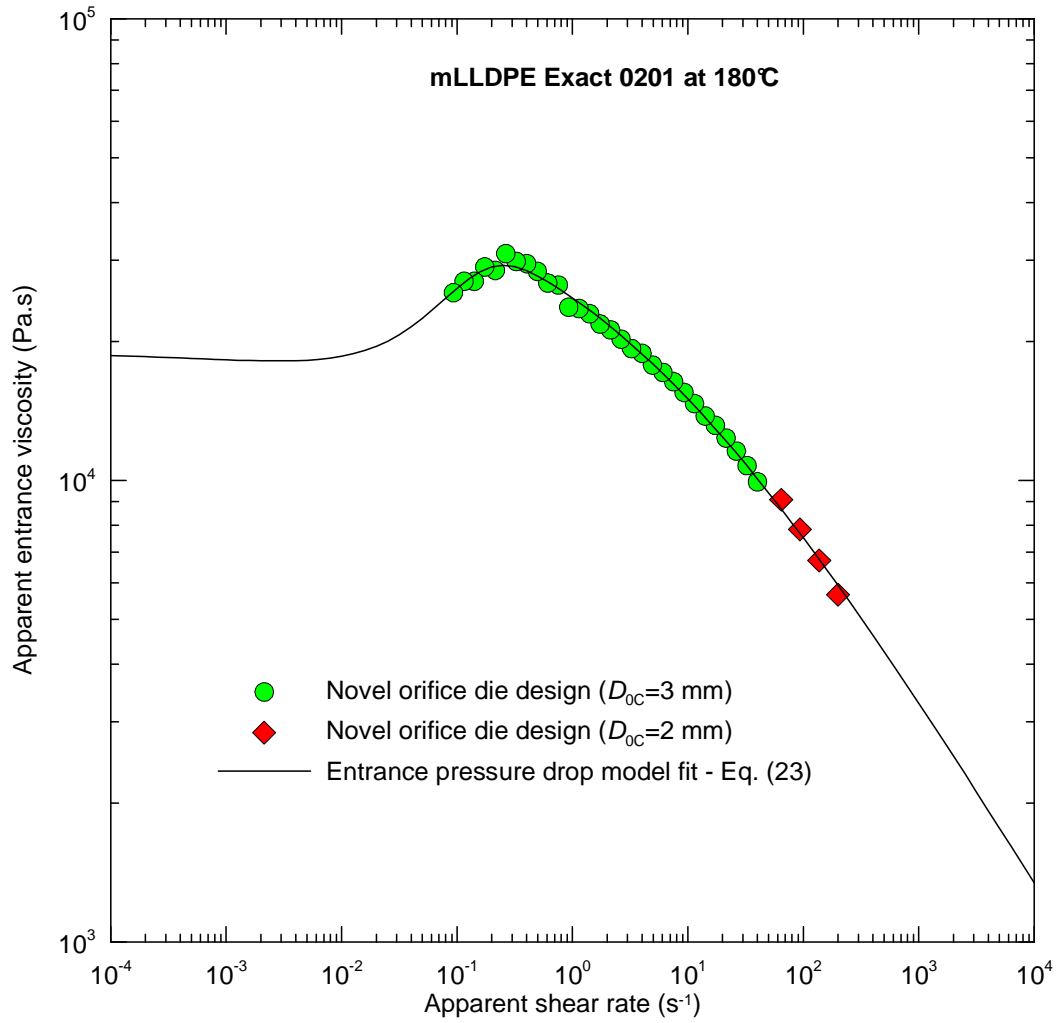


Fig. 68: Entrance viscosity for mLLDPE Exact 0201 material at 180°C measured by novel orifice die with 2mm and 3mm diameter

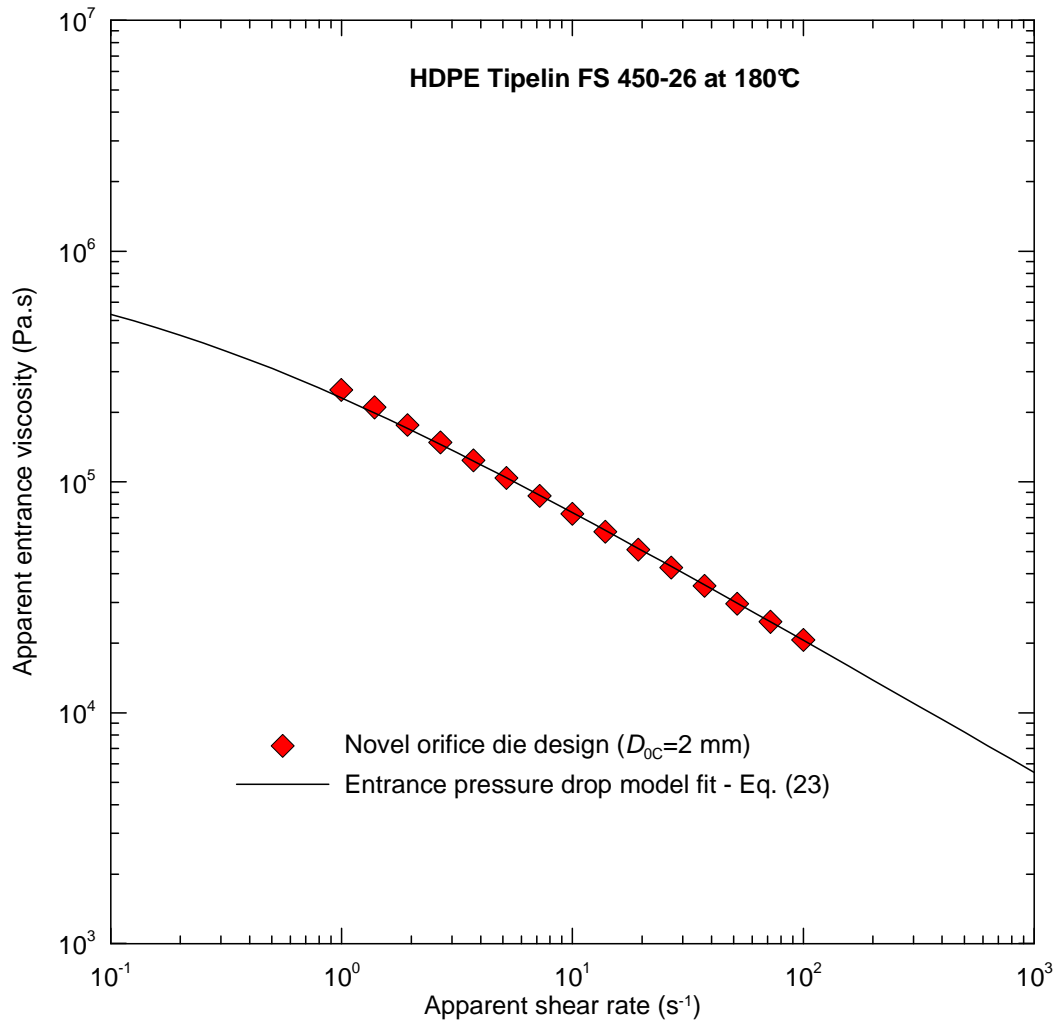


Fig. 69: Entrance viscosity for HDPE Tipelin FS 450-26 material at 180°C measured by novel orifice die with 2mm diameter

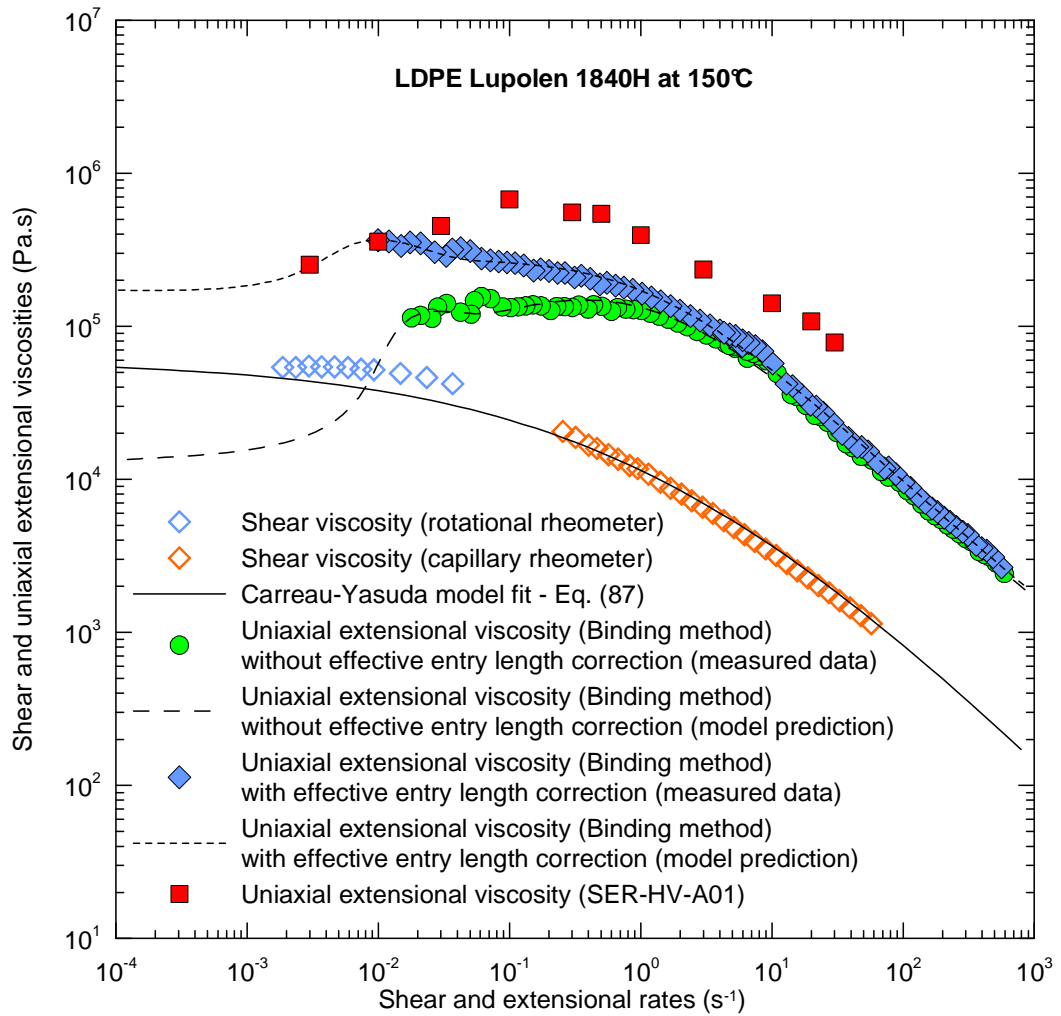


Fig. 70: Comparison between uncorrected/corrected Binding extensional viscosity data and SER measurements for LDPE Lupolen 1840H at 150°C. Shear viscosity data obtained from rotational and capillary rheometer are also provided in this Figure

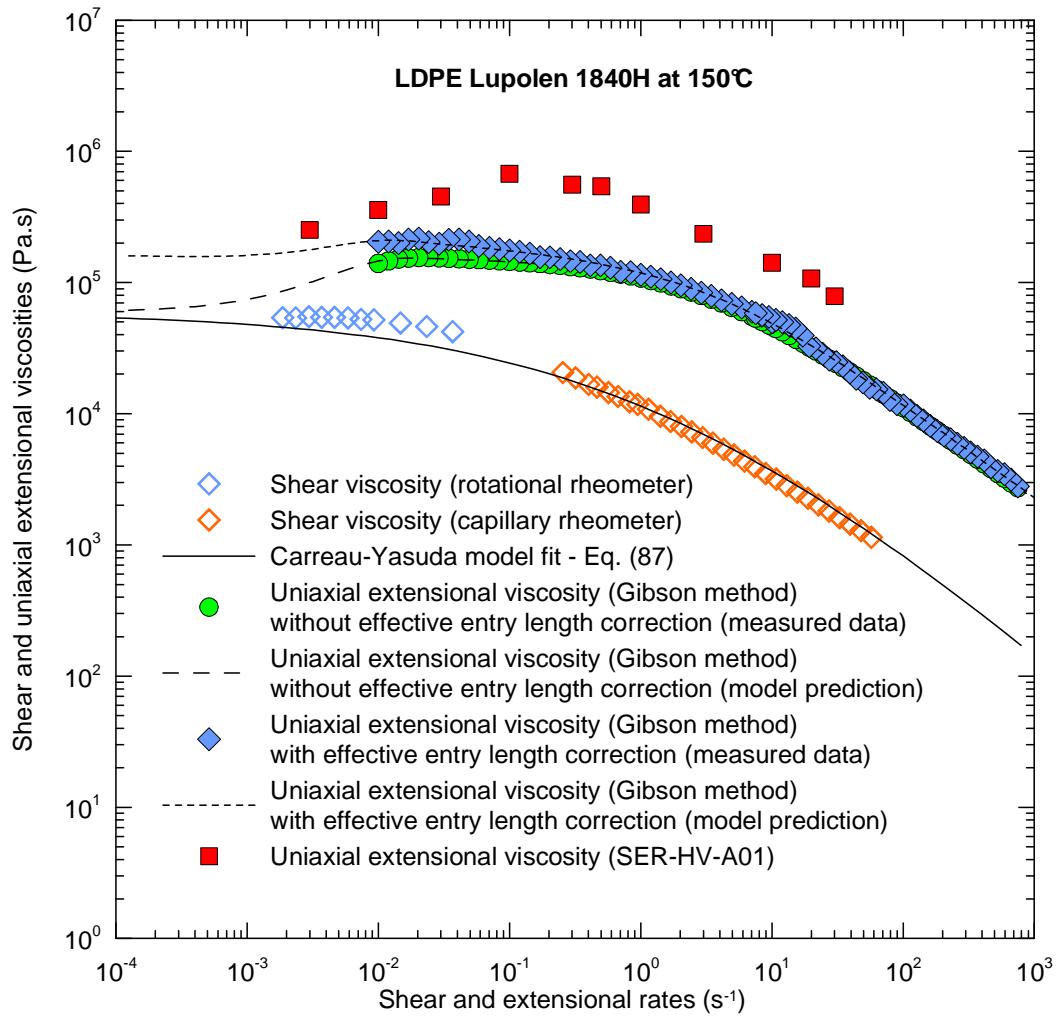


Fig. 71: Comparison between uncorrected/corrected Gibson extensional viscosity data and SER measurements for LDPE Lupolen 1840H at 150°C. Shear viscosity data obtained from rotational and capillary rheometer are also provided in this Figure

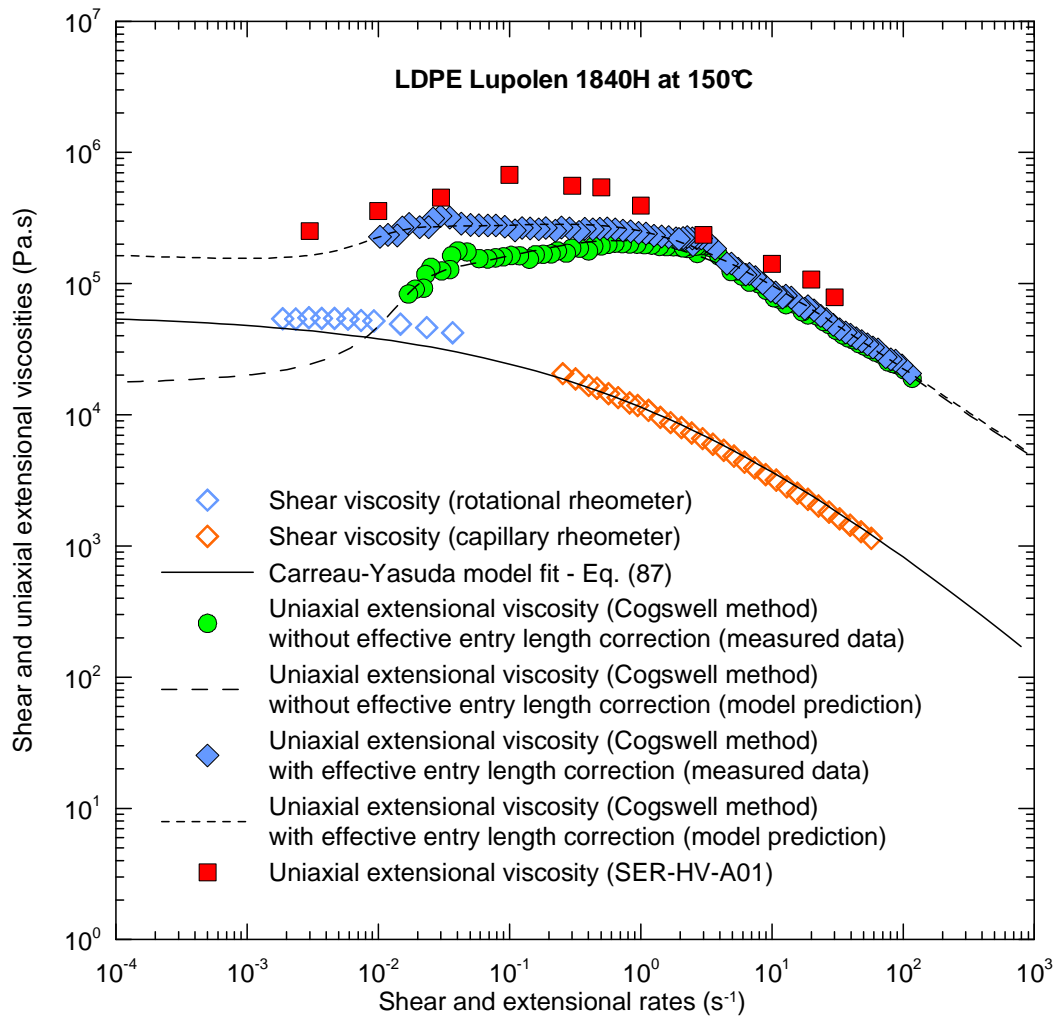


Fig. 72: Comparison between uncorrected/corrected Cogswell extensional viscosity data and SER measurements for LDPE Lupolen 1840H at 150°C. Shear viscosity data obtained from rotational and capillary rheometer are also provided in this Figure

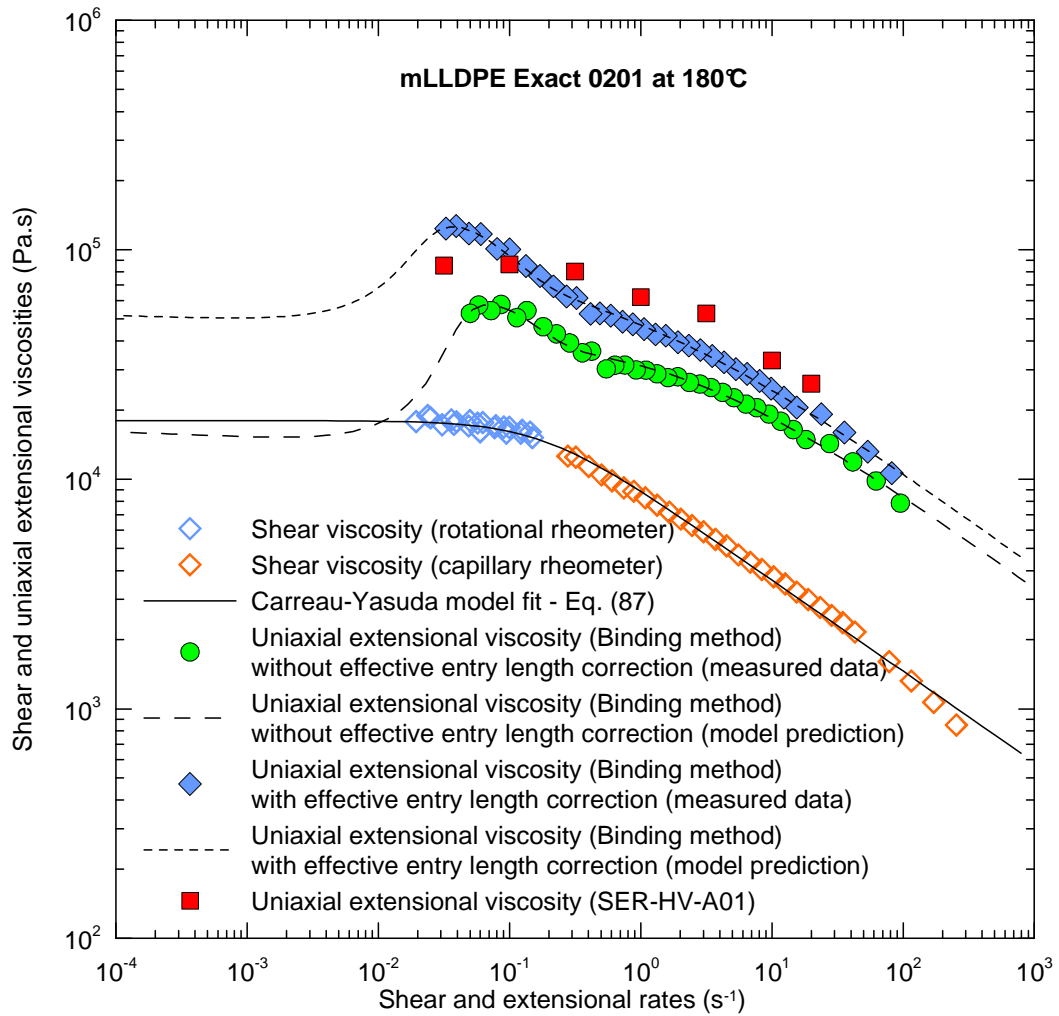


Fig. 73: Comparison between uncorrected/corrected Binding extensional viscosity data and SER measurements for mLLDPE Exact 0201 at 180°C. Shear viscosity data obtained from rotational and capillary rheometer are also provided in this Figure

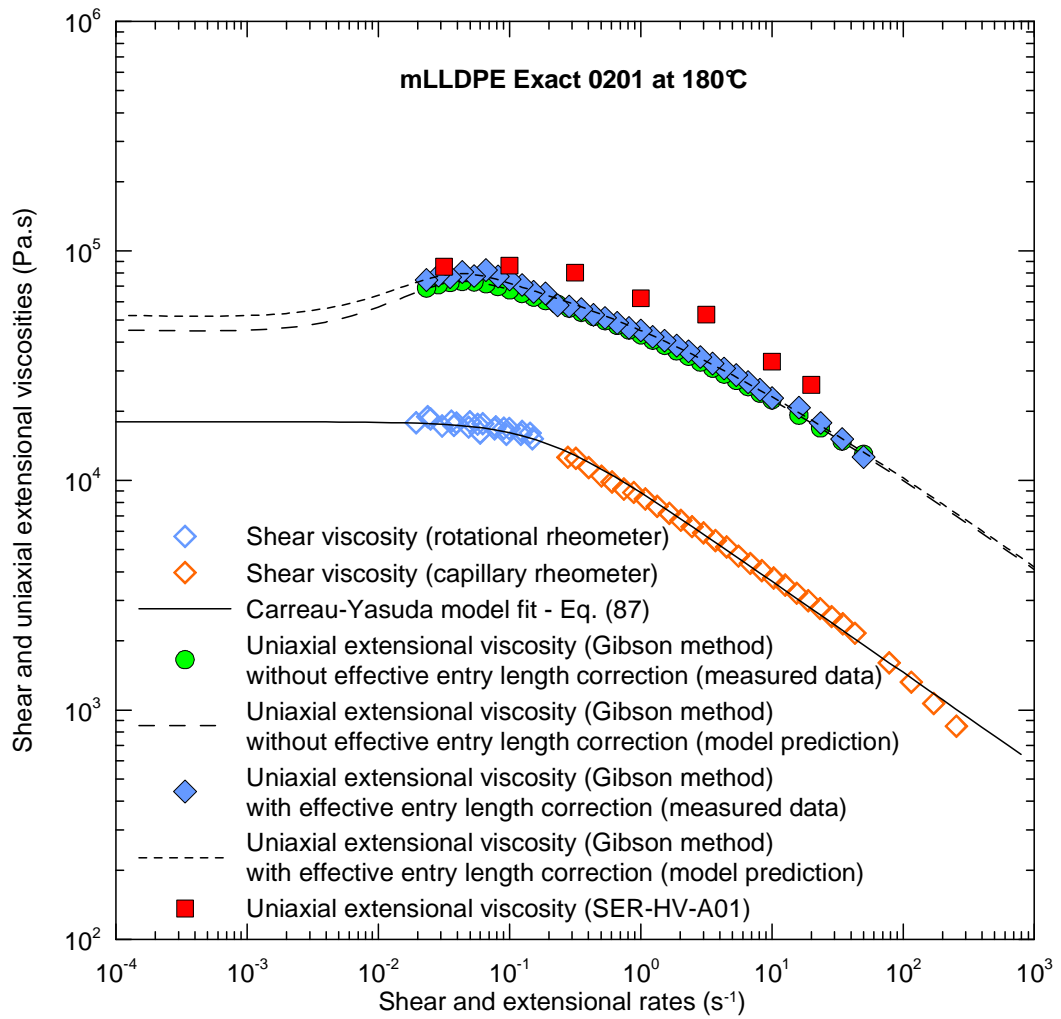


Fig. 74: Comparison between uncorrected/corrected Gibson extensional viscosity data and SER measurements for mLLDPE Exact 0201 at 180°C. Shear viscosity data obtained from rotational and capillary rheometer are also provided in this Figure

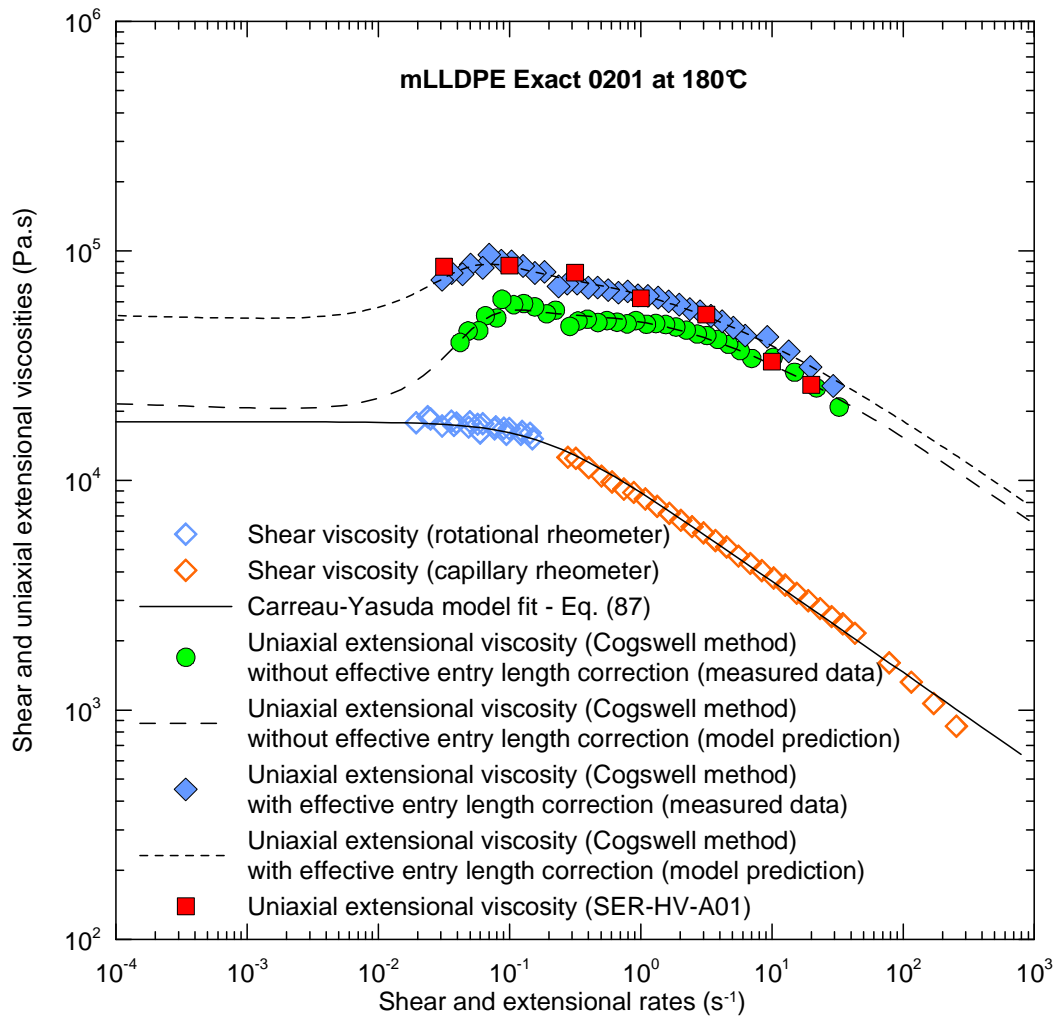


Fig. 75: Comparison between uncorrected/corrected Cogswell extensional viscosity data and SER measurements for mLLDPE Exact 0201 at 180°C. Shear viscosity data obtained from rotational and capillary rheometer are also provided in this Figure

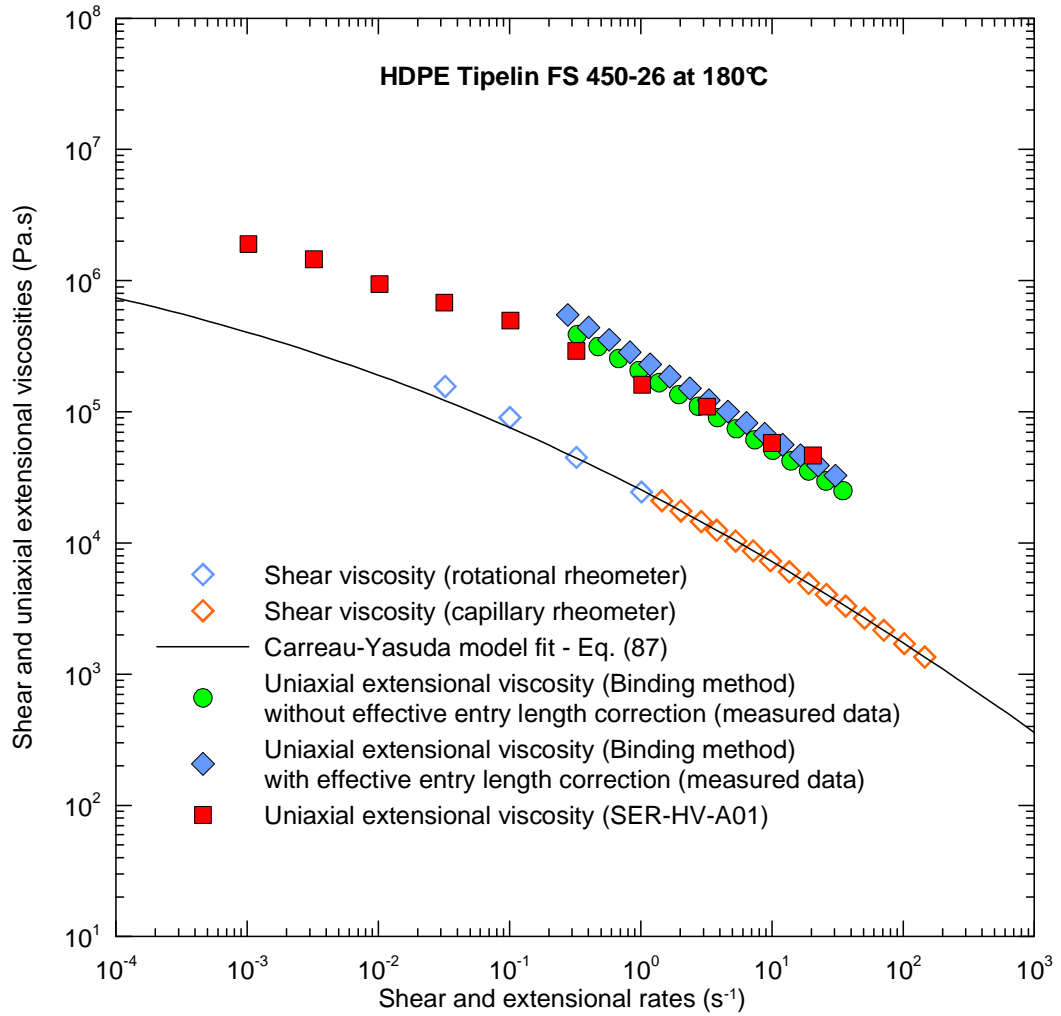


Fig. 76: Comparison between uncorrected/corrected Binding extensional viscosity data and SER measurements for HDPE Tipelin FS 450-26 material at 180°C. Shear viscosity data obtained from rotational and capillary rheometer are also provided in this Figure

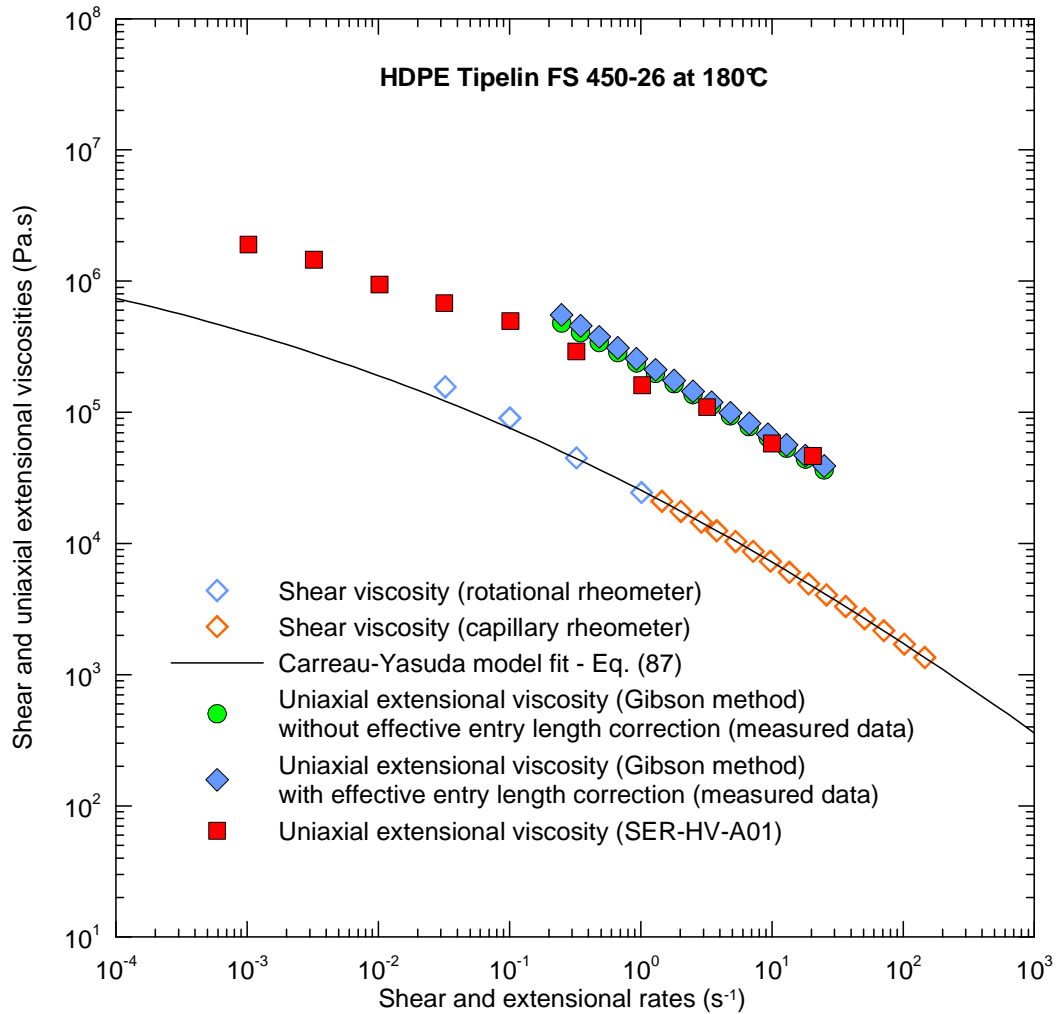


Fig. 77: Comparison between uncorrected/corrected Gibson extensional viscosity data and SER measurements for HDPE Tipelin FS 450-26 material at 180°C. Shear viscosity data obtained from rotational and capillary rheometer are also provided in this Figure

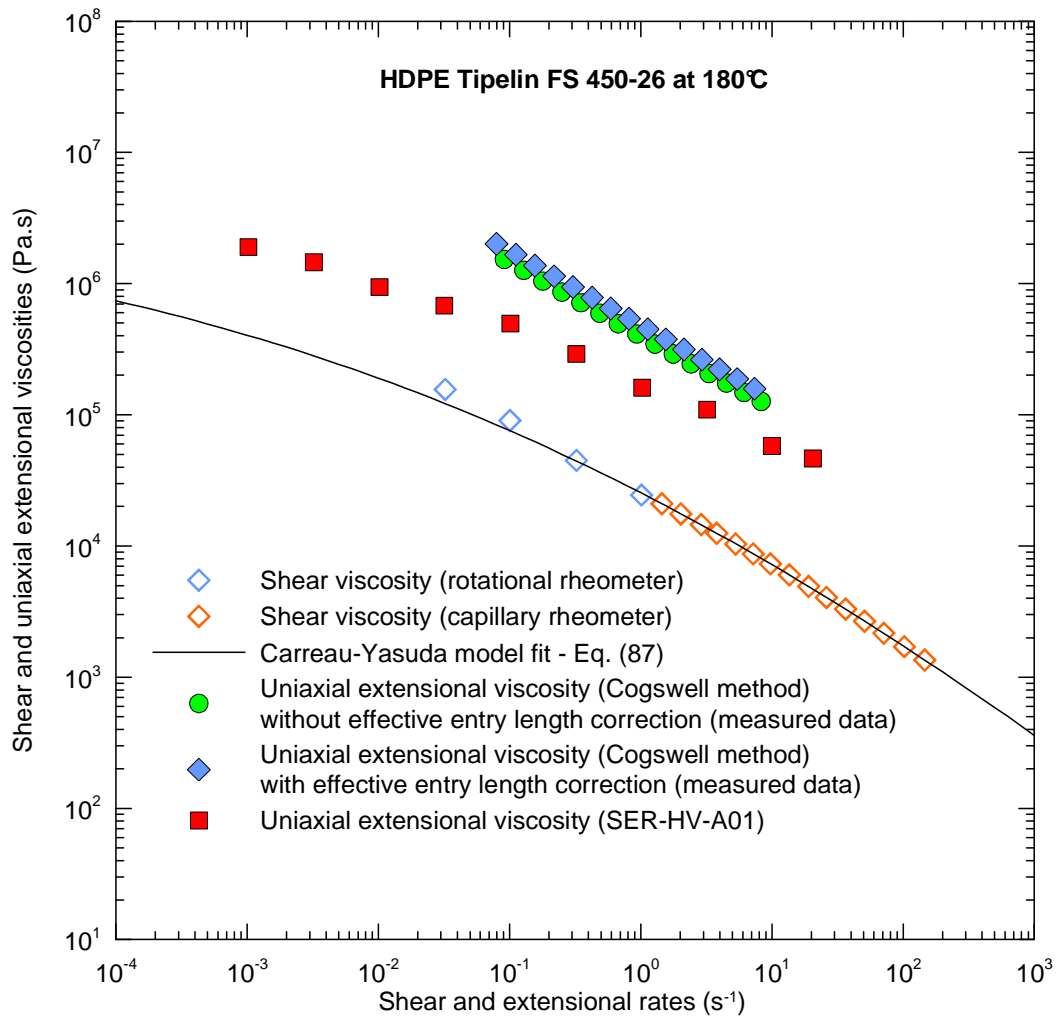


Fig. 78: Comparison between uncorrected/corrected Cogswell extensional viscosity data and SER measurements for HDPE Tipelin FS 450-26 material at 180°C. Shear viscosity data obtained from rotational and capillary rheometer are also provided in this Figure

CONCLUSION

“FINIS CORONAT OPUS.”

(The conclusion crowns the work)

Unknown author,

Common latin quotation.

1. Novel orifice die design has been proposed and tested for the entrance pressure drop measurements. It has been theoretically and experimentally demonstrated that the novel orifice die design allows much precise entrance pressure drop measurement (and thus much precise extensional viscosity determination) in comparison with standard and conventional orifice die.
2. New experimental methodology has been developed for the pressure transducer calibration taking its down resolution limit nonlinearities properly into account.
3. It has been theoretically found that uniaxial extensional viscosity and entrance viscosity are in exponential relationship.
4. Based on theoretical and experimental analysis, it has been revealed that by using novel orifice die design corrected Cogswell model is much precise in uniaxial extensional viscosity prediction than Binding and Cogswell model for highly branched and slightly branched polymer melts. In more detail, it has been demonstrated that corrected Cogswell model provides excellent capability correctly calculate extensional viscosity, especially, if the extensional strain hardening level given by $\eta_{E_{max}}/(3\eta_0)$ ratio is lower than 2. On the other hand, for linear polymer melts, the situation has been found to be opposite, i.e. that Binding and Gibson models were found to provide excellent capability to predict extensional viscosity data from the entrance pressure drop measurements whereas the Cogswell model extensional viscosity predictions were found to be poor (predicted extensional viscosity data were always lower in comparison with SER measurements).

REFERENCES

- [1] BINGHAM, E. C.: *Editorial*, J. Rheol., **1**, 93-95 (1929).
- [2] STEFFE, J. F.: *Rheological methods in food process engineering (second edition)*. East Lansing, United States of America: Freeman press, 1996, 418 p., ISBN 0-9632036-1-4.
- [3] TRACTON, A. A.: *Coating technology handbook (third edition)*. Boca Raton, United States of America: CRC Press, 2006, 912 p., ISBN 1-57444-649-5.
- [4] LIN, H. W., CHANG, C. P., HWU, W. H.: *The rheological behaviors of screen-printing pastes*. J. Mat. Proc. Tec. **197**, 284-291 (2008).
- [5] AGASSANT, J. F, AVENAS, P., SERGENT, J. P., CARREAU, P. J.: *Polymer processing: principles and modeling*. München, Germany: Hauser Publishers, 1991, 475 p., ISBN 3-446-14584-2.
- [6] HATZIKIRIAKOS, S. V., MIGLER, K. B.: *Polymer processing instabilities: Control and Understanding*. New York, United States of America: Marcel Dekker, 2005, 470 p., ISBN 0-8247-5386-0.
- [7] ZATLOUKAL, M., KOPYTKO, W., LENGÁLOVÁ, A., VLČEK, J.: *Theoretical and experimental analysis of interfacial instabilities in coextrusion flows*, **98**, 153-162 (2005).
- [8] MÜNSTEDT, H.: *New universal extensional rheometer for polymer melts*, J. Rheol., **23**, 421-436 (1979).
- [9] HACHMANN, P., MEISSNER, J.: *Rheometer for equibiaxial and planar elongations of polymer melts*, J. Rheol., **47(4)**, 989-1010 (2003).
- [10] SENTMANAT, M. L.: *Miniature universal testing platform: from extensional melt rheology to solid-state deformation behaviour*, Rheol. Acta, **43**, 657-669 (2004).
- [11] PHAN-THIEN, N., TANNER, R. I.: *A new constitutive equation derived from network theory*, J. Non-Newtonian Fluids Mech., **2**, 353-365 (1977).
- [12] VERBEETEN, W. M. H., PETERS, G. W. M., BAAIJENS, F. P. T.: *Differential constitutive equations for polymer melts: eXtended Pom-Pom model*, J. Rheol., **45**, 823-843 (2001).

- [13] BARNES, H. A., ROBERTS, G. P.: *A simple empirical model describing the steady-state shear and extensional viscosities of polymer melts*, J. Non-Newtonian Fluid Mech., **44**, 113-126 (1992).
- [14] KIM, S., DEALY, J. M.: *Design of an orifice die to measure entrance pressure drop*, J. Rheol., **45(6)**, 1413-1419 (2001).
- [15] SENTMANAT, M. L., WANG, B. N., MCKINLEY, G. H.: *Measuring the transient extensional viscosity of polyethylene melts using the SER universal testing platform*, J. Rheol., **49(3)**, 585-606 (2005).
- [16] BIRD, R. B., ARMSTRONG, R. C., HASSAGER, O.: *Dynamics of Polymer Liquids (volume 1: Fluid Mechanics)*. New York, United States of America: John Wiley & Sons, 1987, 649 p., ISBN 0-471-80245-X.
- [17] TADMOR, Z., GOGOS, C. G.: *Principles of Polymer Processing (second edition)*. New Jersey, United States of America: John Willey & Sons, 2006, 961 p., ISBN 0-471-38770-3.
- [18] WHITE, J. L., POTENTE, H.: *Screw extrusion*. Munich, Germany: Hanser Publishers, 2003, 444 p., ISBN 3-446-19624-2.
- [19] MORRISON, F. A.: *Understanding rheology*. New York, United States of America: Oxford University Press, Inc., 2001, 545p., ISBN 0-19-514166-0.
- [20] MACOSCO, C. W.: *Rheology: Principles, Measurements, and Applications*. New York, United States of America: John Willey & Sons, 1993, 550 p., ISBN 0-417-18575-2.
- [21] SENTMANAT M. L., MULIAWAN, E., HATZIKIRIAKOS, S. G.: *Melt fracture of polyethylene and the role of extensional flow behavior*. Available at WWW: <http://www.xpansioninstruments.com/images/SER_2005_SPE-Online.pdf>
- [22] KOLAŘÍK, R.: *Modeling of film blowing process by using variational principles*. Bachelor thesis, Tomas Bata University in Zlín, 2006, 74 p.
- [23] HAGEN, G. H. L.: *Über die Bewegung des in engen zylindrischen Rohren*, Pogg. Ann. Phy. Chem., **46**, 423-442 (1839).

- [24] POISEUILLE, J. L. M.: *Recherches experimentales sur le mouvement des liquides dans les tubes de tres petits diametres*, Crit. Rev. Acad. Sci. Paris, **11**, 961-967, (1840).
- [25] RABINOWITSCH, B.: *Über die Viskosität und Elastiziät von Solen*, Phys. Chem., **145**, 1-26 (1929).
- [26] MOONEY, M.: *Explicit formulas for slip and fluidity*, Trans. Soc. Rheol., **2**, 210-222 (1931).
- [27] BAGLEY, E. B.: *End corrections in the capillary flows of polyethylene*, J. Appl. Phys., **28**, 624-627 (1957).
- [28] BROADBENT, J. M., KAYE, A., LODGE, A. S., VALE, D. G.: *Possible systematic error in the measurement of normal stress differences in polymer solutions in steady shear flow*, Nature, **217**, 55-56 (1968).
- [29] COGSWELL, F. N.: *Converging flow of polymer melts in extrusion dies*, Polym. Eng. Sci. **12**, 64-73 (1972).
- [30] HAN, C. D.: *On slit and capillary die rheometry*, Trans. Soc. Rheol., **18**, 163-190 (1974).
- [31] BINDING, D. M.: *An approximate analysis for contraction and converging flows*, J. Non-Newtonian Fluid Mech. **27**, 173-189 (1988).
- [32] GIBSON, A. G.: *Die entry flows of reinforced polymers*, Composites, **20**, 57-64 (1989).
- [33] ZATLOUKAL, M., VLČEK, J., TZOGANAKIS, C., SÁHA, P.: *Improvement in techniques for the determination of extensional rheological data from entrance flows: computational and experimental analysis*, J. Non-Newtonian Fluid Mech., **107**, 13-37 (2002).
- [34] REVENU, P., GUILLET, J., CARROT, C., ARSAC, A.: *Validation of Cogswell's convergent flow analysis*, J. App. Polym. Sci., **62**, 1783-1792 (1996).
- [35] MACKAY, M. E., ASTARITA, G.: *Analysis of entry flow to determine elongation flow properties revised*, J. Non-Newtonian Fluid Mech., **70**, 219-235 (1997).

- [36] CARROT, C., GUILLET, J.: *Converging flow analysis, entrance pressure drops, and vortex sizes: measurements and calculated values*, Polym. Eng. Sci., **41**, 2095-2107 (2001).
- [37] LAUN, H. M., SCHUTZ, H.: *Transient elongational viscosities and drawability of polymer melts*, J. Rheol., **33**, 119-175 (1989).
- [38] MCGLASHAN, S. A., MACKAY, M. E.: *Comparison of entry flow techniques for measuring elongation flow properties*, J. Non-Newtonian Fluid Mech., **85**, 213-227 (1999).
- [39] TREMBLAY, B.: *Estimation of the elongational viscosity of polyethylene blends at high deformation rates*, J. Non-Newtonian Fluids Mech., **33**, 137-164 (1989).
- [40] PADMANABHAN, M., MACOSCO, C. W.: *Extensional viscosity from entrance pressure drop measurements*, Rheol. Acta, **36**, 144-151 (1997).
- [41] RAJAGOPALAN, D.: *Computational analysis of techniques to determine extensional viscosity from entrance flows*, Rheol. Acta, **39**, 138-151 (2000).
- [42] WAGNER, M. H., BERNAT, A., SCHULZE, V.: *The rheology of the rheotens test*, J. Rheol., **42**(4), 917-928 (1998).
- [43] HAY, G., MACKAY, M. E., AWATI, K. M., PARK, Y.: *Pressure and temperature effects in slit rheometry*, J. Rheol., **43**(5), 1099-1116 (1999).
- [44] COLLYER, A. A., CLEGG, D. W.: *Rheological Measurement (second edition)*. London, United Kingdom: Chapman & Hall, 1998, 779 p., ISBN 0-412-72030-2.
- [45] BAIRD, D. G.: *First normal stress difference measurements for polymer melts at high shear rates in a slit-die using hole and exit pressure data*, J. Non-Newtonian Fluids Mech., **148**, 13-23 (2008).
- [46] JENSEN, E. A., CHRISTIANSEN, J. deC.: *Measurements of first and second normal stress difference in a polymer melt*, J. Non-Newtonian Fluids Mech., **148**, 41-46 (2008).
- [47] MITSOULIS, E., HATZIKIRIAKOS, S. G., CHRISTODOULOU, K., VLASSOPOULOS, D.: *Sensitivity analysis of the Bagley correction to shear and extensional rheology*, Rheol. Acta, **37**, 438-448 (1998).

- [48] MOLDENAERS, P., VERMANT, J., MEWIS, J.: *Origin of nonlinearities in the Bagley plots of thermotropic copolyesters*, J. Rheol., **40**(2), 203-219 (1996).
- [49] TANNER, R. I.: *Engineering rheology (second edition)*. New York, United States of America: Oxford University Press, 2002, 559 p., ISBN 0-19-856473-2.
- [50] BRITTIN, W. E.: *Liquid rise in a capillary tube*, J. Appl. Phys., **17**, 37-44 (1946).
- [51] MALKIN, A. Y., ISAYEV, A. I.: *Rheology: Concepts, Methods, & Applications*. Toronto, Canada: ChemTec Publishing, 2006, 474 p., ISBN 1-895198-33-X.
- [52] WINTER, H. H.: *Temperature fields in extruder dies with circular, annular, or slit cross-section*, Polym. Eng. Sci., **15**, 84-89 (1975).
- [53] LAUN, H. M.: *Pressure dependent viscosity and dissipative heating in capillary rheometry of polymer melts*, Rheol. Acta, **42**, 295-308 (2003).
- [54] SEDLACEK T., ZATLOUKAL M., FILIP P., BOLDIZAR, A., SAHA, P.: *On the effect of pressure on the shear and elongational viscosities of polymer melts*, Polym. Eng. Sci., **44**, 1328-1337 (2004).
- [55] BINDING, D. M., COUCH, M. A., WALTERS, K.: *The pressure dependence of the shear and elongational properties of polymer melts*, J. Non-Newtonian Fluids Mech., **79**, 137-155 (1998).
- [56] THOMAS, C. P.: *Mechanism of reduction of water mobility by polymers in glass capillary arrays*, Soc. Pet. Eng. J., **16**, 130-136 (1976).
- [57] MICHAELI, W.: *Extrusion dies for plastic and rubber: design and engineering computations (third edition)*. München, Germany: Hanser Publishers, 2003, 362 p., ISBN 3-446-22561-7.
- [58] LEONOV, A. I., PROKUNIN, A. N.: *An improved simple version of a non-linear theory of elasto-viscous polymer media*, Rheol. Acta, **19**, 393-403 (1980).
- [59] BERNSTEIN, B., KEARSLEY, E., ZAPAS, L. J.: *A study of stress relaxation with finite strain*, Trans. Soc. Rheol., **7**, 391-410 (1963).
- [60] KAYE, A.: *Non-Newtonian flow in incompressible fluids, Part I: A general rheological equation of state*, Note No. 134, Cranford, United Kingdom, College of Aeronautics, 1962.

- [61] LARSON, R. G.: *Constitutive equations for polymer melts and solutions*. Boston, United States of America: Butterworth Publisher, 1988, 364 p., ISBN 0-409-90119-9 .
- [62] BARNES, H. A., ROBERTS, G. P.: *A simple empirical model describing the steady-state shear and extensional viscosities of polymer melts*, J. Non-Newtonian Fluids Mech., **44**, 113-126 (1992).
- [63] VLACHOPOULOS, J., WAGNER, J. R.: *The SPE guide on Extrusion technology and troubleshooting*. Brookfield, United states of America : The society of plastics engineers, 2001. 456 p., ISBN 9-780-000-00000-2.
- [64] ZATLOUKAL, M., TZOGANAKIS, C., PERDIKOULIAS, J., SÁHA, P.: *Numerical simulations of polymer flow in flat spiral dies*, Polym. Eng. and Sci., **41**, 1683-1694 (2001).
- [65] PIVOKONSKY, R., ZATLOUKAL, M., FILIP, P.: *On the predictive/fitting capabilities of the advanced differential constitutive equations for branched LDPE melts*, J. Non-Newtonian Fluids Mech., **135**, 58-67 (2006).
- [66] GOTSIS, A. D., ODRIOZOLA, A.: *The relevance of entry flow measurements for the estimation of extensional viscosity of polymer melts*, Rheol. Acta, **37**, 430-437 (1998).
- [67] SCHWETZ, M., MÜNSTEDT, H., HEINDL, M., MERTEN, A.: *Investigations on the temperature dependence of the die entrance flow of various long-chain branched polyethylenes using laser-Doppler velocimetry*, J. Rheol., **46(4)**, 797-815 (2002).
- [68] PIVOKONSKY R., ZATLOUKAL, M., FILIP, P.: *On the predictive/fitting capabilities of the advanced differential constitutive equation for linear polymer melts*, J. Non-Newtonian Fluids Mech., **150**, 56-64 (2008).

LIST OF SYMBOLS

Roman symbols

A	temperature sensitivity parameter	$^{\circ}\text{C}^{-1}$
A_0	cross section area of the capillary die	m^2
a	adjustable Carreau – Yasuda model parameter	1
a'	adjustable entrance viscosity model parameter	1
a_t	temperature – dependent shift factor equation	1
B	baric coefficient of viscosity	Pa^{-1}
b	shearfree flow parameter	0 or 1
b'	Gibson's geometrical parameter of exit geometry of the die convergence	m
C	adjustable parameter in Eq. (97)	1
c	heat capacity	$\text{J.kg}^{-1}.\text{K}^{-1}$
D	adjustable parameter in Eq. (97)	1
D_B	barrel diameter	m
D_C	capillary die diameter	m
$\underline{\underline{D_{ij}}}$	deformation rate tensor	s^{-1}
D_{LC}	long capillary die diameter	m
D_{0C}	orifice capillary die diameter	m
E_A	activation energy	J
e	base of natural logarithm	1
F	force	N
F_S	drawdown force	N
F_x	force in x-direction	N
F_y	force in y-direction	N
g	gravitational acceleration	m.s^{-2}

\vec{g}	gravitational acceleration vector	m.s^{-2}
H	gap between parallel plates	m
H_s	slit die height	m
h_t	heat transfer coefficient	$\text{W.m}^{-1}.\text{K}^{-1}$
I_{nk}	Binding's model function	1
i	first tensor index	1
j	second tensor index	1
k	Binding's model parameter	1
k'	Gibson's model parameter	1
\bar{k}	power – law index for elongational viscosity	1
K_1	generalized Maxwell model constant	s
l_0	distance before deformation	m
l	distance after deformation	m
\bar{l}	index of consistence for elongational viscosity	$\text{Pa.s}^{\bar{k}}$
L	length of spinline	m
L_c	capillary die length	m
L_{LC}	long capillary die length	m
L_{0C}	orifice capillary die length	m
L_0	unsupported length	m
L_v	length of vortex	m
$\left(\frac{L_c}{D_c}\right)_{Tr}$	Correction factor for orifice capillary die	1
$\left(\frac{L_{0C}}{D_{0C}}\right)_a$	ratio of length to diameter at orifice capillary die	1
$\left(\frac{L_{LC}}{D_{LC}}\right)_b$	ratio of length to diameter at long capillary die	1
m	slope in dependence of p_H on τ_w	1

\bar{m}	index of consistence for shear viscosity	$\text{Pa}\cdot\text{s}^{\bar{n}}$
m'	power – law index in dependence of melt tension on extensional rate	1
M_n	number average of molecular weight	$\text{g}\cdot\text{mol}^{-1}$
M_w	weight average of molecular weight	$\text{g}\cdot\text{mol}^{-1}$
n	index of non – Newtonian behaviour	1
n'	adjustable entrance viscosity parameter	1
\bar{n}	power – law index for shear viscosity	1
N_1	first normal stress difference	Pa
N_2	second normal stress difference	Pa
$P(V)$	extra function	1
p	pressure	Pa
p_F	flush transducer pressure	Pa
p_H	hole pressure	Pa
p_K	kinetic flow energy induces pressure drop	Pa
p_R	recessed transducer pressure	Pa
p_{REF}	pressure on reference calibration device	Pa
p_{TRANS}	pressure on calibrated transducer	Pa
Q	volumetric flow rate	$\text{m}^3\cdot\text{s}^{-1}$
Q_{SLIP}	slip component of volumetric flow rate	$\text{m}^3\cdot\text{s}^{-1}$
Q_{NOSLIP}	no – slip component of volumetric flow rate	$\text{m}^3\cdot\text{s}^{-1}$
\bar{q}	heat flux	$\text{J}\cdot\text{m}^{-2}\cdot\text{s}^{-1}$
r	radial coordinate in cylindrical and spherical coordinate system	1
r_0	Gibson's geometrical parameter of die entry region	m
r_1	Gibson's geometrical parameter of die entry region	m
R_B	barrel radius	m

R_C	capillary die radius	m
R_G	universal gas constant	$\text{J}\cdot\text{mol}^{-1}\cdot\text{K}^{-1}$
R_{LC}	long capillary die radius	m
R_{0C}	orifice capillary die radius	m
R_V	vortex diameter	m
t	time	s
t'	Binding's model parameter	1
T	temperature	$^{\circ}\text{C}$
T_0	reference temperature	$^{\circ}\text{C}$
\bar{T}	increased temperature due to dissipation energy	$^{\circ}\text{C}$
\bar{T}_0	reference temperature	$^{\circ}\text{C}$
T_q	torque	N.m
U	internal energy	J
V	draw ratio	1
V_P	critical draw ratio	1
V_S	starting point of the drawdown	1
\bar{v}	average velocity in capillary die	$\text{m}\cdot\text{s}^{-1}$
v_D	drawdown velocity	$\text{m}\cdot\text{s}^{-1}$
v_E	exit velocity	$\text{m}\cdot\text{s}^{-1}$
v_M	velocity of moving plate	$\text{m}\cdot\text{s}^{-1}$
v_{SLIP}	slip velocity	$\text{m}\cdot\text{s}^{-1}$
\vec{v}	velocity vector	$\text{m}\cdot\text{s}^{-1}$
v_x	velocity in x-direction	$\text{m}\cdot\text{s}^{-1}$
v_y	velocity in y-direction	$\text{m}\cdot\text{s}^{-1}$
v_z	velocity in z-direction	$\text{m}\cdot\text{s}^{-1}$

W	width of parallel plates	m
W_s	slit die width	m
x	x-coordinate in Cartesian coordinate system	1
y	y-coordinate in Cartesian coordinate system	1
z	z-coordinate in Cartesian, cylindrical and spherical coordinate systems	1

Greek symbols

α	kinetic correction coefficient	s^2
α'	adjustable entrance viscosity model parameter	1
β	angle of exit geometry of the convergence in Gibson's model	$^\circ$
β'	adjustable entrance viscosity model parameter	1
γ	shear strain	1
$\dot{\gamma}$	shear rate	s^{-1}
$\dot{\gamma}_{APP}$	apparent shear rate	s^{-1}
$\dot{\gamma}_{APP-SC}$	apparent shear rate – slip corrected	s^{-1}
$\dot{\gamma}_{COR}$	corrected shear rate	s^{-1}
$\dot{\gamma}_{TRUE}$	no – slip component of apparent shear rate	s^{-1}
Δ	difference	1
Δp	total pressure drop	Pa
$\overline{\Delta p}$	Hagenbach corrected total pressure drop	Pa
Δp_{CAP}	capillary pressure drop	Pa
Δp_{END}	end pressure drop	Pa
Δp_{ENT}	entrance pressure drop	Pa
Δp_{EXIT}	exit pressure drop	Pa
ε	extensional strain	1

$\dot{\epsilon}$	extensional rate	s^{-1}
$\dot{\epsilon}_{xx}$	extensional rate in x-direction	s^{-1}
$\dot{\epsilon}_{yy}$	extensional rate in y-direction	s^{-1}
$\dot{\epsilon}_{zz}$	extensional rate in z-direction	s^{-1}
ζ	Binding's model parameter	1
η	shear viscosity	Pa.s
η_0	zero – shear – rate (Newtonian) viscosity	Pa.s
$\eta(I_D)$	deformation rate – dependent viscosity	Pa.s
η_{APP}	apparent shear viscosity	Pa.s
η_E	extensional viscosity	Pa.s
$\eta_{E_{max}}$	maximum value of uniaxial extensional viscosity	Pa.s
η_{ENT}	entrance viscosity	Pa.s
$\eta_{ENT_{max}}$	maximum value of entrance viscosity	Pa.s
$\overline{\eta}_{ENT}$	entrance viscosity on shear flow component at the entry region	Pa.s
$\eta_{ENT,0}$	plateau – value of entrance viscosity in entrance viscosity model	Pa.s
$\eta_{ENT,0,e}$	entrance viscosity plateau for Binding, Cogswell and Gibson models	Pa.s
$\eta_{ENT,a}$	entrance viscosity measured on the orifice capillary die	Pa.s
$\eta_{ENT,a,0}$	entrance viscosity plateau measured on an orifice capillary die	Pa.s
$\eta_{ENT,C}$	corrected entrance viscosity	Pa.s
η_{P_0}	shear viscosity at atmospheric pressure	Pa.s
η_{T_0}	shear viscosity at reference temperature	Pa.s
θ	angle coordinate in cylindrical and spherical coordinate system	1
κ	capillary die entrance angle	°
λ	relaxation time	s
λ'	adjustable entrance viscosity model parameter	s

λ_0	generalized Maxwell model constant	s
$\bar{\lambda}(II_D)$	deformation rate – dependent relaxation time	s
ξ'	adjustable entrance viscosity model parameter	1
π	Ludolf's number	1
ρ	density	kg.m ⁻³
ρ_M	melt density	kg.m ⁻³
ρ_S	solid density	kg.m ⁻³
σ_E	extensional stress	Pa
σ_P	critical tension	Pa
σ_T	tensile stress	Pa
$\nabla_{\underline{\underline{\tau}}}$	upper convected stress tensor derivate	Pa.s ⁻¹
$\underline{\underline{\tau}}_{ij}$	stress tensor	Pa
τ_{rz}	shear stress in capillary die	Pa
τ_{Rz}	wall shear stress in capillary die	Pa
τ_{RzAPP}	apparent wall shear stress in capillary die	Pa
τ_W	wall shear stress in slit die	Pa
φ	angle coordinate in spherical coordinate system	1
φ_V	vortex angle	°
ψ_1	first normal stress coefficient	Pa.s ²
ψ_2	second normal stress coefficient	Pa.s ²
Ω	drive shaft rotational rate	s ⁻¹

Special symbols

I_D	first invariant of deformation rate tensor	s^{-1}
II_D	second invariant of deformation rate tensor	s^{-1}
III_D	third invariant of deformation rate tensor	s^{-1}
∂	partial derivate	1
∞	far field	1
∇	vector operator “ <i>nabla</i> ”	1

Abbreviations

<i>CE</i>	Constitutive Equation
<i>CVM</i>	Control Volume Method
<i>DSC</i>	Differential Scanning Calorimetry
<i>FAN</i>	Flow Analysis Network
<i>FDM</i>	Finite Difference Method
<i>FEM</i>	Finite Element Method
<i>HDPE</i>	High Density PolyEthylene
<i>K-BKZ</i>	The Kaye-Bernstein-Kearsley-Zapas model
<i>LDPE</i>	Low Density PolyEthylene
<i>mLLDPE</i>	metallocene Linear Low Density PolyEthylene
<i>PID</i>	Proportional – Integrative – Derivative regulator
<i>PSI</i>	Pounds per Square Inch
<i>PTT</i>	Phan-Thien-Tanner model
<i>SER</i>	Sentmanat Extensional Rheometer
<i>VEL</i>	Virtual Extrusion Laboratory
<i>XPP</i>	eXtended Pom-Pom model

LIST OF FIGURES

<i>Fig. 1: Movement of a differential material element</i>	16
<i>Fig. 2: Shear flow definition sketch</i>	18
<i>Fig. 3: Principle of drag shear flow and its velocity profile</i>	20
<i>Fig. 4: Deformation of abutting material layers in drag shear flow</i>	20
<i>Fig. 5: Poiseuille flow into a thin slit and its velocity profile</i>	21
<i>Fig. 6: Deformation of neighbouring material layers in Poiseuille flow</i>	22
<i>Fig. 7: Definition sketch of uniaxial elongational flow</i>	22
<i>Fig. 8: Definition sketch of planar elongational flow</i>	23
<i>Fig. 9: Definition sketch of biaxial elongational flow</i>	23
<i>Fig. 10: Uniaxial elongational flow</i>	25
<i>Fig. 11: Planar elongational flow</i>	26
<i>Fig. 12: Biaxial elongational flow</i>	27
<i>Fig. 13: Development of melt fracture instability with increasing shear rate: (a) smooth surface, (b) sharkskin, (c) gross melt fracture (taken from [21])</i>	29
<i>Fig. 14: Instabilities in film casting process</i>	30
<i>Fig. 15: One spun fibre</i>	31
<i>Fig. 16: Film blowing instabilities</i>	32
<i>Fig. 17: Coextrusion instabilities</i>	33
<i>Fig. 18: Cross section view of runner with detail of deformation element and tear forehead of melt</i>	34
<i>Fig. 19: Transparent section view of barrel part of twin-bore capillary rheometer (controlled-rate mode)</i>	37
<i>Fig. 20: The behaviour of pressure along the capillary</i>	39
<i>Fig. 21: Definition sketch of entry flow</i>	41
<i>Fig. 22: Definition scheme of entry flow in Gibson's analysis</i>	45
<i>Fig. 23: Principle of Haul-off Rheotens measuring technique of extensional viscosity and rupture stress</i>	48
<i>Fig. 24: Differential ring shape element in a capillary and forces acting on it</i>	50
<i>Fig. 25: Real view of slit die</i>	53
<i>Fig. 26: Pressure profile along the slit die (taken from [44])</i>	54

<i>Fig. 27: First normal stress difference versus shear stress for low density polyethylene (taken from [44])</i>	55
<i>Fig. 28: Pressure hole geometry</i>	56
<i>Fig. 29: Most frequently used pressure hole types: (a) transverse to flow, (b) parallel to flow, (c) circular</i>	57
<i>Fig. 30: Shear flow in capillary die with (a) no slip and (b) slip at the wall</i>	58
<i>Fig. 31: Dependence of apparent shear rate on inverse capillary radius at various shear stresses for low density polyethylene (taken from [19])</i>	58
<i>Fig. 32: Schematic view of typical capillary dies set: long capillary (left) and orifice capillary (right)</i>	60
<i>Fig. 33: Linear fit (a) and quadratic fit (b) in Bagley plots (taken from [14])</i>	61
<i>Fig. 34: Volume element of fluid</i>	70
<i>Fig. 35: Components of stress, velocity and gravitational acceleration acting on differential volume of fluid</i>	71
<i>Fig. 36: Comparison of shear and extensional viscosity obtained experimentally (symbols) and through modified White – Metzner model (lines) (taken from [62])</i>	75
<i>Fig. 37: Typical spiral mandrel die geometry (real die on the left side, real model of channels on the top of the right side and FAN grid of channels below it)</i>	78
<i>Fig. 38: Typical Finite difference grid</i>	78
<i>Fig. 39: Typical flat spiral die geometry (real die-left, and FEM grid of distribution system-right) (taken from [64])</i>	80
<i>Fig. 40: Real view of twin-bore capillary rheometer ROSAND RH7-2</i>	85
<i>Fig. 41: Conventional orifice die – section view (a), bottom view (b)</i>	86
<i>Fig. 42: Real view of calibration device in operation state</i>	89
<i>Fig. 43: Schematic view of Sentmanat extensional rheometer (SER)</i>	90
<i>Fig. 44: Details for theoretical ideal orifice die analysis where downstream region is not filled by the polymer melt (a – geometrical sketch of ideal orifice die, b – boundary conditions, c – FEM mesh)</i>	93
<i>Fig. 45: Details for theoretical conventional orifice die analysis where downstream region is not filled by polymer melt (a – geometrical sketch of conventional orifice die, b – boundary conditions, c – FEM mesh)</i>	97
<i>Fig. 46: Novel orifice die – section view (a), bottom view (b)</i>	98

<i>Fig. 47: Single point calibration curve for 500 PSI pressure transducer</i>	<i>103</i>
<i>Fig. 48: Comparison between uncorrected (red circles) and corrected (green, blue and orange symbols) 500 PSI pressure transducer response.....</i>	<i>104</i>
<i>Fig. 49: Single point calibration for 250 PSI pressure transducer</i>	<i>105</i>
<i>Fig. 50: Comparison between uncorrected (red circles) and corrected (green, blue and orange symbols) 250 PSI pressure transducer response.....</i>	<i>106</i>
<i>Fig. 51: Comparison between steady shear and uniaxial extensional viscosity data (symbols) and modified White-Metzner model predictions (lines) for LDPE Escorene LD 165 BW1 at 200 °C. Experimental data are taken from [65]</i>	<i>107</i>
<i>Fig. 52: Steady shear and uniaxial extensional viscosity curves predicted by modified White-Metzner model – Eq. (86) for LDPE Escorene LD 165 BW1 and four additional virtual materials (M1, M2, M3 and M4).....</i>	<i>108</i>
<i>Fig. 53: Apparent entrance viscosity curves determined by viscoelastic FEM calculations for “ideal orifice die” depicted in Fig. 44.....</i>	<i>109</i>
<i>Fig. 54: Comparison of corrected Cogswell, Binding and Gibson predictions of extensional viscosity with modified White-Metzner extensional viscosity for LDPE Escorene LD 165 BW1 assuming “ideal orifice die” depicted in Fig. 44.....</i>	<i>110</i>
<i>Fig. 55: Comparison of corrected Cogswell, Binding and Gibson predictions of extensional viscosity with modified White-Metzner extensional viscosity for virtual material M1 assuming “ideal orifice die” depicted in Fig. 44.....</i>	<i>111</i>
<i>Fig. 56: Comparison of corrected Cogswell, Binding and Gibson predictions of extensional viscosity with modified White-Metzner extensional viscosity for virtual material M2 assuming “ideal orifice die” depicted in Fig. 44.....</i>	<i>112</i>
<i>Fig. 57: Comparison of corrected Cogswell, Binding and Gibson predictions of extensional viscosity with modified White-Metzner extensional viscosity for virtual material M3 assuming “ideal orifice die” depicted in Fig. 44.....</i>	<i>113</i>
<i>Fig. 58: Comparison of corrected Cogswell, Binding and Gibson predictions of extensional viscosity with modified White-Metzner extensional viscosity for virtual material M4 assuming “ideal orifice die” depicted in Fig. 44.....</i>	<i>114</i>
<i>Fig. 59: Theoretically predicted relationship between attainable dimensionless maximum in uniaxial extensional viscosity curve and entrance viscosity curve for “ideal orifice die” depicted in Fig. 44.....</i>	<i>115</i>

<i>Fig. 60: Theoretically predicted effect of orifice die design on the entrance viscosity for virtual material M2</i>	<i>116</i>
<i>Fig. 61: Comparison between modified White-Metzner extensional viscosity and Cogswell predictions for virtual material M2 by using two different orifice dies.....</i>	<i>117</i>
<i>Fig. 62: Comparison between measured steady uniaxial extensional/shear viscosities and modified White-Metzner model predictions.....</i>	<i>118</i>
<i>Fig. 63: Vortex size development predicted by the FEM calculation (using the modified White-Metzner model as the constitutive equation) for LDPE Lupolen 1840H melt flow through “ideal orifice die” (abrupt contraction flow) at 150°C for different mass flow rates.....</i>	<i>119</i>
<i>Fig. 64: Comparison between experimentally determined entrance viscosities by using conventional orifice die (green symbols) and novel orifice die (red symbols) for LDPE Lupolen 1840H at 250°C</i>	<i>120</i>
<i>Fig. 65: Comparison between experimentally determined entrance viscosities by using conventional orifice die (green symbols) and novel orifice die (red symbols) for LDPE Lupolen 1840H at 150°C</i>	<i>121</i>
<i>Fig. 66: Comparison of two independent measurements of entrance viscosity for LDPE Lupolen 1840H at 150°C by using novel orifice die having diameter equal to 2mm</i>	<i>122</i>
<i>Fig. 67: Comparison of entrance viscosity measurement for LDPE Lupolen 1840H at 150°C by using novel orifice die having diameters equal to 1mm and 3mm.....</i>	<i>123</i>
<i>Fig. 68: Entrance viscosity for mLLDPE Exact 0201 material at 180°C measured by novel orifice die with 2mm and 3 mm diameter.....</i>	<i>124</i>
<i>Fig. 69: Entrance viscosity for HDPE Tipelin FS 450-26 material at 180°C measured by novel orifice die with 2mm diameter.....</i>	<i>125</i>
<i>Fig. 70: Comparison between uncorrected/corrected Binding extensional viscosity data and SER measurements for LDPE Lupolen 1840H at 150°C. Shear viscosity data obtained from rotational and capillary rheometer are also provided in this Figure</i>	<i>126</i>

Fig. 71: Comparison between uncorrected/corrected Gibson extensional viscosity data and SER measurements for LDPE Lupolen 1840H at 150°C. Shear viscosity data obtained from rotational and capillary rheometer are also provided in this Figure..... 127

Fig. 72: Comparison between uncorrected/corrected Cogswell extensional viscosity data and SER measurements for LDPE Lupolen 1840H at 150°C. Shear viscosity data obtained from rotational and capillary rheometer are also provided in this Figure 128

Fig. 73: Comparison between uncorrected/corrected Binding extensional viscosity data and SER measurements for mLLDPE Exact 0201 at 180°C. Shear viscosity data obtained from rotational and capillary rheometer are also provided in this Figure 129

Fig. 74: Comparison between uncorrected/corrected Gibson extensional viscosity data and SER measurements for mLLDPE Exact 0201 at 180°C. Shear viscosity data obtained from rotational and capillary rheometer are also provided in this Figure..... 130

Fig. 75: Comparison between uncorrected/corrected Cogswell extensional viscosity data and SER measurements for mLLDPE Exact 0201 at 180°C. Shear viscosity data obtained from rotational and capillary rheometer are also provided in this Figure 131

Fig. 76: Comparison between uncorrected/corrected Binding extensional viscosity data and SER measurements for HDPE Tipelin FS 450-26 material at 180°C. Shear viscosity data obtained from rotational and capillary rheometer are also provided in this Figure..... 132

Fig. 77: Comparison between uncorrected/corrected Gibson extensional viscosity data and SER measurements for HDPE Tipelin FS 450-26 material at 180°C. Shear viscosity data obtained from rotational and capillary rheometer are also provided in this Figure..... 133

Fig. 78: Comparison between uncorrected/corrected Cogswell extensional viscosity data and SER measurements for HDPE Tipelin FS 450-26 material at 180°C. Shear viscosity data obtained from rotational and capillary rheometer are also provided in this Figure..... 134

LIST OF TABLES

<i>Tab. 1: Assumptions of Cogswell's entry flow analysis</i>	<i>42</i>
<i>Tab. 2: Assumptions of Binding's entry flow analysis.....</i>	<i>43</i>
<i>Tab. 3: Assumptions of Gibson's entry flow analysis.....</i>	<i>46</i>
<i>Tab. 4: Assumptions for Poiseuille flow in a capillary die.....</i>	<i>50</i>
<i>Tab. 5: Parameters of modified White-Metzner model (Eqs. (86), (87) and (91)) for both, real (LDPE Escorene LD 165 BW1) and virtual (M1, M2, M3 and M4) materials.....</i>	<i>92</i>
<i>Tab. 6: Entrance pressure drop model (Eq. (23)) parameters for both, real (LDPE Escorene LD 165 BW1) and virtual (M1, M2, M3 and M4) materials.....</i>	<i>94</i>
<i>Tab. 7: Parameters of entrance pressure drop model (Eq. (23)) for virtual material M2 ..</i>	<i>96</i>
<i>Tab. 8: Temperature dependent modified White – Metzner model parameters (Eq. (86), (87), (88) and (91)) for LDPE Lupolen 1840H</i>	<i>99</i>
<i>Tab. 9: Parameters of entrance pressure drop model (Eq. (23)).....</i>	<i>101</i>
<i>Tab. 10: Fitting parameters of Carreau – Yasuda model (Eq. (87)).....</i>	<i>101</i>

APPENDICES

Appendix A I: Extrusion line for pipes

Appendix A II: Extrusion line for thin polymer film

Appendix A III: Production line of fibre spinning

Appendix A IV: Film blowing production line

Appendix A V: Injection moulding process

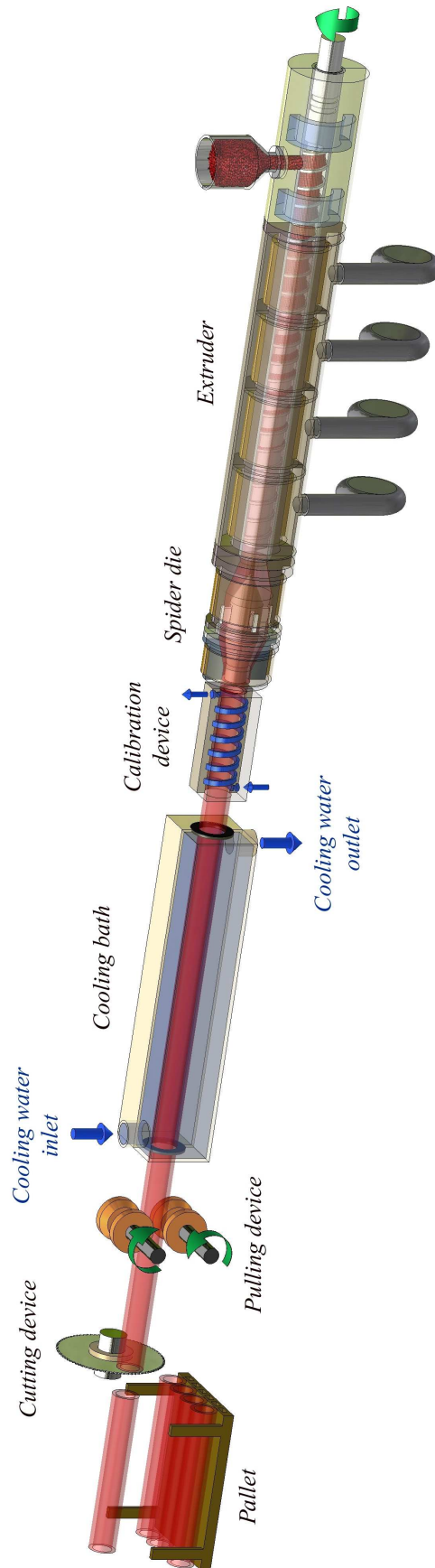
Appendix A VI: Drawings of novel orifice die design

Appendix A VII: DSC analysis of tested materials

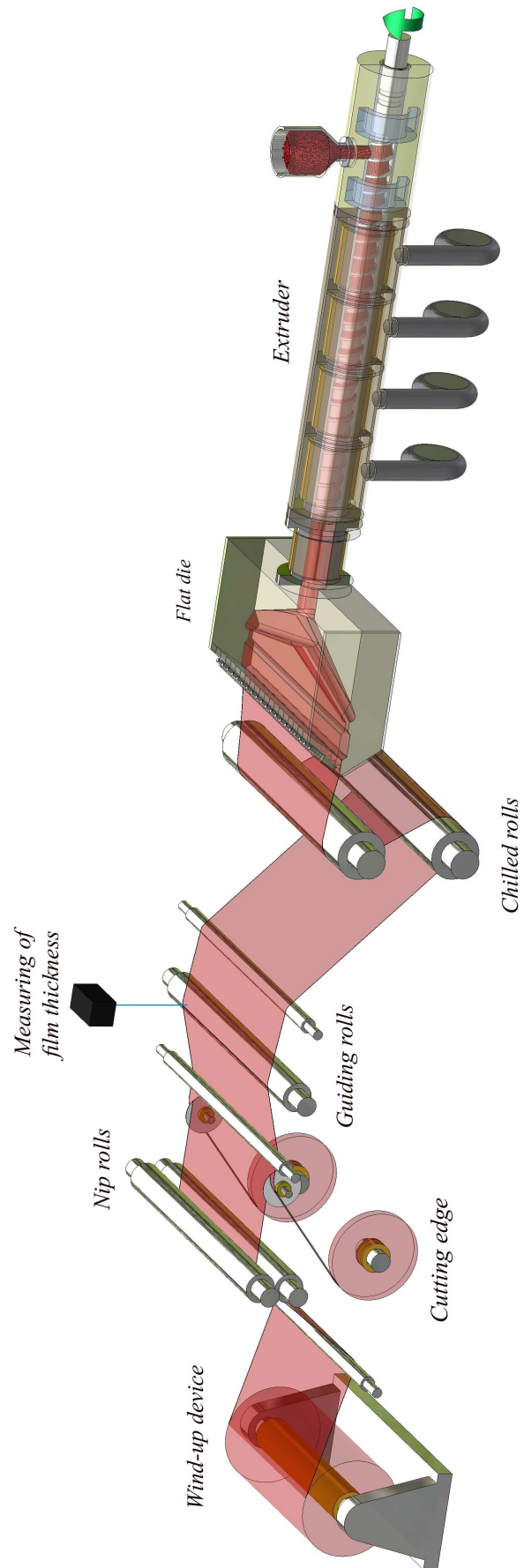
Appendix A VIII: IR spectrum of tested materials

Appendix A IX: CD-ROM

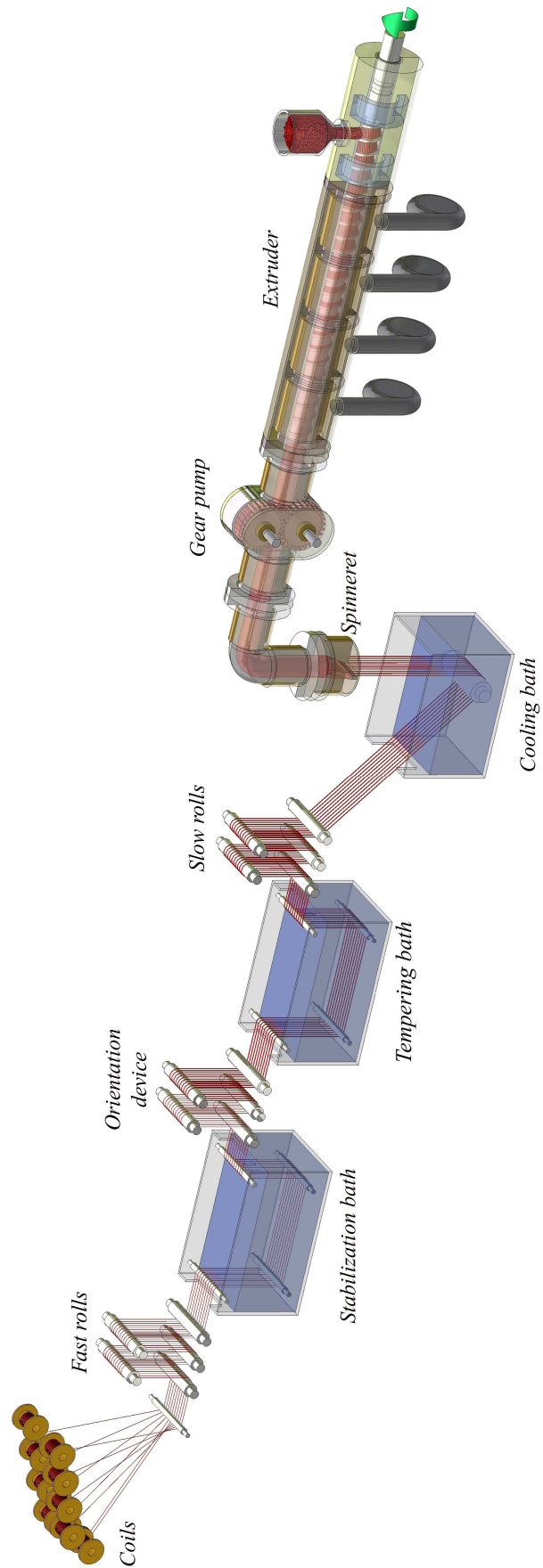
APPENDIX A I: EXTRUSION LINE FOR PIPES



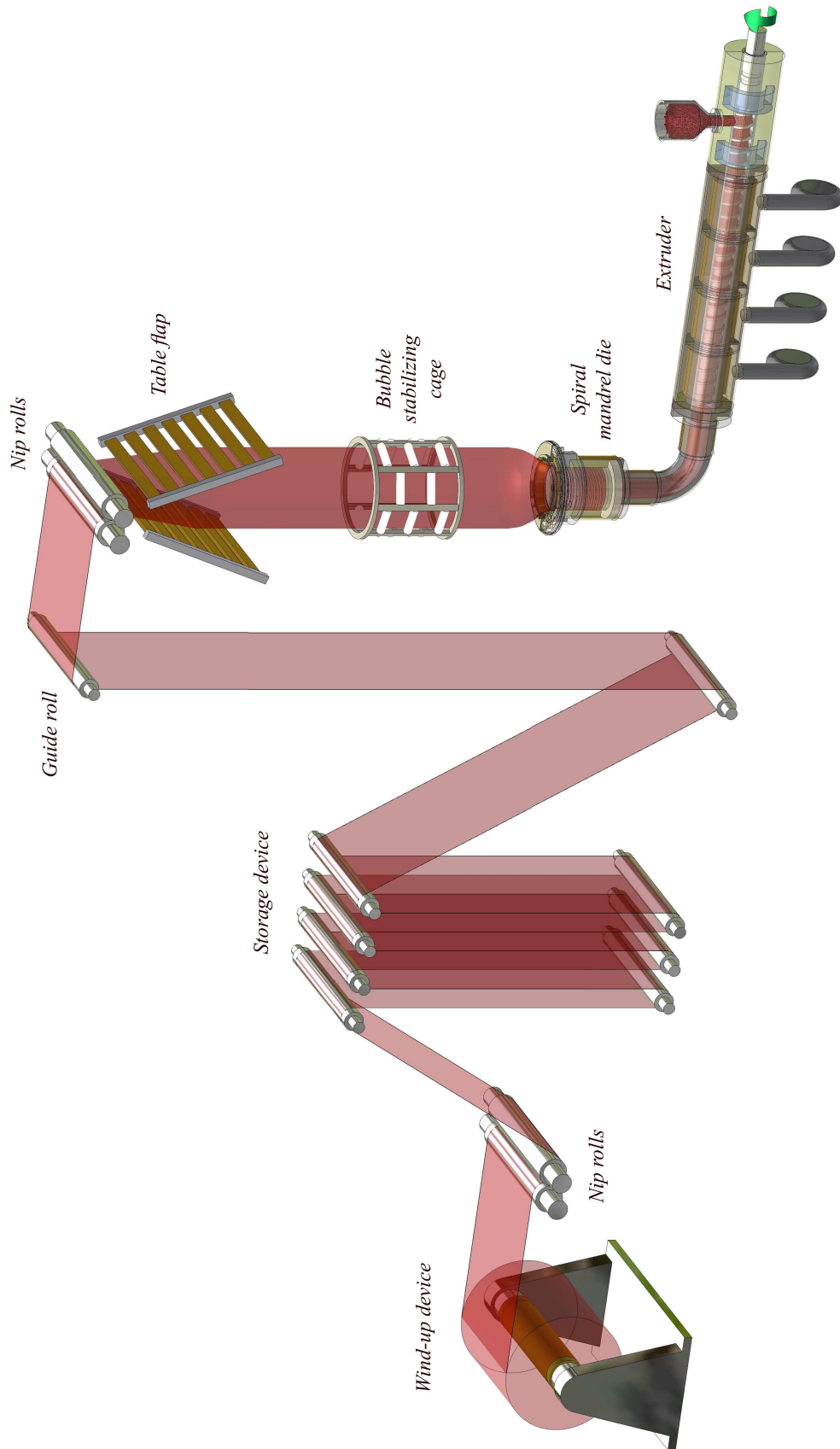
APPENDIX A II: EXTRUSION LINE FOR THIN POLYMER FILMS



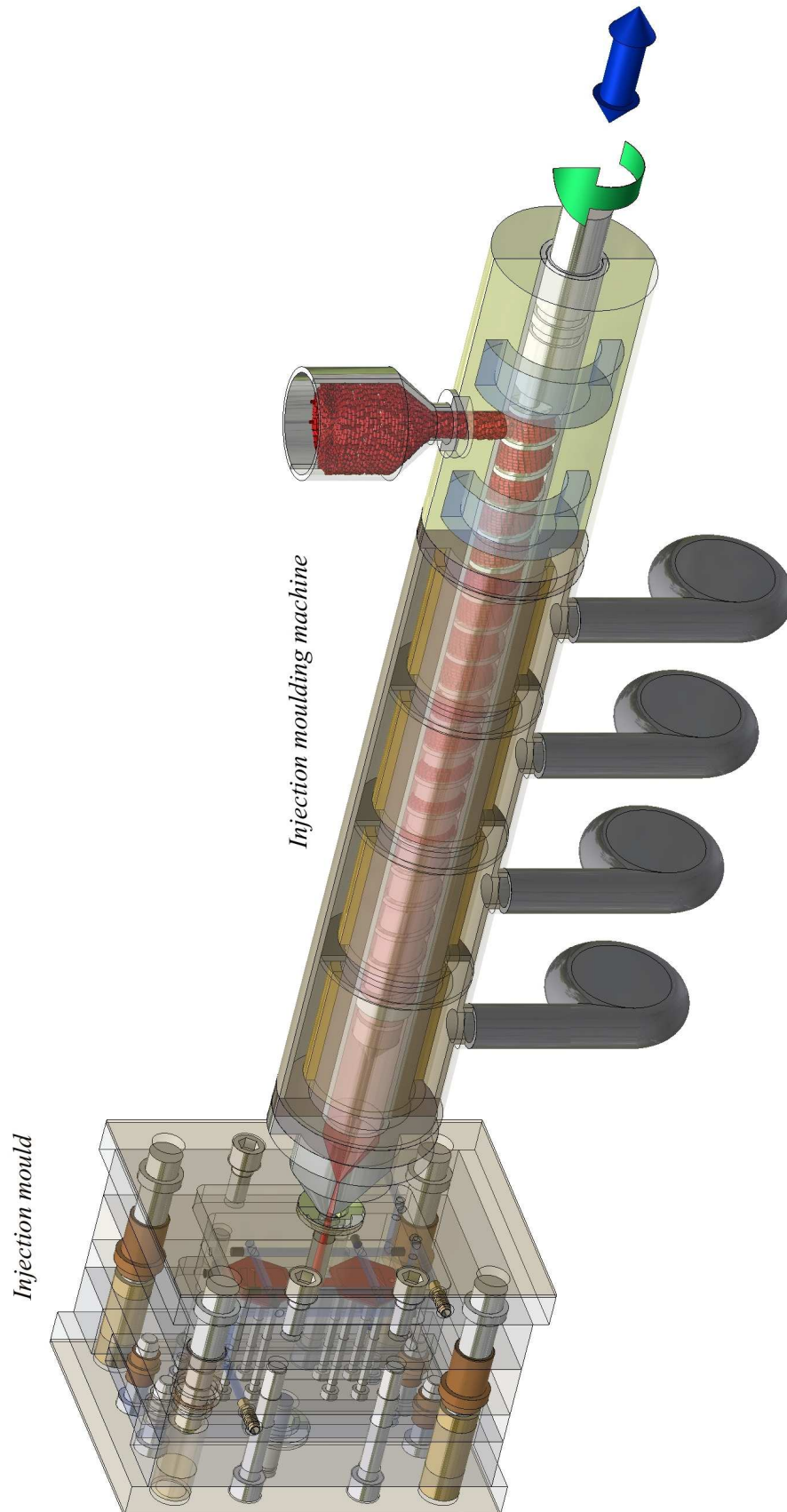
APPENDIX A III: PRODUCTION LINE OF FIBRE SPINNING



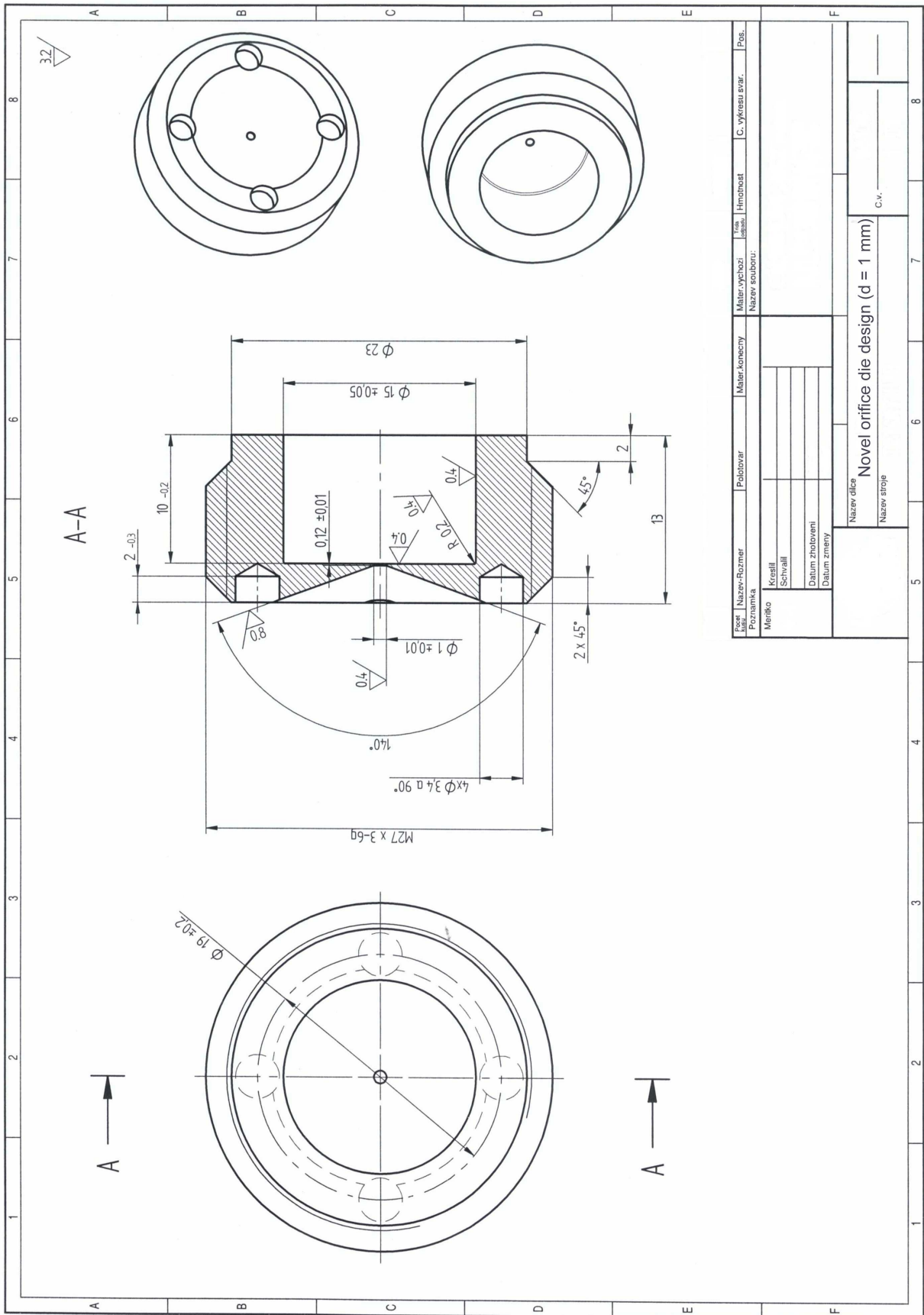
APPENDIX A IV: FILM BLOWING PRODUCTION LINE

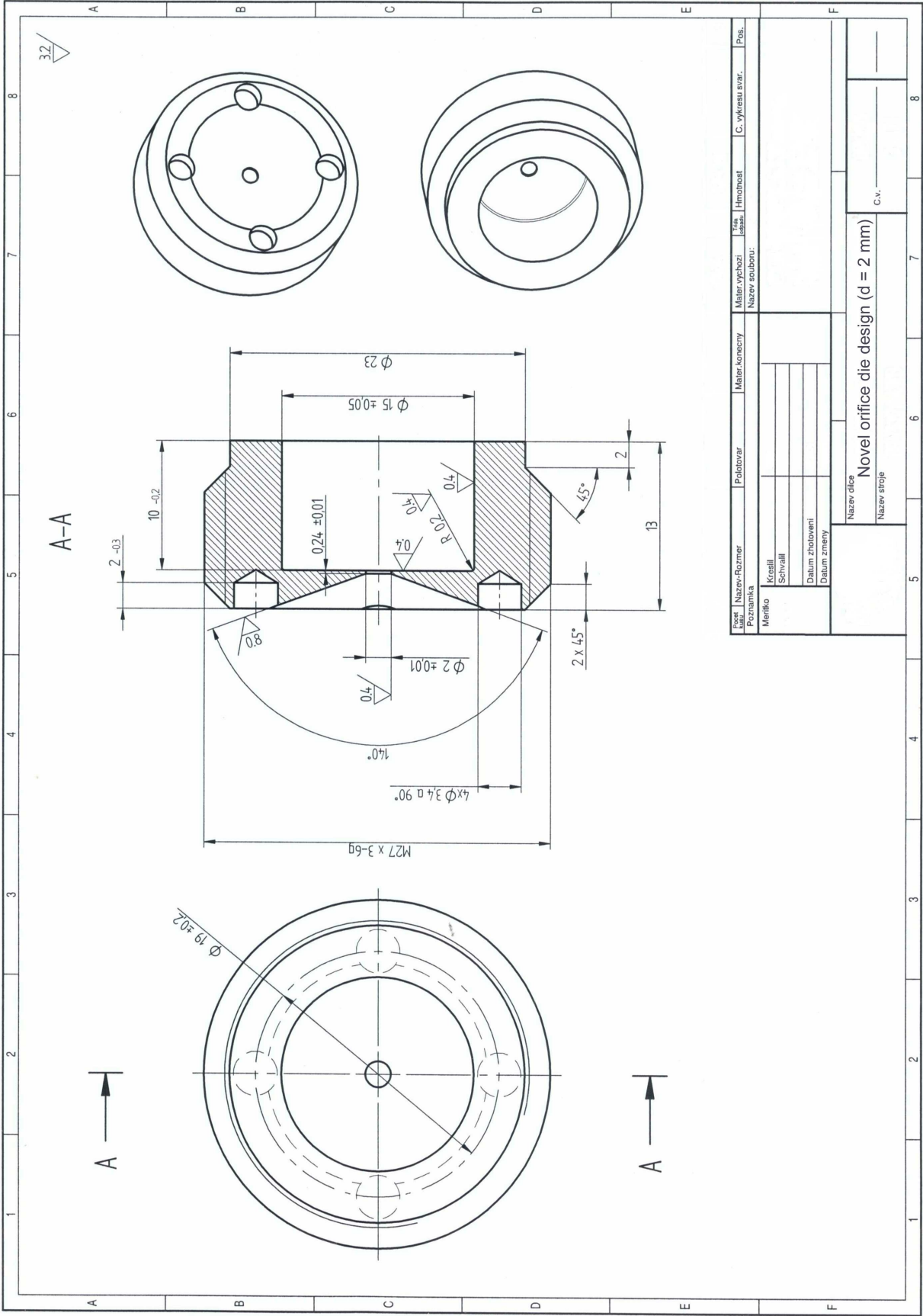


APPENDIX A V: INJECTION MOULDING PROCESS



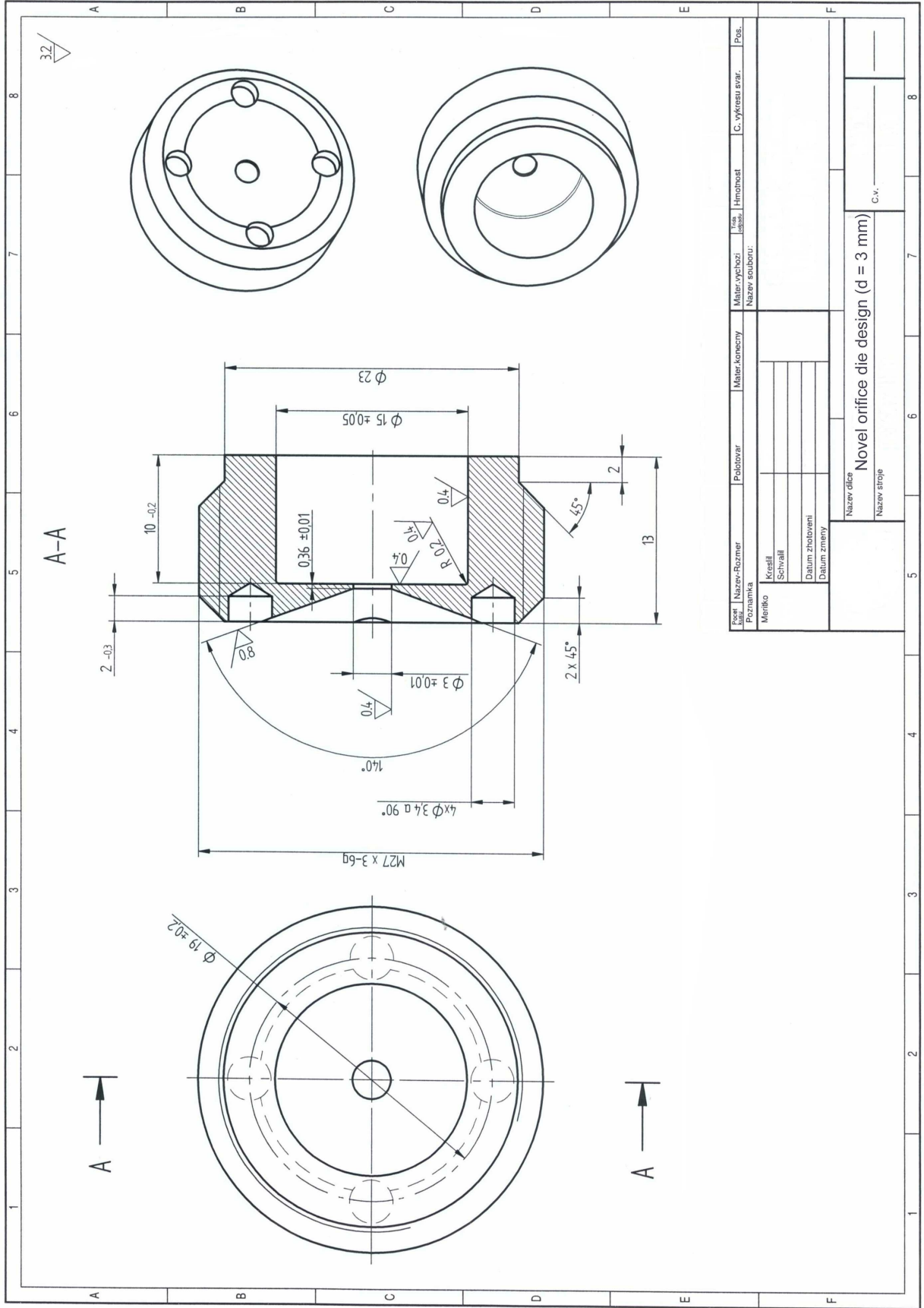
APPENDIX A VI: DRAWINGS OF NOVEL ORIFICE DIE DESIGN



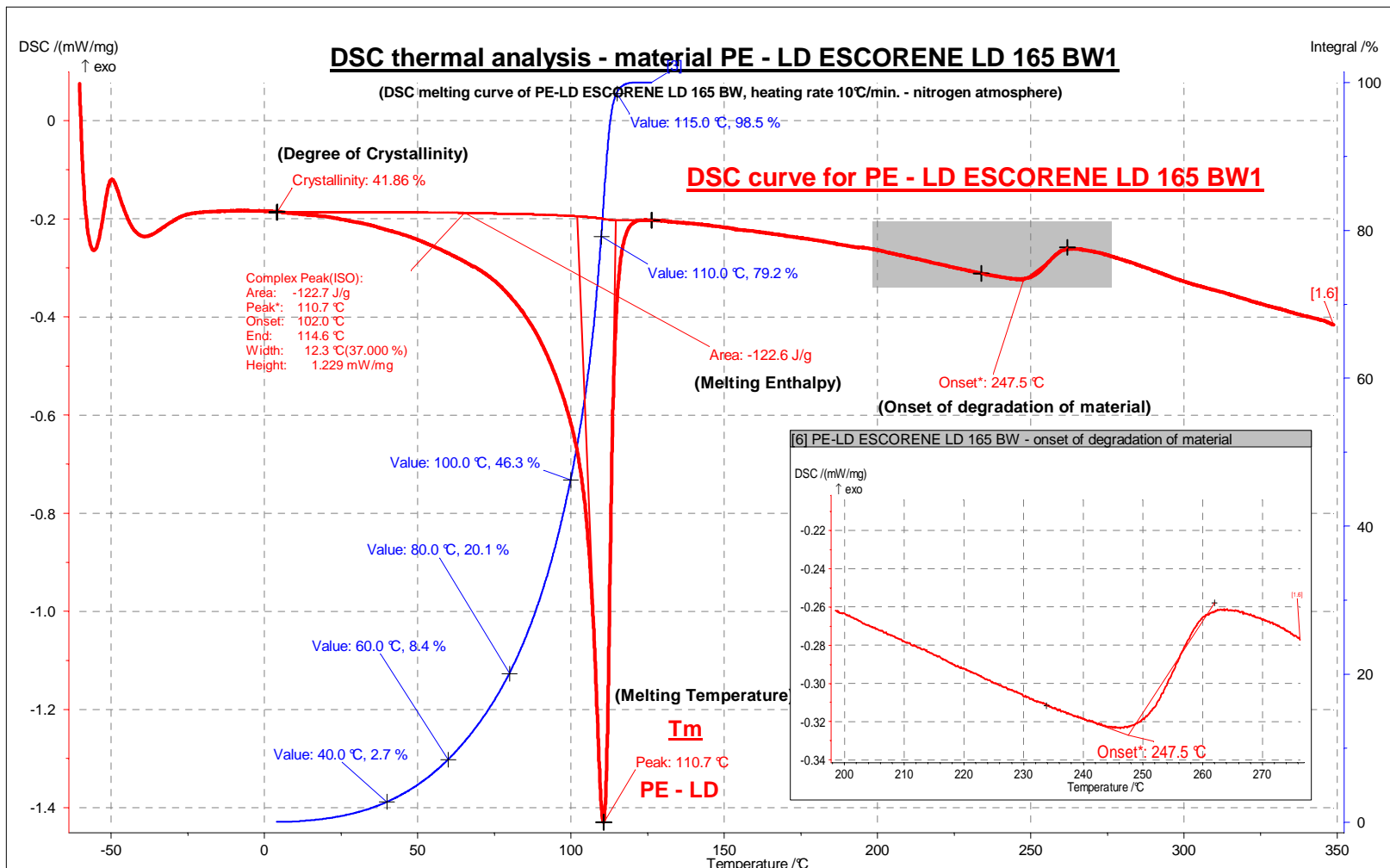


Popř. číslo	Název-Rozměr	Podstavec	Materiál	Materiál	Materiál	Tržba	Hmotnost	C. vykrešlu svar.	Pos.
1	Novel orifice die design (d = 2 mm)								
2									
3									
4									
5									
6									
7									
8									

Název díle
 Novel orifice die design (d = 2 mm)
 Název stroje
 C.v.

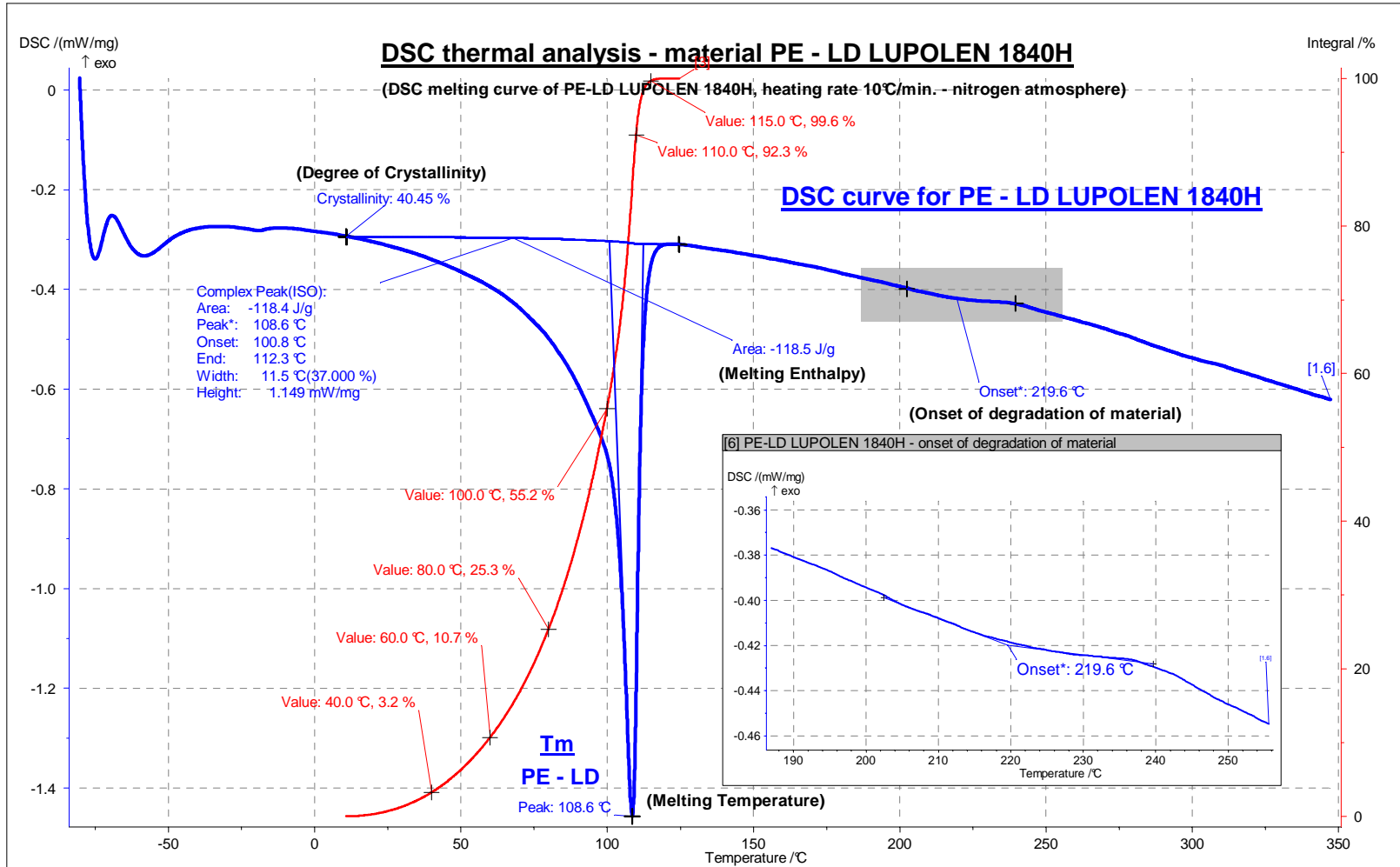


Číslo kresby	Název - Rozměr	Položkový	Materiál konečný	Materiál výtahový	Hmotnost	C. vykreslu svar.	Pros.
	Poznámka			Název souboru:			
Měřítko	Kreslí						
	Ševcáři						
	Datum zhotovení						
	Datum změny						
Název dílce		Novel orifice die design (d = 3 mm)					
Název stroje		C.v. _____					



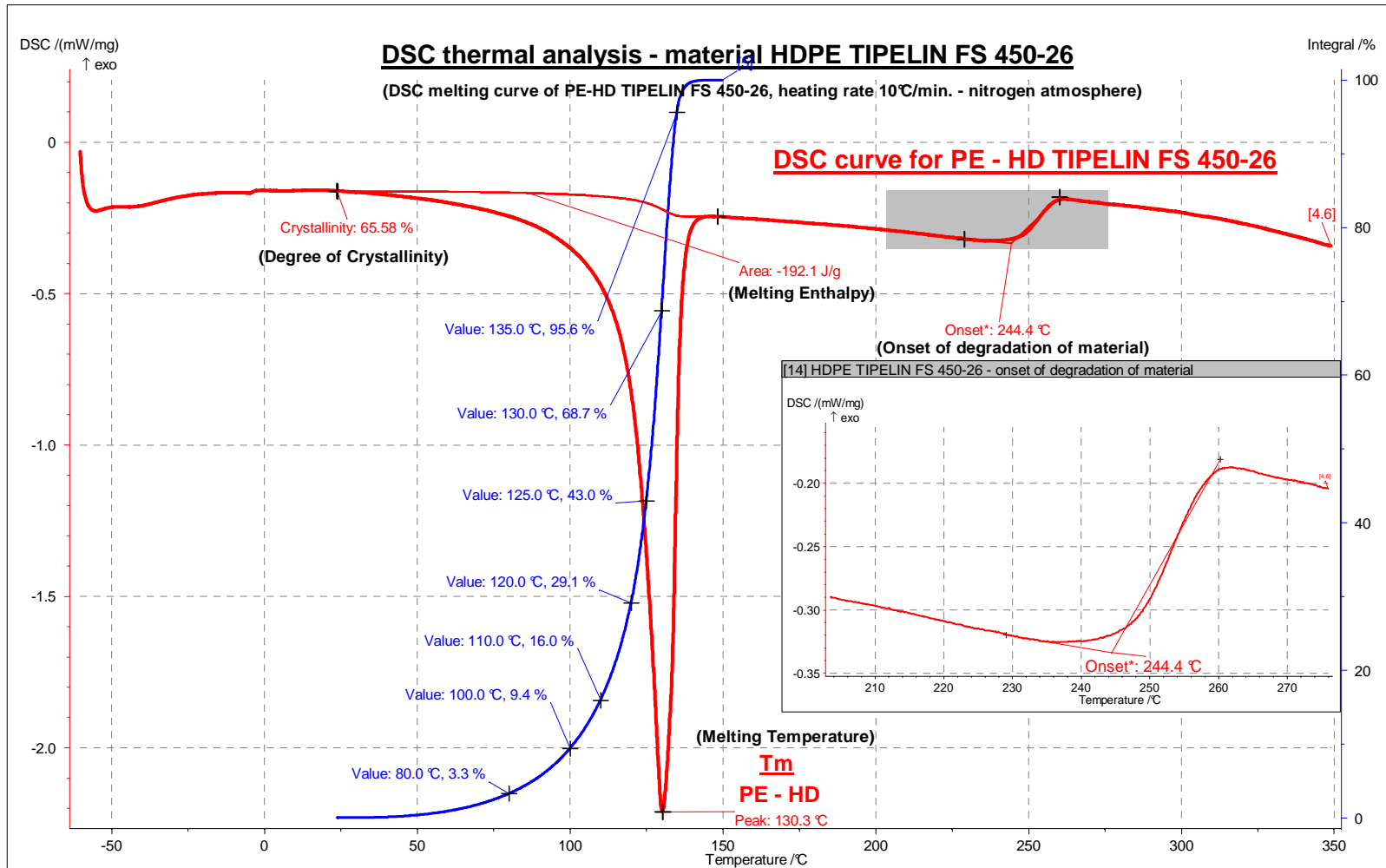
zapletal.b 06-05-2008 17:10

#	Instrument	File	Identity	Sample	Date	Mass	Segment	Range	Atmosphere	Correction
[1.6]	NETZSCH DSC 200 PC	PE-LD ESCORENE LD 16...	ESCORENE- LD 165 BW 1	ESCORENE- LD 165 BW 1	29.2.2008 14:23:56	5.300 mg	6/7	-60/10.00(K/min)/350	N2/50 / ---/---	000
[3]	NETZSCH DSC 200 PC	PE-LD ESCORENE LD 16...	ESCORENE- LD 165 BW 1	ESCORENE- LD 165 BW 1	29.2.2008 14:23:56	5.300 mg	1/1	-60/10.00(K/min)/350	N2/50 / ---/---	0

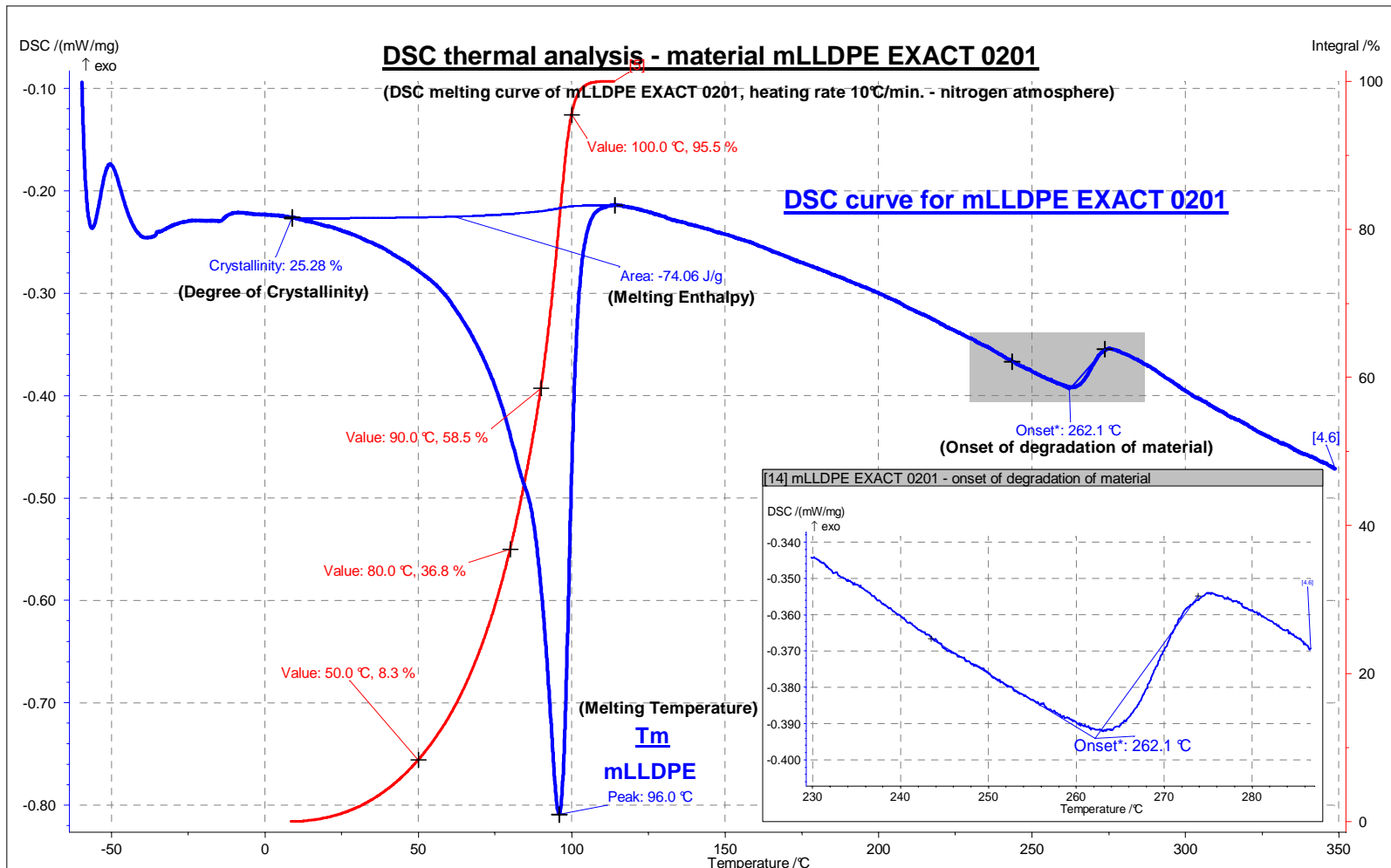


zapletal.b 06-05-2008 17:12

[#]	Instrument	File	Identity	Sample	Date	Mass	Segment	Range	Atmosphere	Correction
[1.6]	NETZSCH DSC 200 PC	PE-LD LUPOLEN 1840H ...	PE-LD LUPOLEN 1840H	PE-LD LUPOLEN 1840H	22.4.2008 10:03:13	5.200 mg	6/6	-80/10.00(K/min)/350	N2/50 / ---/---	400
[3]	NETZSCH DSC 200 PC	PE-LD LUPOLEN 1840H ...	PE-LD LUPOLEN 1840H	PE-LD LUPOLEN 1840H	22.4.2008 10:03:13	5.200 mg	1/1	-80/10.00(K/min)/350	N2/50 / ---/---	0



#	Instrument	File	Identity	Sample	Date	Mass	Segment	Range	Atmosphere	Correction
[4.6]	NETZSCH DSC 200 PC	HDPE TIPELIN FS 450-...	HDPE TIPELIN FS 450-26	HDPE TIPELIN FS 450-26	5.5.2008 7:54:48	5.200 mg	6/7	-60/10.00(K/min)/350	N2/50 / ---/---	000
[5]	NETZSCH DSC 200 PC	HDPE TIPELIN FS 450-...	HDPE TIPELIN FS 450-26	HDPE TIPELIN FS 450-26	5.5.2008 7:54:48	5.200 mg	1/1	-60/10.00(K/min)/350	N2/50 / ---/---	0



zapletal.b 06-05-2008 17:08

[#]	Instrument	File	Identity	Sample	Date	Mass	Segment	Range	Atmosphere	Correction
[4.6]	NETZSCH DSC 200 PC	mLLDPE EXACT 0201.sd...	mLLDPE EXACT 0201	mLLDPE EXACT 0201	5.5.2008 9:46:44	5.600 mg	6/7	-60/10.00(K/min)/350	N2/50 / ---/---	000
[5]	NETZSCH DSC 200 PC	mLLDPE EXACT 0201.md...	mLLDPE EXACT 0201	mLLDPE EXACT 0201	5.5.2008 9:46:44	5.600 mg	1/1	-60/10.00(K/min)/350	N2/50 / ---/---	0

APPENDIX AVIII: IR SPECTRUM OF TESTED MATERIALS

